HARVARD UNIVERSITY
Graduate School of Arts and Sciences

DISSERTATION ACCEPTANCE CERTIFICATE

The undersigned, appointed by the

Department of Physics

have examined a dissertation entitled

Superconducting Proximity Effect in Graphene

presented by Ko-Fan Huang

candidate for the degree of Doctor of Philosophy and hereby certify that it is worthy of acceptance.

Signature _____

Typed name: Professor Philip Kim, Chair

Signature _____

Typed name: Professor Bertrand Halperin

Signature _____

Typed name: Professor Amir Yacoby

Date: May 5, 2020

Superconducting Proximity Effect in Graphene

A DISSERTATION PRESENTED
BY
KO-FAN HUANG
TO
THE DEPARTMENT OF PHYSICS

IN PARTIAL FULFILLMENT OF THE REQUIREMENTS
FOR THE DEGREE OF
DOCTOR OF PHILOSOPHY
IN THE SUBJECT OF
PHYSICS

HARVARD UNIVERSITY
CAMBRIDGE, MASSACHUSETTS
MAY 2020

Thesis advisor: Professor Philip Kim Ko-Fan Huang

Superconducting Proximity Effect in Graphene

Abstract

Graphene is a popular candidate when it comes to the study of the superconductivity proximity effect. However, experiments have mainly been focusing on the transport behavior in two-terminal Josephson junctions. This dissertation presents unconventional transport experiments which study aspects of the proximity effect that were previously unexplored. The first experiment investigates systematically the graphene (G) - superconductor (S) hybrid system with a controllable interfacial barrier strength. We demonstrate how the Andreev process can be modulated by the magnetic field and the carrier density in graphene.

The second study focuses on the multi-terminal S-G-S junction with a loop which hosts Andreev bound states (ABS) in higher dimensions. Under specific voltage configurations, we are able to capture the elusive quartet– a state composed of four entangled electrons that is responsible for nonlocal supercurrents. With the Josephson junction biased, the system becomes periodically driven and is analyzed in the framework of Floquet theory. The associated dynamical energy spectrum can be modified with gate control and probed via a phase difference achieved by flux threaded through the device loop. Altogether, we have opened up new possibilities for the manipulation of Andreev bound states, creating a playground potentially for topological states.

Contents

1 Overview 2

2 Superconducting Proximity Effect 5
- 2.1 Bardeen-Cooper-Schreiffer (BCS) Theory . . . 7
- 2.2 Bogoliubov-de Gennes (BdG) Formalism . . . 10
- 2.3 Andreev Reflection at NS Interface . . . 14
  - 2.3.1 Andreev reflection . . . 14
  - 2.3.2 Blonder-Tinkham-Klapwijk (BTK) model . . . 15
  - 2.3.3 Tunneling conductance through NS junction . . . 24
- 2.4 Andreev Bound States in SNS Junctions . . . 27
  - 2.4.1 Scattering picture . . . 28
  - 2.4.2 Infinite-gap dot model . . . 31
  - 2.4.3 Supercurrent carried by ABS in short junctions . . . 34

3 Magnetoresistance Plateaus in Proximitized Graphene 38
- 3.1 Device Structure and Measurement Setup . . . 39
  - 3.1.1 Vertical graphene-insulator-superconductor architecture . . . 41
  - 3.1.2 Measurement Setup . . . 42
- 3.2 Transparent Regime: Al/Graphene . . . 43
- 3.3 Tunneling Regime: Al/BN/graphene . . . 46
- 3.4 Intermediate Regime: Al/MoS_2/Graphene . . . 49
  - 3.4.1 Differential conductance enhancement . . . 50
  - 3.4.2 Gate dependence . . . 52
- 3.5 Magnetoresistance Plateaus in the Intermediate Regime . . . 53
  - 3.5.1 Collection of devices . . . 57
  - 3.5.2 Step width and tunneling area . . . 59
  - 3.5.3 Gate dependence of the magnetoresistance plateaus . . . 60
  - 3.5.4 From plateaus to oscillations . . . 63
- 3.6 Conclusion . . . 66

4 Beyond Two-Terminal SNS Junctions 68
- 4.1 ABS in a Three-Terminal Josephson Junction: Quartets . . . 69
  - 4.1.1 A novel out-of-equilibrium coherent mode . . . 70
  - 4.1.2 Phases of quartets . . . 73

4.2 Quartets in Graphene . . . 75
4.2.1 Device fabrication and geometry . . . 76
4.2.2 Two-terminal characterization measurement . . . 78
4.2.3 Quartet measurement . . . 82
4.3 Quartets in the Presence of Magnetic Field . . . 86
4.3.1 Two-terminal junction with a loop . . . 87
4.3.2 Quartet in three-terminal junction with a loop . . . 89
4.4 Adiabatic Approximation: Effective Andreev Bound State . . . 92
4.4.1 Engineering the effective ABS via contact couplings . . . 94
4.4.2 Engineering the effective ABS via gate . . . 96
4.5 Different Types of Quartet Process . . . 100
4.5.1 Conventional quartet process . . . 101
4.5.2 Split quartet process . . . 103
4.5.3 Interference and flux dependence of I_{qc} . . . 104

5 Emergence of the Floquet Spectrum 106
5.1 Landau-Zener transition . . . 108
5.2 Driven Two-level Systems . . . 110
5.3 Floquet Theorem: Bloch's Theorem in Time . . . 112
5.4 Formation of Floquet Ladders . . . 114
5.4.1 Classical ladders . . . 115
5.4.2 Landau-Zener tunneling at resonances . . . 117
5.4.3 Construction of three-dimensional Floquet spectrum . . . 118
5.5 Probing the Floquet Spectrum . . . 120
5.5.1 Evolution of Floquet levels along V . . . 120
5.5.2 Flux dependence of the Floquet spectrum . . . 123
5.6 Outlook: A Platform for Exploring Topology . . . 127
5.6.1 Superconductivity and band theory . . . 128
5.6.2 Weyl nodes in three-dimensional ABS spectrum . . . 129
5.6.3 Floquet topological insulators . . . 132

Appendix A Device Fabrication 134
A.1 Stamp Preparation . . . 135
A.2 Inverted Stacking . . . 135

Appendix B Measurements 138
B.1 Current Bias Measurement in a Three-terminal Junction . . . 139
B.2 Voltage Bias Measurement in a Three-terminal Junction . . . 142
B.2.1 Voltage bias measurement for an ideal junction . . . 142
B.2.2 $V - I$ curve of the junction in quartet circuit . . . 144
B.2.3 Comparison between current bias and voltage bias . . . 145

B.2.4 Voltage bias measurement for quartet detection 147
B.3 Quartet supercurrent 153

Appendix C Floquet Formalism 154
C.1 Floquet Theorem 155
C.2 Floquet Theory of the Dot Toy-Model 156

Appendix D Quartet in Loop-biased Measurement 160

References 176

Listing of figures

2.1 Superconducting proximity effect . . . 6
2.2 Quasiparticle DOS . . . 14
2.3 NS system . . . 16
2.4 E(k) for NS interface . . . 17
2.5 Scattering process at NS interface . . . 19
2.6 Andreev reflection . . . 22
2.7 Phase and probability of Andreev reflection . . . 23
2.8 BTK model . . . 26
2.9 Formation of Andreev bound states . . . 27
2.10 Andreev bound state energies . . . 30
2.11 Andreev bound state energies in a dot model . . . 33
2.12 ABS: left and right moving supercurrents . . . 35

3.1 Device structure . . . 40
3.2 Measurement configuration of vertical graphene/superconductor structure . . . 42
3.3 Transparent regime gate dependence . . . 43
3.4 Transparent regime magnetic field dependence . . . 45
3.5 Tunneling regime differential conductance . . . 48
3.6 Optical image of monolayer MoS_2 . . . 50
3.7 Intermediate regime differential conductance . . . 51
3.8 Intermediate regime gate dependence . . . 52
3.9 (Device A) Intermediate regime magnetic field dependence . . . 54
3.10 (Device C) Intermediate regime magnetic field dependence . . . 55
3.11 Temperature dependence of the magnetic plateaus . . . 56
3.12 Different sweep direction of magnetic field . . . 57
3.13 Step feature among different devices . . . 59
3.14 (Device C) Gate dependence of the magnetoresistance plateaus . . . 61
3.15 (Device C) Gate dependence of the height of magnetoresistance plateaus . . . 62
3.16 (Device B) Gate dependence of the magnetoresistance plateaus . . . 64
3.17 (Device B, D) Magnetoresistance plateaus and oscillations . . . 65

4.1 Transfer of Cooper pairs in a two-terminal junction . . . 69
4.2 Quartet process in a three-terminal junction . . . 70
4.3 Quartet process in the Andreev bound state picture . . . 71
4.4 Phases in a quartet process . . . 74

4.5 Two-dimensional Andreev bound state spectrum . . . 76
4.6 Device: three-terminal graphene Josephson junction with a loop . . . 77
4.7 Two-terminal measurement setup . . . 78
4.8 Gate dependence of supercurrent in two-terminal measurement . . . 79
4.9 SQUID-like pattern in two-terminal measurement . . . 81
4.10 Quartet measurement setup . . . 82
4.11 Different supercurrents in a three-terminal Josephson junction . . . 83
4.12 $V_1 - V_2$ scan of G_1 in quartet measurement . . . 84
4.13 $V_1 - V_2$ scan of G_2 in quartet measurement . . . 85
4.14 Illustration of a two-terminal junction with a loop . . . 87
4.15 Illustration of a three-terminal junction with a loop . . . 90
4.16 Equivalence of three-terminal junction with and without a loop . . . 92
4.17 Effective Andreev bound states . . . 93
4.18 Calculation: coupling dependence of quartet critical current as a function of flux . . . 95
4.19 Calculation: Andreev bound state spectrum at different values of flux . . . 96
4.20 Calculation: gate dependence of quartet critical current as a function of flux . . . 98
4.21 Measured gate dependence of quartet supercurrent as a function of magnetic flux . . . 99
4.22 Conventional quartet process . . . 100
4.23 Conventional quartet process among four contacts . . . 102
4.24 Split quartet process among four contacts . . . 104

5.1 Time-dependent Andreev bound states in the adiabatic regime . . . 107
5.2 $V = 0^+$ region in $V_1 - V_2$ scan . . . 108
5.3 Time-dependent Andreev bound states . . . 109
5.4 Floquet ladders . . . 116
5.5 Calculation: classical Floquet ladders as a function of V . . . 119
5.6 Measured quartet conductance as a function of V . . . 120
5.7 Evolution of Floquet levels along V . . . 122
5.8 Measured quartet signal as a function of V at different values of flux . . . 124
5.9 Quartet conductance as a function of V and magnetic field . . . 125
5.10 Quartet conductance as a function of flux at different values of V . . . 126
5.11 Comparison between band structure and Andreev bound state spectrum . . . 129
5.12 Calculation: Weyl nodes in three-dimensional Andreev bound state spectrum. . . . 131
5.13 Floquet topological insulator. . . . 133

A.1 PPC stamp . . . 136
A.2 Inverted stacking . . . 137

B.1 Circuit of current bias measurement for three-terminal Josephson junction . . . 139
B.2 $I_{bias,1} - I_{bias,2}$ scan of three-terminal Josephson junction . . . 141
B.3 Voltage bias measurement for an ideal Josephson junction . . . 143

B.4 $V - I$ curve for the quartet junction 144
B.5 Comparison between current and voltage bias measurements 146
B.6 Circuit of quartet measurement 148
B.7 Josephson signal as a function of V_1 150
B.8 Josephson signal as a function $V_{bias,1}$ 152
B.9 Quartet signal as a function $V_{bias,1}$ 153

C.1 Floquet levels calculated from the dot toy-model 159

D.1 Circuit of quartet measurement (loop biased) 161
D.2 $V_2 - V_0$ scan with the loop-biased configuration 162
D.3 $V_0 - B$ scan with the loop-biased configuration 164
D.4 $V_0 - B$ zoom-in scan with the loop-biased configuration 165
D.5 Period doubling of quartet conductance with the loop-biased configuration 166

Dedicated to my parents, Yvonne Teng and Kai Huang.

Acknowledgments

I NEVER IMAGINED WHAT IT WOULD BE LIKE. To be honest, I didn't even expect this day to come: post-defending, sitting down to write the acknowledgements, which is the last piece for completing this dissertation. But as they say, we should always expect the unexpected and life is full of wonderful surprises. Looking back the past few years at Harvard, for sure I would not have made it this far without the help, or even just the presence of these people. I am truly grateful and feel extremely lucky and privileged to have met them.

My deepest gratitude goes to Philip, who is the best advisor I could ever wish for. He doesn't just provide guidance in research, but also valuable advice in life. He genuinely cares about our well-being and always treat people with respect and consideration. I remember when I first met Philip in his office, I was pretty clueless, not sure what to do in graduate school. He still took me in and gave me the opportunity to learn and grow. He once said that it doesn't matter what we do in the future, he just hopes we are happy and successful. During times of my hesitation and self-doubt, he gave me the ultimate support and encouragement. A lot of things would not be possible if it weren't for Philip. I still have a long way to go, but I'm already far from where I used to be and I will always appreciate Philip for guiding me towards the right direction.

Gilho was my first mentor in the group. He taught me everything from scratch– from scratching

graphene to using clean-room tools and performing measurements in cryostats. There were numerous times I would ask myself, "what would Gilho do,? when things didn't go exactly the way I expected. More importantly, he showed me how we should embrace the challenges and difficulties while staying focused and optimistic. Besides being an excellent mentor in research, he is also a great friend who brings everyone together. I truly cherish all the bike trips, picnics, camping, Korean bbq parties and many other countless joyous memories.

In the later part of PhD, I had the pleasure to work with Yuval. He is very knowledgeable, always eager to lend a helping hand and selflessly share his experience. He is a great friend who looked out for me, motivated me and made me improve in many facets in life. If it weren't for Yuval, I wouldn't have even started the quartet experiment and who knows where I'd be be for my PhD. I also want to thank Denis and Régis, who are the theorists we work together with. Even though they are all the way in France and we have barely spent any time in person, they feel like friends and teachers whom I've known for a long time. They are always super patient, answering my endless questions and helping me acquire a better understanding of the physics.

Thanks goes to all the Kim group members, from old members in the beginning of time: Ke, Hiroshi, Luis, Kwabena, Youngjae, Nicola, Jesse, Jonah, Kate, Mehdi, to the new generation: Önder, Andrew, Artem, Laurel, Zeyu, Tom, Zhongying, Andres, Joon Young, Tamar, Antti, Qi. They have created the most friendly and fun environment for work. It became such a great place to just hang out. I really enjoyed all the conversations I had with Rebecca as we sat in the corner of the office. Over time, I developed a great sense of belonging to the group and I cannot describe how much it means to me. What I can easily say though is that I will never forget all the group outings, the summer bbq

and Christmas parties at Philip's place, and just having that cup of tea and chilling with everyone in the lab kitchen. All these moments will stay vivid with me.

Frank, Xiaomeng and Jing were the senior graduate students in lab and the group of friends who were and still are always there for me. It has been amazing not only experiencing the PhD life with them but also going through plenty of other life-defining occasions. Regardless of the different places we will be in the future, the group chat will surely keep our phones buzzing. Andy and I joined Philip's group around the same time. As young graduate students, we both felt lost at some point but thankfully he made the perfect companion. I remember as fabrication newbies, we used to spend the whole night in the cleanroom, trying to figure things out. It was such great fun listening to him sing in a helium voice when we transferred helium together. Although he was one year below me, we always said we should graduate together. We did not make that happen in the end, but at least it was for good reason. I am super happy for him now that he has found even greater ambition in his research and I know he is going to show the world something special.

I like to call Si Young and Hyobin hyungs. We got coffee together and I could go on rambling about everything in life to them. I've probably never seen anyone calmer than Si Young. No matter what happened, he would never lose his composure. As experimentalists, we all have to face a lot of unforeseen failures which can be very frustrating. However, every time after I talked to Si Young, it would be like having a meditation session and all my worries would be gone. Hyobin is like an elder brother to me. In lab he was always helpful when I had questions or needed something. He was also the person I can talk to, watch movies with and exercise with. He has a very subtle sense of humor and I'll always remember his laughter and the "life stories" he shared with me.

My parents and my brother, Kevin, have always been the biggest support throughout my life. One of the reasons doing graduate school was tough was that I had to be so far away from home. Talking to them over the phone was something I looked forward to the most every week. Their love is the greatest blessing I have and all that I have, I owe to my family.

Lastly, another reason I need to thank Philip is that he brought Austin to my life. He has become my best friend and partner in life. He is always supportive and gives me the courage to move forward. He showed me the value of hard work and that I should be proud of what I do. He always makes me laugh with his sense of humor and strengthen my mind with his determination. Every day I spend with Austin I get precious moments that I smile at when I think of them. There is going to be a lot of challenges in the future but knowing that he will be by my side makes me stronger and I cannot wait to start a new chapter in life with him.

A final big thank you to all the people I have met, including all of my friends outside of lab. You have made my life in Cambridge so colorful and my journey at Harvard life-changing with so many invaluable memories. I look forward to seeing you all again!

Author List and Previous Publications

The following authors contributed to Chapter 3:

Önder Gül, Kenji Watanabe, Takashi Taniguchi, Philip Kim.

The following authors contributed to Chapter 4 and 5:

Yuval Ronen, Régis Mélin, Denis Feinberg, Kenji Watanabe, Takashi Taniguchi, Philip Kim.

Results of the following publications are not included in this dissertation:

"Inducing superconducting correlation in quantum Hall edge states". Gil-Ho Lee, Ko-Fan Huang, Dmitri K. Efetov, Di S. Wei, Sean Hart, Takashi Taniguchi, Kenji Watanabe, Amir Yacoby, Philip Kim. Nature Physics, 13, 693-698 (2017).

"Logarithmic singularities and quantum oscillations in magnetically doped topological insulators". Debaleena Nandi, Inti Sodemann, Kevin Shain, Gil-Ho Lee, Ko-Fan Huang, Cui-Zu Chang, Yunbo Ou, S.-P. Lee, J. Ward, J. S. Moodera, Philip Kim, Amir Yacoby. Physical Review B 97, 085151 (2018).

"Signatures of long-range-correlated disorder in the magnetotransport of ultrathin topological insulators". Debaleena Nandi, Brian Skinner, Gil-Ho Lee, Ko-Fan Huang, Kevin Shain, Cui-Zu Chang, Yunbo Ou, S.-P. Lee, J. Ward, J. S. Moodera, Philip Kim, Bertrand I. Halperin, Amir Yacoby. Physical Review B 98, 214203 (2018).

1

Overview

The superconducting proximity effect was first observed in 1932 by R. Holm and W. Meissner[1] and has remained a subject of both theoretical and experimental interest. Over the past few decades, due to the advancement of nano-fabrication techniques, the hybrid system of superconductors and semiconductors has garnered much attention and has made big strides towards the under-

standing of the superconducting proximity effect. More recently, graphene has been the most widely used platform for this type of study. The popularity can be attributed to the fact that graphene is easily accessible and exhibits a wide range of physical phenomena that can interact with superconductivity. For instance, massless Dirac fermions, a highly correlated hydrodynamical liquid and composite quasi-particles with fractional charge are some of the many novel physical phenomena that graphene offers. A hybrid graphene (G)-superconductor (S) system then provides an opportunity to study the interplay of superconductivity with these exotic entities and hence enables us to tap further into the highly fascinating and complex world of superconductivity.

But perhaps most importantly is that superconducting contacts can be established on graphene with high yield. Unlike the 2DEG predecessor, GaAs, and unlike other van der Waals material, graphene is simply superior when it comes to the easiness and reliability of having working superconducting contacts. In addition, the gate tunable carrier density and carrier types are free experimental knobs that a hybrid G-S device comes with and this level of control over an experiment is simply unprecedented. Despite the intense research, much about superconductivity in hybrid G-S systems remains uncharted. In this thesis, I will show how we use state-of-art nano-fabrication techniques along with an unconventional measurement circuitry to uncover unseen aspects of superconductivity in graphene-based devices.

In Chapter 2, I will introduce the concept of superconducting proximity effect. Basic theoretical models are described, in order to discuss the microscopic mechanism of a single normal (N) - superconductor (S) interface as well as an S-N-S sandwich structure. It provides the background knowledge for the experiments studied in the following chapters.

In Chapter 3, we present the experimental results in the simplest type of proximity effect devices: an NS hybrid system, in which N and S are graphene and superconducting Al, respectively. As it turns out, one can get drastically different superconducting behaviors just from the transparency of the NS contact. Based on this, we insert different barrier layers between graphene and Al. By using a van der Waals material as the barrier layer, the interfaces and contact transparency can be well controlled. We systematically investigate the properties of Andreev reflection in different regimes of the transparency and show how the proximity effect in graphene can be modulated.

In Chapter 4, we move on from N-S interfaces to three-terminal S-N-S junctions. The successive Andreev reflections at NS boundaries result in the formation of Andreev bound states that carry supercurrent in the proximitized region. In a three-terminal junction, besides local supercurrents that come from transmitting one Cooper pair, there may also be a phenomenon of two Cooper pairs forming four correlated electrons that result in nonlocal supercurrents flowing synchronously among all three superconducting leads. We explore the details of these unique entangled states, known as the quartets, and their energy spectra that characterize the proximitized graphene.

Chapter 5 continues the quartet story. While in the previous chapter we only vary the system adiabatically, in Chapter 5 we go beyond the adiabatic regime. As the dynamics is taken into consideration, the energy spectra of quartet takes an unexpected turn and evolves into Floquet ladders as in a periodically driven system. We compare the NS hybrid systems with topological materials and discuss the outlook for future experiments.

Finally, the appendices include details of device fabrication, measurement setup, and in-depth mathematical description of the theory behind quartets.

2

Superconducting Proximity Effect

Superconductivity was discovered in 1911 by H. Kamerlingh Onnes in Leiden as he was measuring the resistivity of mercury. He found that it drops to zero below some critical temperature T_c, which is the fundamental phenomenon of superconductivity. Since for a metal at low temperatures T , the resistivity has a T^2 contribution from electron-electron scattering and a T^5 contribution from

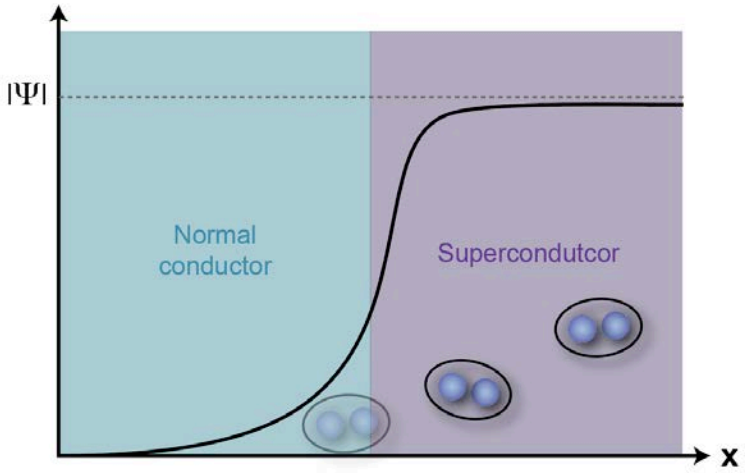

Figure 2.1: When a normal conductor is put in proximity contact to a superconductor, the order parameter $|\Psi|$ can leak into the normal region.

phonon scattering, the vanishing resistivity at nonzero T indicates that there is a new ground state below T_c. Another fundamental property of superconductivity was found by W. Meissner in 1933. The so-called Meissner effect is the repulsion of a magnetic field below T_c, meaning a superconductor is a perfect diamagnet. In 1950, the theory of superconductivity was introduced by V. L. Ginzburg and L. Landau with the description of superconducting phase transition from the thermodynamic point of view. They proposed there is an order parameter $|\Psi|$ characterizing the superconducting state, which is only nonzero below T_c.

When a normal conductor is brought in close proximity to a superconductor, its properties can be dramatically changed. The early knowledge about this proximity effect was understood as the leakage of superconducting order parameter $|\Psi|$ from the superconductor into the normal region as shown in figure 2.1. Later, a microscopic understanding of the physical mechanism is developed and can be elegantly described by the Andreev reflection. In this chapter, we will start with a brief introduction

to the BCS theory and then follow the history that leads to our current understanding of the superconducting proximity effect.

2.1 Bardeen-Cooper-Schreiffer (BCS) Theory

The first truly microscopic theory of superconductivity was published by J. Bardeen, L. N. Cooper, and R. Schrieffer in 1957.[2] The key idea of the starting point in BCS theory is that there is an effective attraction for electrons near the Fermi surface due to the exchange of phonons. Cooper found that a single pair of electrons outside the occupied Fermi sea would form a bound state, the so-called Cooper pairs. But the whole Fermi surface would be unstable due to the creation of such a pair; unless every electron at the the Fermi surface becomes bounded into a Cooper pair. How can one express a many-particle wave function in which all electrons are paired with one another? For this new ground state, Schrieffer wrote down a coherent state with operators that create and annihilate Cooper pairs centered at $\boldsymbol{R}$: $\varphi^\dagger(\boldsymbol{R})$ and $\varphi(\boldsymbol{R})$. Since it is more convenient to work in $\boldsymbol{k}$-space, we need a uniform translationally invariant solution. The pair creation operator can be defined by

$$\hat{p}^\dagger_{\boldsymbol{k}} = c^\dagger_{\boldsymbol{k},\uparrow} c^\dagger_{-\boldsymbol{k}}, \tag{2.1}$$

which creates a pair of electrons with opposite spins and zero total crystal momentum. Then the coherent state many-body wave function that Schrieffer proposed can be written as

$$|\psi_{BCS}\rangle = \prod_{\boldsymbol{k}} (u_{\boldsymbol{k}} + v_{\boldsymbol{k}} c^\dagger_{\boldsymbol{k},\uparrow} c^\dagger_{-\boldsymbol{k},\downarrow}) \, |0\rangle \,, \tag{2.2}$$

where $|0\rangle$ is the vacuum state without any electrons and $u_{\boldsymbol{k}}, v_{\boldsymbol{k}}$ are the still-unknown complex coefficients. Normalization requires

$$\langle \psi_{BCS} | \psi_{BCS} \rangle = \prod_{\boldsymbol{k}} (|u_{\boldsymbol{k}}|^2 + |u_{\boldsymbol{k}}|^2) = 1, \tag{2.3}$$

which is certainly satisfied if we demand $|u_{\boldsymbol{k}}|^2 + |u_{\boldsymbol{k}}|^2 = 1$ for all $\boldsymbol{k}$.

The Hamiltonian can be written as

$$H = \sum_{\boldsymbol{k}\sigma} \xi_{\boldsymbol{k}} c^\dagger_{\boldsymbol{k}\sigma} c_{\boldsymbol{k}\sigma} + \frac{1}{N} \sum_{\boldsymbol{k}\boldsymbol{k}'} V_{\boldsymbol{k}\boldsymbol{k}'} c^\dagger_{\boldsymbol{k},\uparrow} c^\dagger_{-\boldsymbol{k},\downarrow} c_{-\boldsymbol{k}',\downarrow} c_{\boldsymbol{k}',\uparrow}, \tag{2.4}$$

where the first term is just the usual kinetic energy of the electrons, and the second term is due to the electron-electron interaction with $V_{\boldsymbol{k}\boldsymbol{k}'} < 0$ near the Fermi surface.

By using the mean-field approximation the quartic term can be decoupled:

$$\begin{aligned} &\langle c^\dagger_{\boldsymbol{k},\uparrow} c^\dagger_{-\boldsymbol{k},\downarrow} c_{-\boldsymbol{k}',\downarrow} c_{\boldsymbol{k}',\uparrow} \rangle \\ &\qquad \approx \langle c^\dagger_{\boldsymbol{k},\uparrow} c^\dagger_{-\boldsymbol{k},\downarrow} \rangle c_{-\boldsymbol{k}',\downarrow} c_{\boldsymbol{k}',\uparrow} + c^\dagger_{\boldsymbol{k},\uparrow} c^\dagger_{-\boldsymbol{k},\downarrow} \langle c_{-\boldsymbol{k}',\downarrow} c_{\boldsymbol{k}',\uparrow} \rangle - \langle c^\dagger_{\boldsymbol{k},\uparrow} c^\dagger_{-\boldsymbol{k},\downarrow} \rangle \langle c_{-\boldsymbol{k}',\downarrow} c_{\boldsymbol{k}',\uparrow} \rangle. \end{aligned} \tag{2.5}$$

We can define a parameter

$$\Delta_{\boldsymbol{k}} \coloneqq -\frac{1}{N}\sum_{\boldsymbol{k}\boldsymbol{k}'} V_{\boldsymbol{k}\boldsymbol{k}'}\langle c_{-\boldsymbol{k}',\downarrow} c_{\boldsymbol{k}',\uparrow}\rangle \tag{2.6}$$

and

$$\Delta^*_{\boldsymbol{k}} = -\frac{1}{N}\sum_{\boldsymbol{k}\boldsymbol{k}'} V_{\boldsymbol{k}\boldsymbol{k}'}\langle c^\dagger_{\boldsymbol{k}',\uparrow} c^\dagger_{-\boldsymbol{k}',\downarrow}\rangle. \tag{2.7}$$

Then the mean-field BCS Hamiltonian is written as

$$H_{BCS} = \sum_{\boldsymbol{k}\sigma} \xi_{\boldsymbol{k}} c^\dagger_{\boldsymbol{k}\sigma} c_{\boldsymbol{k}\sigma} - \sum_{\boldsymbol{k}} \Delta^*_{\boldsymbol{k}} c_{-\boldsymbol{k},\downarrow} c_{\boldsymbol{k},\uparrow} - \sum_{\boldsymbol{k}} \Delta_{\boldsymbol{k}} c^\dagger_{\boldsymbol{k},\uparrow} c^\dagger_{-\boldsymbol{k},\downarrow} + \text{const.}, \tag{2.8}$$

and we have

$$H_{BCS}\,|\psi_{BCS}\rangle = E_{BCS}\,|\psi_{BCS}\rangle\,, \tag{2.9}$$

where the ground state $|\psi_{BCS}\rangle$ is the condensate state and E_{BCS} is the temperature-dependent energy of the condensate. Note that since H_{BCS} contains terms in the form $c\ c$ and $c^\dagger c^\dagger$, the number of electrons is not conserved, meaning the eigenstates of H_{BCS} do not have a fixed electron number.

Eq.2.6 is known as the BCS gap parameter. In 1959, L. P. Gor'kov demonstrated the derivation of the Ginzburg-Landau theory from the BCS theory, and showed that the order parameter $|\Psi|$ is essentially the same as the BCS gap Δ, except for some constant factors. In fact, $|\Psi|^2$ can even be

identified as the density of Cooper pairs in the superconductor.

2.2 Bogoliubov-de Gennes (BdG) Formalism

The excitations of the superconductor are broken Cooper pairs states instead of single particle states like in a normal metal. Since the BCS theory is written in the single particle creation and annihilation operators specified by the wave vector $\boldsymbol{k}$ and spin σ, it can become very cumbersome. Based on the BCS theory, in 1958 N. Bogoliubov developed a mathematical formulation,[3] in which the concept of coherent mixtures of particles and holes was introduced and these mixed particle-hole excited states are known as the Bogoliubons. The operators for the Bogoliubons have been generalized by P. G. de Gennes in order to study layered structures with pair potential that varies in space.[4,5] In this description, the momentum operators in $\boldsymbol{k}$-space have been replaced by field operators in real space:

$$H_{BdG}(\boldsymbol{r}) = \begin{pmatrix} H_0(\boldsymbol{r}) & \Delta(\boldsymbol{r}) \\ \Delta^*(\boldsymbol{r}) & -H_0(\boldsymbol{r}) \end{pmatrix}, \tag{2.10}$$

where H_0 is the free-electron Hamiltonian:

$$H_0(\boldsymbol{r}) = \frac{p^2}{2m} - E_F + U(\boldsymbol{r}). \tag{2.11}$$

The corresponding Schrödinger equation is

$$H_{BdG}(\boldsymbol{r})\Psi(\boldsymbol{r}) = E\Psi(\boldsymbol{r}), \quad \text{with } \Psi(\boldsymbol{r}) = \begin{pmatrix} \psi_e(\boldsymbol{r}) \\ \\ \psi_h(\boldsymbol{r}) \end{pmatrix}, \tag{2.12}$$

which is called the Bogoliubov-de Gennes equation. $\psi_e(\boldsymbol{r})$ and $\psi_h(\boldsymbol{r})$ are the electron-like and hole-like wavefunctions that are coupled via the pair potential $\Delta(\boldsymbol{r})$. If $\Delta(\boldsymbol{r})$ vanishes, Eq.2.12 recovers the usual single-particle Hamiltonian for uncorrelated electron and hole, as in the case of a normal conductor.

Quasiparticle density of states

For a homogeneous superconductor, it is convenient to expand the eigenfunctions of the BdG equation (Eq.2.12) in terms of quasiparticle plane waves:

$$\Psi(\boldsymbol{r}) = \begin{pmatrix} u_{\boldsymbol{k}} \\ \\ v_{\boldsymbol{k}} \end{pmatrix} e^{i\boldsymbol{k}\cdot\boldsymbol{r}} \tag{2.13}$$

For an isotropic s-wave pairing symmetry, the pair potential can be written as

$$\Delta(\boldsymbol{r}) = \Delta_0 e^{i\varphi}, \tag{2.14}$$

which has no momentum dependence with $\Delta_0 > 0$ and φ the phase of the order parameter.

After some algebra, we obtain the eigenfunctions

$$\psi_k^+ = \begin{pmatrix} u_0 \\ \\ v_0 \end{pmatrix} e^{i\boldsymbol{k}\cdot\boldsymbol{r}}$$
$$\psi_k^- = \begin{pmatrix} -v_0^* \\ \\ u_0^* \end{pmatrix} e^{i\boldsymbol{k}\cdot\boldsymbol{r}} \tag{2.15}$$

with eigenvalues

$$\pm E_k = \pm\sqrt{\Delta_0^2 + \varepsilon_k^2}\,, \tag{2.16}$$

where ε_k is the single-particle energy dispersion:

$$\varepsilon_k = \frac{\hbar^2 k^2}{2m} - E_F. \tag{2.17}$$

The coefficients of the BdG wavefunctions are

$$u_0 = e^{i\frac{\varphi}{2}}\sqrt{\frac{1}{2}\left(1 + \frac{\varepsilon}{E_k}\right)}$$
$$v_0 = e^{-i\frac{\varphi}{2}}\sqrt{\frac{1}{2}\left(1 - \frac{\varepsilon}{E_k}\right)}. \tag{2.18}$$

Eq.2.16 shows that for a real wavevector k, E_k is always larger than the pair potential Δ_0. In other words, there are no quasiparticle states for energies below Δ_0, forming the superconducting gap. More

explicitly, we can find the density of states for the Bogoliubov quasiparticles N_s from the dispersion

$$N_s(E) = \frac{1}{N}\sum_k \delta(E - E_k) = \frac{1}{N}\sum_k \left(E - \sqrt{\Delta_0^2 + \varepsilon_k^2}\right). \tag{2.19}$$

For simplicity, we assume the normal state density of states N_n is constant and equals to that at Fermi level, N_0. Then

$$\begin{aligned} N_s(E) &= \int_{-\infty}^{\infty} d\varepsilon N_n(E_F - \varepsilon)\ \delta\left(E - \sqrt{\Delta_0^2 + \varepsilon^2}\right) \\ &\cong N_0 \int_{-\infty}^{\infty} d\varepsilon\ \delta\left(E - \sqrt{\Delta_0^2 + \varepsilon^2}\right) \qquad (2.20) \\ &= N_0 \begin{cases} \frac{2E}{\sqrt{E^2 - \Delta_0^2}}\ , & \text{if } |E| > \Delta_0 \\ 0\ , & \text{if } |E| < \Delta_0. \end{cases} \qquad (2.21) \end{aligned}$$

Note that here the excitation energy E is relative to the Fermi level, so we are counting contributions from both electron and hole excitations to the density of states at E. It explains why from this derivation we get a factor of 2 in $N_s(E) \rightarrow 2N_0$ as $\Delta_0 \rightarrow 0$. The quasiparticle density of states N_s is shown in figure 2.2.

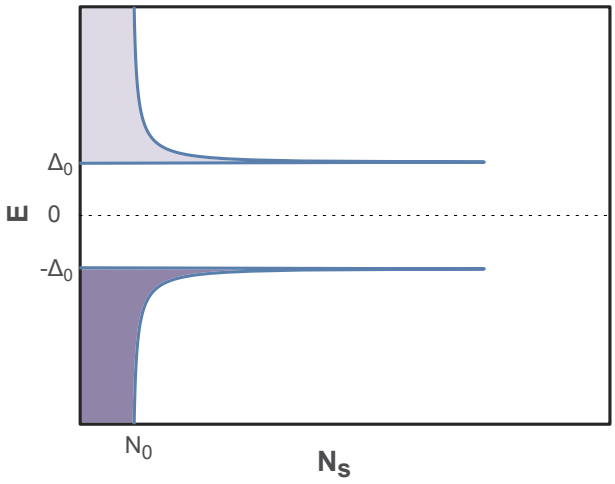

Figure 2.2: Quasiparticle density of states for an s-wave superconductor. There are no quasiparticle states for $|E| < \Delta_0$. In order to add or remove a quasiparticle from the ground state, a minimum energy of $2\Delta_0$ is required to overcome the superconducting gap.

2.3 Andreev Reflection at NS Interface

Now that we have the $H_{BdG}(\boldsymbol{r})$, both $U(\boldsymbol{r})$ and $\Delta(\boldsymbol{r})$ are spatially described. They become useful for studying what happens when we put a normal conductor (N) next to a superconductor (S).

2.3.1 Andreev reflection

It was already noticed from earlier experiments that the thermal resistance of superconductors in the intermediate states (which can be viewed as a series of alternating N/S regions) are greatly larger than the thermal resistance in both the normal and superconducting states. It implies there is a new resistance mechanism that is exclusive to the intermediate states, in which the population of electrons

decreases as one crosses the boundary between the normal and superconducting regions. [6,7] However, the nature of this type of scattering for electrons at the NS boundary was never clarified until A. F. Andreev did so by employing the BdG equations in 1964. [8] The process is now widely known as the Andreev reflection. Since single electronic states are prohibited in the superconducting quasiparticle energy gap, an electron with energy below the gap is not allowed to enter the superconductor. The Andreev reflection describes how the electron is coherently reflected as a hole from the NS interface while a charge of $-2e$ is transferred into the superconductor.

For generality, in the next section we will discuss the model developed by G. E. Blonder, M. Tinkham, and T. M. Klapwijk in 1982. [9] Same as Andreev's approach, they use the BdG equations to describe a hybrid system, but with an arbitrary transparency of the NS interface. From the BTK model, we can show that the Andreev reflection probability is 100% for an ideal interface. Furthermore, this model includes the contribution of subgap conductance from Andreev reflection and is extremely useful for experimentalists studying transport through NS junctions.

2.3.2 Blonder-Tinkham-Klapwijk (BTK) model

As shown in figure 2.3, our hybrid system has the NS interface at $x = 0$: normal region for $x < 0$ and superconducting region for $x > 0$. The pair potential can be written as

$$\Delta(x) = \Theta(x)\Delta_0 e^{i\varphi}, \tag{2.22}$$

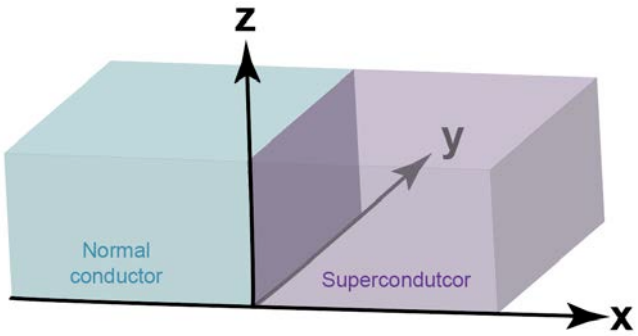

Figure 2.3: Normal/superconductor hybrid system.

where $\Theta(x)$ is a step function such that $\Theta(x) = 1$ for $x \geq 0$ and $\Theta(x) = 0$ for $x < 0$. $\Delta_0 e^{i\varphi}$ is the complex order parameter in the bulk superconductor. Since the transport properties are determined in details by the quasiparticle states produced by the interfacial scattering, a potential $H\delta(x)$ at the NS interface is added in the one-dimensional BdG Hamiltonian:

$$\begin{pmatrix} -\frac{\hbar^2}{2m}\frac{\partial^2}{\partial x^2} - E_F + H\delta(x) & \Delta(x) \\ \Delta^*(x) & \frac{\hbar^2}{2m}\frac{\partial^2}{\partial x^2} + E_F - H\delta(x) \end{pmatrix} \begin{pmatrix} u(x) \\ v(x) \end{pmatrix} = E \begin{pmatrix} u(x) \\ v(x) \end{pmatrix}. \tag{2.23}$$

For a given energy, Eq.2.23 allows two electron waves and two hole waves in N region ($x < 0$):

$$\psi_{\pm}^{e} = \begin{pmatrix} 1 \\ 0 \end{pmatrix} e^{\pm i q_e x} \quad \text{and} \quad \psi_{\pm}^{h} = \begin{pmatrix} 0 \\ 1 \end{pmatrix} e^{\pm i q_h x} \tag{2.24}$$

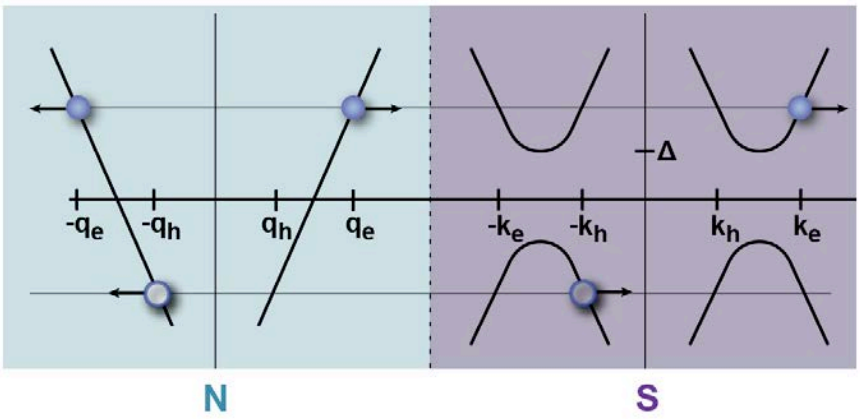

Figure 2.4: Energy vs momentum at NS interface with different types of quasiparticle wave.

Similarly, there can be two electron-like and two hole-like quasiparticle waves in S region ($x > 0$):

$$\psi_{\pm}^{e} = \begin{pmatrix} u_0\, e^{i\varphi/2} \\ v_0\, e^{-i\varphi/2} \end{pmatrix} e^{\pm i k_e x} \quad \text{and} \quad \psi_{\pm}^{h} = \begin{pmatrix} v_0\, e^{i\varphi/2} \\ u_0\, e^{-i\varphi/2} \end{pmatrix} e^{\pm i k_h x} \tag{2.25}$$

where

$$q_{e,h} = \frac{\sqrt{2m\left(E_F \pm E\right)}}{\hbar} \tag{2.26}$$

$$k_{e,h} = \frac{\sqrt{2m\left(E_F \pm \sqrt{E^2 - \Delta^2}\right)}}{\hbar} \tag{2.27}$$

and the coefficients are

$$u_0 = \sqrt{1 - v_0^2} = \sqrt{\frac{1}{2}\left(1 + \sqrt{1 - \left(\frac{\Delta_0}{E}\right)^2}\right)} \tag{2.28}$$

Different types of quasiparticle wave are illustrated in figure 2.4, where the arrows point in the direction of the group velocity. Note that when the momenta of electron and hole have the same sign, they are actually waves going towards the opposite directions.

Solving the scattering problem

For an electron in N that is impinging the NS interface (illustrated in figure 2.5), we have:

1. an incident plane wave
2. a reflected wave consisting of an electron part due to elastic scattering and a hole part due to interaction with the superconductor
3. a transmitted wave going into the superconductor

They can be written as

$$\psi_{inc} = \begin{pmatrix} 1 \\ 0 \end{pmatrix} e^{+iq_e x} \tag{2.29}$$

$$\psi_{refl} = r_{ee} \begin{pmatrix} 1 \\ 0 \end{pmatrix} e^{-iq_e x} + r_{he} \begin{pmatrix} 0 \\ 1 \end{pmatrix} e^{+iq_h x} \tag{2.30}$$

$$\psi_{trans} = t_{ee} \begin{pmatrix} u_0\, e^{i\varphi/2} \\ v_0\, e^{-i\varphi/2} \end{pmatrix} e^{+ik_e x} + t_{he} \begin{pmatrix} v_0\, e^{i\varphi/2} \\ u_0\, e^{-i\varphi/2} \end{pmatrix} e^{-ik_h x}, \tag{2.31}$$

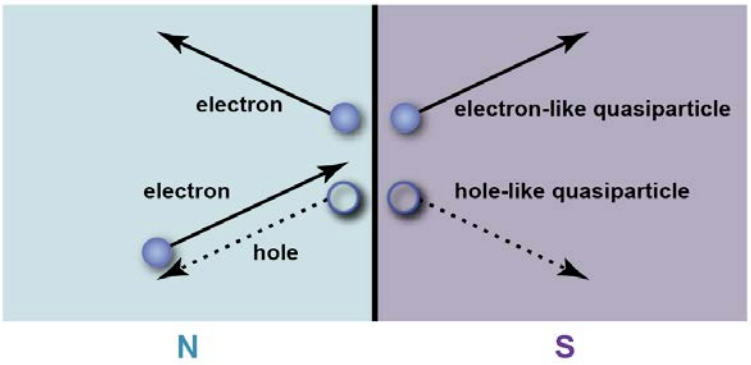

Figure 2.5: Scattering process at NS interface.

The wavefunctions describing the system are:

$$\psi_N = \psi_{inc} + \psi_{refl}, \quad \text{in N } (x < 0) \tag{2.32}$$

$$\psi_S = \psi_{trans} \quad , \quad \text{in S } (x > 0) \tag{2.33}$$

The scattering amplitudes $r_{ee}, r_{he}, t_{ee}, t_{he}$ can be determined through the given boundary conditions.

The continuity of wavefunctions at $x = 0$ requires:

$$\psi_N(0) = \psi_S(0). \tag{2.34}$$

And in view of the δ-function potential we have:

$$\frac{\hbar}{2m}\left[\psi'_S(0) \; - \; \psi'_N(0)\right] = H\psi(0) \tag{2.35}$$

with $\psi'_{S,N}$ the spatial derivatives.

Then by working out the algebra, we find the amplitude (for convenience, $\gamma = u_0^2 + (u_0^2 - v_0^2)Z^2$) and hence the probability of all four processes:

$$r_{he} = \frac{u_0 v_0}{\gamma} e^{-i\varphi} \tag{2.36}$$

$$r_{ee} = \frac{(v_0^2 - u_0^2)\,(Z^2 + iZ)}{\gamma} \tag{2.37}$$

$$t_{ee} = \frac{u_0\,\sqrt{u_0^2 - v_0^2}\,(1 - iZ)}{\gamma} e^{-i\varphi/2} \tag{2.38}$$

$$t_{he} = \frac{iv_0\,\sqrt{u_0^2 - v_0^2}\,Z}{\gamma} e^{-i\varphi/2}, \tag{2.39}$$

where Z is a new dimensionless parameter defined as

$$Z \equiv \frac{H}{\hbar v_F}. \tag{2.40}$$

Importance of the parameter Z

Note that for any real interface with different materials having different Fermi-momenta, there will be an electronic mismatch. When we determine the amplitudes in Eq.2.36-2.39, it is assumed the Fermi velocities are the same for N and S with the Andreev approximation:

$$E, \Delta_0 \ll E_F. \tag{2.41}$$

Andreev noticed the curious feature of hole retroreflection, i.e., momentum conservation that is absent in normal reflection. However, without the condition Eq.2.41, the Andreev reflection is a perfect retroreflection only for electrons incident at the Fermi energy. When the energy is above the Fermi energy, the incident electron $(E_F + E, k_F + \delta k/2)$ and the reflected hole $(E_F - E, k_F - \delta k/2)$ have different wavelengths. The mismatch $\delta k = 2E/\hbar v_F$ is linear in energy and can be absorbed by the adjustable Z in the BTK model.

Obviously, in a normal conductor ($\Delta_0 = 0$), we have $u_0 = 1, v_0 = 0$; the probabilities $|r_{he}|^2, |t_{he}|^2$ both vanish, leaving

$$|r_{ee}|^2 = \frac{Z^2}{1+Z^2}, \quad \text{probability of normal state reflection} \tag{2.42}$$

$$|t_{ee}|^2 = \frac{1}{1+Z^2}, \quad \text{probability of normal state transmission.} \tag{2.43}$$

So now it is clear that Z can be understood as the strength of the interface barrier. For $Z = 0$, we have a perfectly transparent interface with perfect normal state transmission $|t_{ee}|^2 = 1$. For $Z \gg 1$, we have an opaque interface with very low transmission.

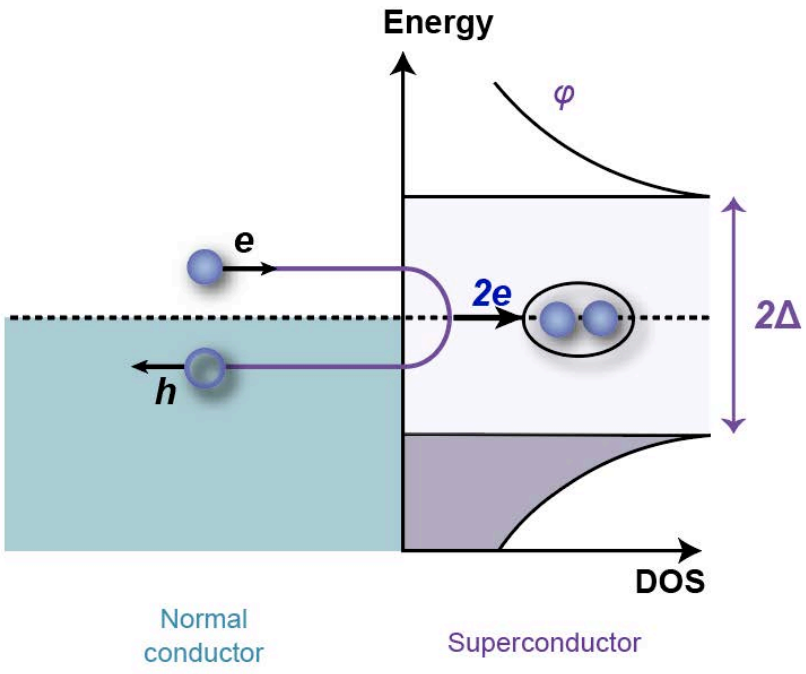

Figure 2.6: Sketch of Andreev reflection.

Andreev reflection for an ideal NS interface

In the case of perfectly transparent interface ($Z = 0$), the amplitude of the process having an electron reflected as a hole becomes

$$r_{he} = \frac{v_0}{u_0}\, e^{-i\varphi} = e^{-i\chi} = \begin{cases} e^{-i\varphi}\left(\frac{E - sgn(E)\sqrt{E^2-\Delta_0^2}}{\Delta_0}\right), & |E| > \Delta_0 \\ e^{-i\varphi}\left(\frac{E - i\sqrt{E^2-\Delta_0^2}}{\Delta_0}\right), & |E| < \Delta_0 \end{cases} \tag{2.44}$$

$$\chi = \begin{cases} \varphi\,, & E < -\Delta_0 \\ \varphi + \arccos\left(\frac{E}{\Delta_0}\right);, & |E| < \Delta_0 \\ \varphi + \pi\,, & E > \Delta_0 \end{cases} \tag{2.45}$$

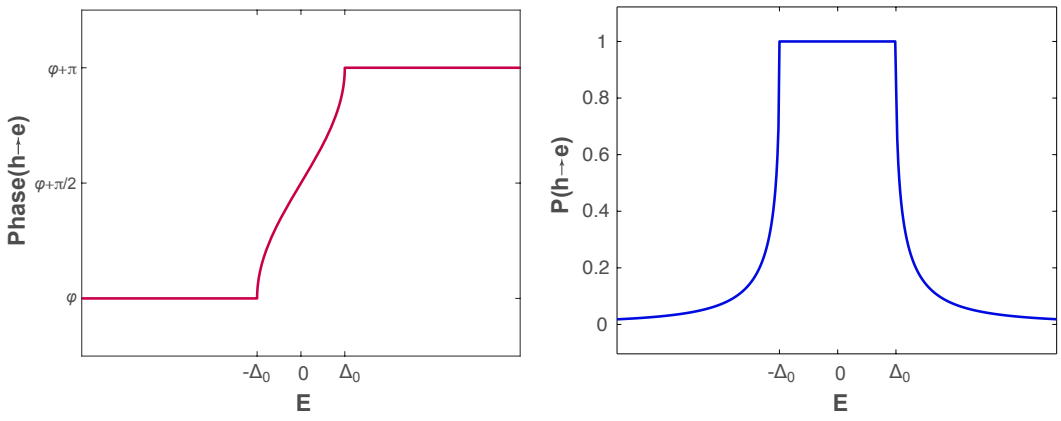

Figure 2.7: Energy-dependent phase and probability ($P(h \rightarrow e) = |r_{he}|^2$) of Andreev reflection for an ideal interface ($Z = 0$).

where u_0, v_0 are given in Eq.2.28.

The most important property of proximity effect is phase coherence. We now can see from r_{he} that the Andreev reflected hole has a phase shift χ with respect to the incident electron, as illustrated in the left panel of figure 2.7. It carries not only the information of the superconductor (via the macroscopic phase φ), but also of the incident electron (via the energy-dependent phase).

The right panel of figure 2.7 shows the probability of Andreev reflection as a function of the energy of the incident electron. For a transparent interface, an injected electron with energies above the superconducting gap has finite probability (though dropping rather fast) to be transmitted into the superconductor. But with energies below the gap, Andreev reflection must happen and it converts a dissipative current in the normal conductor into a dissipationless supercurrent in the superconductor.

2.3.3 Tunneling conductance through NS junction

BTK continues on to discuss the transport properties of NS junction. For a system with normal electrodes (denoted by L and R), the Landauer-Büttiker expression for single channel current is

$$\begin{aligned} I &= \frac{2e}{h} \int dE \ |t_{ee}|^2 \left(f_L(E) - f_R(E)\right) \\ &= \frac{2e}{h} \int dE \ \left(1 - |r_{ee}|^2\right) \left(f_L(E) - f_R(E)\right) \end{aligned} \tag{2.46}$$

In the case of NS junction with one normal electrode and one superconducting electrode, the Andreev reflection increases the total current by transferring a charge of $2e$ into the S side. So the formula should become (at zero temperature):

$$I = \frac{2e}{h} \int_0^{eV} dE \ \left(1 - |r_{ee}(E)|^2 + |r_{he}(E)|^2\right), \tag{2.47}$$

where we have set the chemical potential of the leads to be

$$\mu_L = E_F + eV, \quad \mu_R = E_F \quad (V > 0). \tag{2.48}$$

Note that the voltage V is small such that r_{ee}, r_{he} are evaluated at the Fermi energy. The conductance through the NS junction is then

$$G_{NS} = \frac{dI}{dV} = \frac{2e^2}{h}\left(1 - |r_{ee}(eV)|^2 + |r_{he}(eV)|^2\right) \tag{2.49}$$

$$= \frac{2e^2}{h}\begin{cases} \frac{2\Delta_0^2}{(eV)^2+(1+2Z^2)^2(\Delta_0^2-(eV)^2)}, & eV < \Delta_0 \\ \frac{2eV}{eV+(1+2Z^2)\sqrt{(eV)^2-\Delta_0^2}}, & eV > \Delta_0. \end{cases} \tag{2.50}$$

If the voltage is much greater than the superconducting gap ($eV \gg \Delta_0$), we obtain the normal conductance

$$G_{NN} = \frac{2e^2}{h}\frac{1}{1+Z^2}. \tag{2.51}$$

To get a better physical intuition, let us consider a perfect interface where $Z = 0$. Then we have $|r_{he}|^2 = 1$ and $|r_{ee}|^2 = 0$. For the subgap regime $eV < \Delta_0$, conductance through the NS junction becomes twice of the normal conductance:

$$G_{NS} = \frac{4e^2}{h} = 2\,G_{NN}. \tag{2.52}$$

BTK model is useful as a guidance for finding the transparency of an NS interface from the transport properties. Figure 2.8 shows the normalized conductance (G_{NS}/G_{NN}) as a function of the bias voltage for a few different values of the parameter Z, which represents the barrier strength. In Chapter

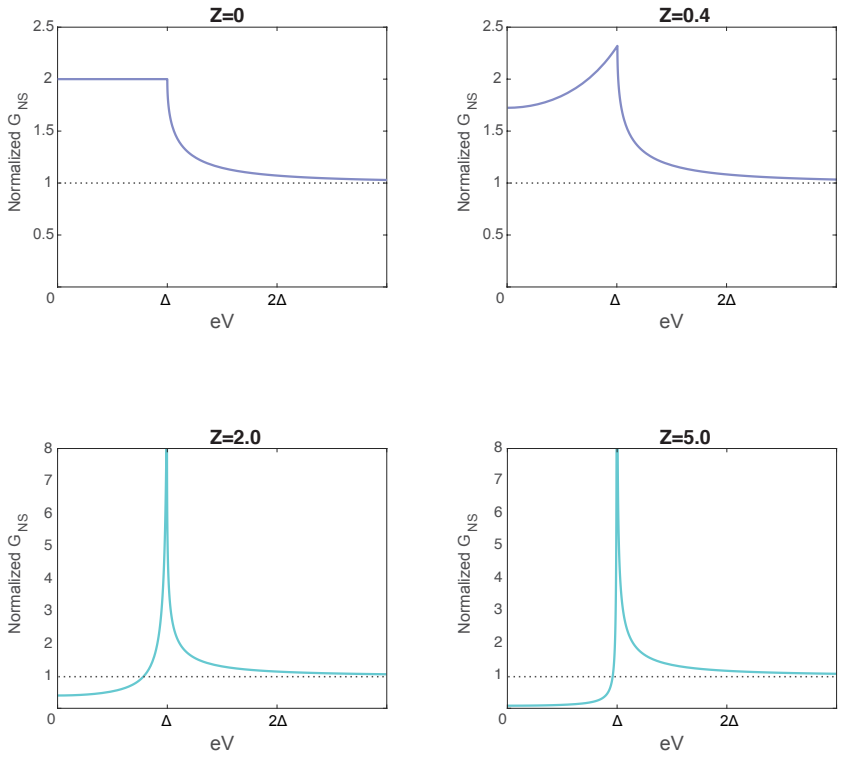

Figure 2.8: Normalized conductance across the NS junction with different interface transparency Z. Top panel: for Z=0, the interface is perfectly transparent and the conductance is doubled inside the gap compared to the normal conductance. For Z=0.4, there is still conductance enhancement inside the gap. Bottom panel: as Z is increased to 2.0, the NS junction enters the tunneling regime. There is conductance suppression inside the gap. For Z=5.0, the contact is opaque. The tunneling conductance inside the gap almost reaches zero, similar to the scenario of probing the quasiparticle density of states in a superconductor (figure 2.2).

3 we will compare the experimental results to these subfigures and decide different interface regimes

the devices fall into.

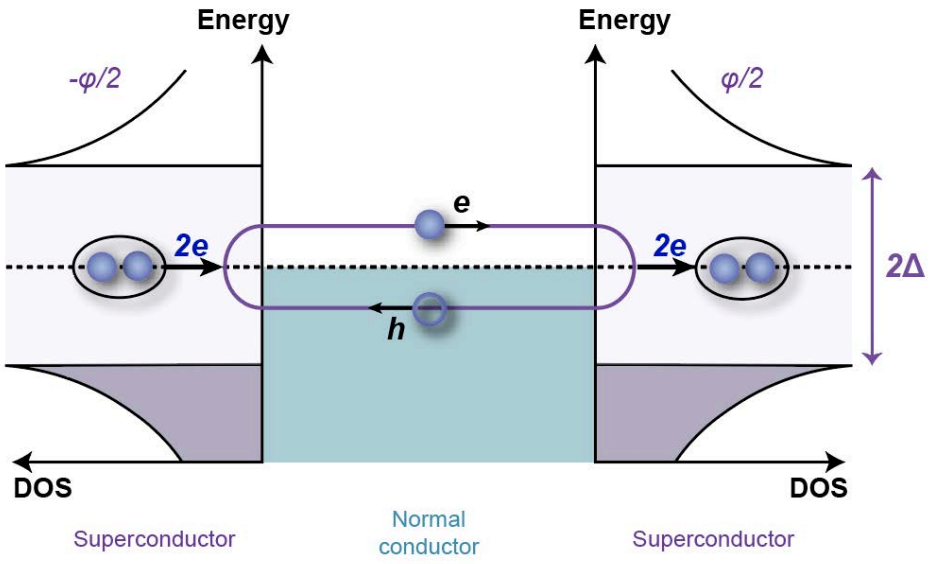

Figure 2.9: Formation of Andreev bound states originates from the successive Andrrev reflections at the two NS interfaces.

2.4 Andreev Bound States in SNS Junctions

In the previous section we discussed one NS interface, where an excitation with energy above Fermi level (an electron) is reflected as a hole with energy below Fermi level, and vice versa. Now let us consider a normal conductor that is sandwiched between two superconductors, i.e., an SNS junction. As a result of the successive Andreev reflections from both NS interfaces, the excitation will carry out periodic motions as shown in figure 2.9: being an electron for half of the time and a hole for the other. Standing waves form in the normal region and lead to the quantization of the excitation energy levels. This is the problem solved by Andreev[10] in 1966 and the excitations are known as the "Andreev bound states" (ABS).

This quantization implies coherence between the phases of the two superconductors and hence throughout the entire SNS junction. Just a few years earlier, in 1962, based on quantum mechanical tunneling of electrons through a barrier layer, B. D. Josephson predicted that a zero-voltage current can flow between two superconductors through a thin insulator, driven by the phase difference across the junction. The is known as the DC Josephson effect, a general feature of two superconductors that are connected by any weak link (besides an insulator as Josephson envisioned, it can also be a normal metal or a point contact). In the early 1970s, the importance of ABS was already recognized in connection to the DC Josephson effect in long SNS junctions[11] (where the junction length L is longer than the superconducting coherence length $\xi_0 = \hbar v_F/\Delta_0$). However, it was only till the 1990s that these supercurrent-carrying states are demonstrated to play a central role in Josephson junctions with point contacts and tunnel junctions.[12,13] The complete solution of scattering theory can be found in Beenakker's work,[14] with scattering matrices constructed for the normal region and Andreev reflection. The determinant equation giving ABS energies is still widely used in the study of NS hybrid systems. For our purpose, we will only focus on the case where $L < \xi_0$. Now let us follow the similar steps as in the previous section so we can find the wave functions and energy levels in a short SNS junction .

2.4.1 Scattering picture

We start with the same BdG equation (Eq.2.23) but instead of an NS interface, we now have a short SNS junction. It means that the normal region is thin and we consider it having infinitesimal thickness.

The pair potential is then described as

$$\Delta(x) = \begin{cases} \Delta_0\, e^{i\varphi_L}\,, & x < 0 \\ \Delta_0\, e^{i\varphi_R}\,, & x > 0 \end{cases} \tag{2.53}$$

We are interested in the state below the energy gap and we already know that for $E < \Delta_0$, the wave function in S has to decay exponentially and can be written as (same as ψ_{trans} in the superconductor in Eq.2.31)

$$\psi_S = \begin{cases} t_{ee}^L \begin{pmatrix} u_0\, e^{i\varphi_L/2} \\ v_0\, e^{-i\varphi_L/2} \end{pmatrix} e^{-ik_e x} + t_{he}^L \begin{pmatrix} v_0\, e^{i\varphi_L/2} \\ u_0\, e^{-i\varphi_L/2} \end{pmatrix} e^{+ik_h x}\,, & x < 0 \\ t_{ee}^R \begin{pmatrix} u_0\, e^{i\varphi_R/2} \\ v_0\, e^{-i\varphi_R/2} \end{pmatrix} e^{+ik_e x} + t_{he}^R \begin{pmatrix} v_0\, e^{i\varphi_R/2} \\ u_0\, e^{-i\varphi_R/2} \end{pmatrix} e^{-ik_h x}\,, & x > 0 \end{cases} \tag{2.54}$$

Again, the coefficients $t_{ee}^L, t_{he}^L, t_{ee}^R, t_{he}^R$ are determined from the boundary conditions at $x = 0$:

$$\psi_S(0^-) = \psi_S(0^+) \quad \text{and} \quad \frac{\hbar}{2m}\left[\psi_S'(0) - \psi_S'(0)\right] = H\psi_S(0) \tag{2.55}$$

Using the Andreev approximation ($E, \Delta_0 \ll E_F$ and hence $k_e \approx k_h \approx k_F$), we find[13]

$$E = \pm\Delta_0 \sqrt{\frac{\cos^2(\varphi/2) + Z^2}{1 + Z^2}}, \tag{2.56}$$

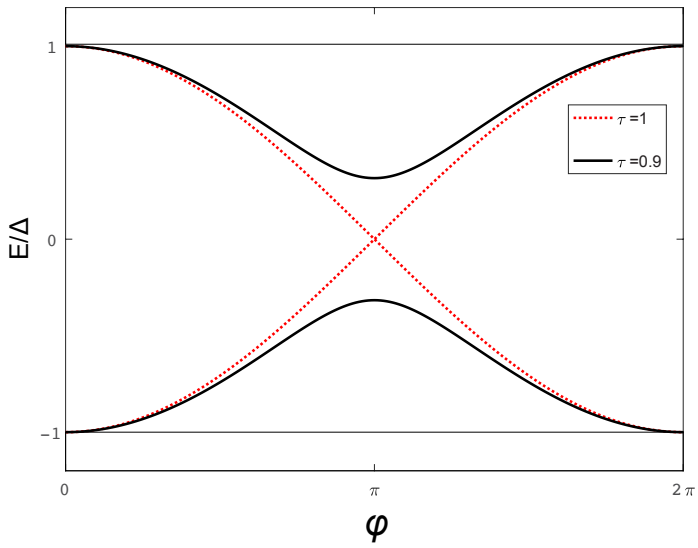

Figure 2.10: Energy of the Andreev bound states as a function of the superconducting phase across the junction.

where $\varphi = \varphi_R - \varphi_L$. By denoting the normal state transmission probability $|t_{ee}|^2$ as τ and using the relation Eq.2.43, we arrive at the expression of Andreev levels for short junctions

$$E_{ABS} = \pm\Delta_0\sqrt{1 - \tau\sin^2(\varphi/2)}. \tag{2.57}$$

Figure 2.10 shows the energy dispersion of the Andreev bound states as a function of φ, the superconducting phase across the junction.

2.4.2 Infinite-gap dot model

We will now turn to a quantum dot model in the infinite-gap limit. It is simple enough to be generalized to an n-terminal Josephson junction ($n > 2$), which will be discussed in the later chapters.

Consider a Josephson junction made of a normal quantum dot island connected to several superconducting terminals. This dot with single-level energy ε_0 is coupled to the superconductors via tunneling. In the infinite-gap limit, the superconducting gap is the dominant energy (much larger than the couplings and ε_0).

With a finite pair potential, an electron with energy ε_0 is coupled to a hole with energy $-\varepsilon_0$ through the Andreev reflection, which happens at the point contact between the normal dot island and each superconducting contact. The Hamiltonian is given by[15]

$$H = \begin{pmatrix} \varepsilon_0 & \sum_i \gamma_i e^{i\varphi_i} \\ \sum_i \gamma_i e^{-i\varphi_i} & -\varepsilon_0 \end{pmatrix}, \tag{2.58}$$

where φ_i's are the superconducting phases of each terminal and γ_i's are the coupling coefficients describing the tunneling of Cooper pair between the dot and the superconductors. Note that γ's are real since from a microscopic point of view, the Hamiltonian gives that γ is proportional to $|T|^2$, where T is a single electron transfer matrix element.

The Schrödinger equations for the wavefunction with electron and hole components (ψ_e, ψ_h) are

$$\begin{aligned} \varepsilon_0 \psi_e + \sum_i \gamma_i e^{i\varphi_i} \psi_h &= E\psi_e \\ \sum_i \gamma_i e^{-i\varphi_i} \psi_e - \varepsilon_0 \psi_h &= E\psi_h \end{aligned} \tag{2.59}$$

Solving for the eigenvalues we get the Andreev bound state energies

$$E_{ABS} = \pm \sqrt{\varepsilon_0^2 + |\sum_i \gamma_i e^{i\varphi_i}|^2} \tag{2.60}$$

For example, a two-terminal SNS junction has ABS energies:

$$E_{ABS} = \pm \sqrt{\varepsilon_0^2 + \left|\gamma_1 + \gamma_2 e^{i\varphi}\right|^2}, \tag{2.61}$$

where φ is the phase difference between the two superconductors. The numerical results of a two-terminal junction in the dot model is shown in figure 2.11.

One would notice immediately the resemblance between figure 2.10 and 2.11. When obtained from a single channel in scattering theory (Eq.2.57), the ABS becomes $E = \pm\Delta_0 \cos(\varphi/2)$ for perfect transmission ($\tau = 1$). In the case of a resonant dot ($\varepsilon_0 = 0$), the symmetric contact couplings corresponds to perfect transmission, and hence produce also a 4π- periodic function. In the scattering case, an infinitesimal deviation of τ from unity would open up an Andreev gap around $\varphi = \pi$, doubling the periodicity. However, in the dot case, the gap forms due to both the coupling asymmetries and

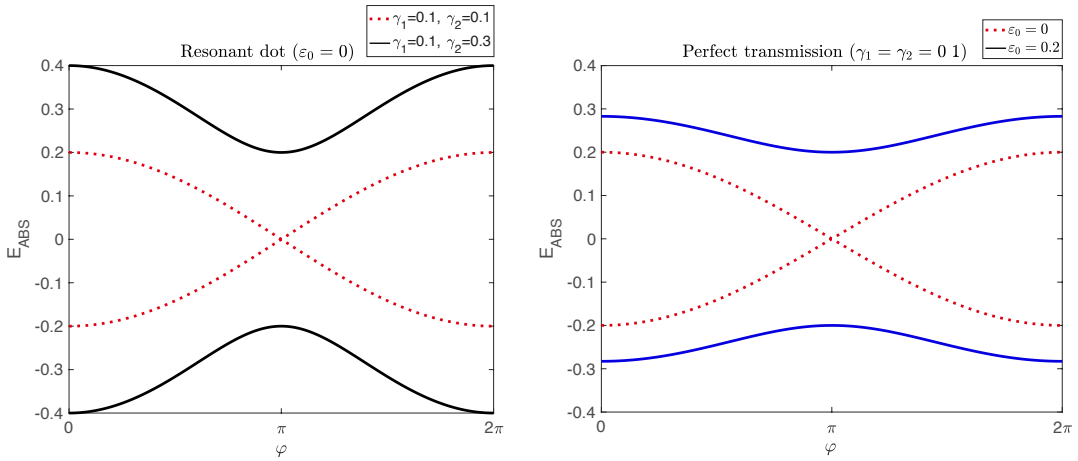

Figure 2.11: $E_{ABS}(\varphi)$ for perfect transmission in a resonant dot (red dotted line) and with other values of γ and ε_0 (black/blue lines).

the shift of ε_0.

Yet the biggest difference between the two models is the presence of the superconducting gap. In the scattering case $E = \pm\Delta_0$ at $\varphi = 0$, the states are not really bound but exist at the edges of the continuous quasiparticle spectrum in the superconductor. However, in the dot model, the whole spectrum is inside the gap and will never touch the gap edges. The underlying flaw of the dot model is exposed if the contact couplings or ε_0 become large compared to the gap Δ_0 ; we will find the ABS above the gap, which is obviously beyond the original assumption. The infinite-gap approximation indeed has its limit, but is good enough for capturing low-energy physics and will provide a simple analytic expression one can consider when the system becomes more complicated.

2.4.3 Supercurrent carried by ABS in short junctions

The ground-state energy of our SNS system has contributions from all excitation energies, including the propagating quasiparticles above the superconducting gap and the Andreev bound states inside the gap. But let us focus on the latter now since it is the only energy that is dependent on φ, the phase difference across the junction. If we vary the phase difference slowly, the energy shift per unit time is then given by

$$\frac{dE}{dt} = \frac{\partial E(\varphi)}{\partial \varphi}\frac{d\varphi}{dt}, \tag{2.62}$$

which is the power dissipated at the junction (product of the current and the voltage). Due to the global gauge invariance,* the time derivative of the superconducting phase is simply the potential of the superconductor,

$$\frac{d\varphi}{dt} = \frac{2eV}{\hbar} \tag{2.63}$$

*The global gauge invariance requires that the phase and the vector potential always come in the combination $\boldsymbol{\nabla}\varphi - (2e/\hbar)\boldsymbol{A}$. It leads to the fundamental relation in Josephson junctions: $\varphi = 2\pi\Phi/\Phi_0$, where $\Phi_0 \equiv h/2e$. Using Faraday's law we can get Eq.2.63, which is known as the 2nd Josephson relation.

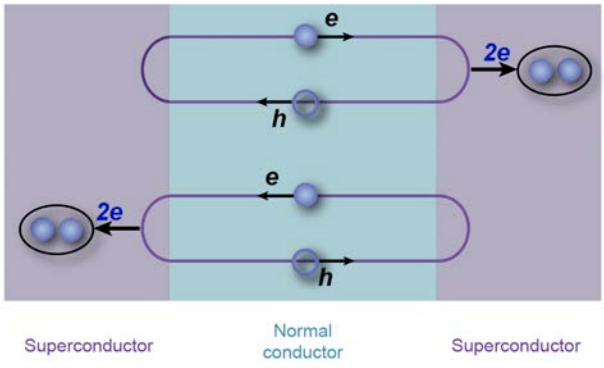

Figure 2.12: Andreev bound states that carry opposite directions of supercurrents.

Therefore, the current in the junction can be calculated from taking derivative of the energy with respect to the phase difference:

$$I(\varphi) = \frac{2e}{\hbar}\frac{dE}{d\varphi} \tag{2.64}$$

Using the energy obtained from the scattering theory (Eq.2.57), we get

$$I_{ABS,|-\rangle} = \frac{e\Delta_0}{2\hbar}\frac{\tau \sin\varphi}{\sqrt{1-\tau\sin^2(\varphi/2)}} \tag{2.65}$$

$$I_{ABS,|+\rangle} = -\frac{e\Delta_0}{2\hbar}\frac{\tau \sin\varphi}{\sqrt{1-\tau\sin^2(\varphi/2)}} \tag{2.66}$$

It is now clear that the ground state and excited state describe the two processes in figure 2.12, which differ in the direction of electron and hole propagation, corresponding to supercurrents flowing in opposite directions.

In the above discussions we only considered a single channel in a one-dimensional junction. For a

multi-channel junction, we have

$$E = \pm\Delta_0\sqrt{1 - \tau_i \sin^2(\varphi/2)}, \tag{2.67}$$

where the index i labels the transverse modes in the normal region and τ_i is the individual transmission coefficients, which is essential in determining the current-phase relation.

For example, in a tunnel junction ($\tau_i \ll 1$), the supercurrent reads [†]

$$I(\varphi) = I_c \sin\varphi \ , \quad I_c = \frac{e\Delta_0}{2\hbar}\sum_{i=1}^{N}\tau_i = \frac{\pi\Delta_0}{2e}G_N. \tag{2.68}$$

Or in a quantum point contact ($\tau_i = 1$), the supercurrent is

$$I(\varphi) = I_c \sin(\varphi/2) \ , \quad I_c = \frac{e\Delta_0}{\hbar}\sum_{i=1}^{N}\tau_i = \frac{\pi\Delta_0}{e}G_N. \tag{2.69}$$

Here G_N is the normal state conductance, given in the Landauer formalism.

Supercurrent at finite temperature

At zero temperature, only the ground state is occupied and the supercurrent flowing in the junction is given by Eq.2.65. But at finite temperature, we will have to take into account the thermal population of the excited states (and depopulation of the ground states), determined by the Fermi-Dirac distribution

[†] Josephson made his predictions based on tunneling of electrons through an insulator barrier. Historically, the first superconducting junctions were also SIS junctions. Eq.2.68 is known as the first Josephson relation.

function:

$$f(E) = \frac{1}{1 + \exp(E/k_B T)}. \tag{2.70}$$

Then the supercurrent becomes

$$I(\varphi) = I_{ABS,|+\rangle} f_+(E) + I_{ABS,|-\rangle} f_-(E) \tag{2.71}$$

$$= I_{ABS}[1 - 2f(E)], \tag{2.72}$$

with $I_{ABS} = I_{ABS,|-\rangle} = -I_{ABS,|+\rangle}$ and by definition $f_+(E) + f_-(E) = 1$. This will lead to

$$I(\varphi) = \frac{e\Delta_0}{2\hbar} \frac{\tau \sin\varphi}{\sqrt{1 - \tau \sin^2(\varphi/2)}} \tanh\left(\frac{\Delta_0}{2k_B T}\sqrt{1 - \tau \sin^2(\varphi/2)}\right) \tag{2.73}$$

Up to this point, we have enough background information to understand the experimental studies. In the next chapter, we will concentrate on the graphene-superconductor interface, where the BTK model introduced earlier is going to be useful for characterizing the contact transparency. In Chapter 4 and 5, multi-terminal SNS junctions are explored and the simple quantum dot model will help us grasp the physical picture of the system.

3

Magnetoresistance Plateaus in Proximitized Graphene

Graphene has proven to be a great platform for the study of the superconductivity proximity effect. However, despite the fact that superconducting contacts can be established on graphene

with high yield compared to other semiconductors, the fabrication results are never perfect. Since the contact transparency between the normal conductor and the superconductor plays a pivotal role in the Andreev process as we discussed in Chapter 2, the resulting proximity effect can alter the properties in the normal region in several different ways.

To better understand the different superconducting behaviors stemming from the transparency of the contacts, we decided to take an extensive approach and study all three possible regimes that the superconductivity proximity effect can fall into. These regimes depend on the Andreev process probability, i.e., it depends on the transparency of the superconducting contacts, and they are called: the tunneling, intermediate and transpartent regime.

In this chapter, we will walk the reader through the device planning and then proceed to our experimental findings. As expected, we see that the proximitized graphene in the tunneling and transparent regime show conductance suppression and conductance enhancement, respectively and the variations would gradually flatten out as the magnetic field is increased. The intermediate regime, however, presented a surprise. Unseen in the other regimes, the proximitized graphene in the intermediate regime showed magnetoresistance plateaus. The origin and nature of the plateaus will be discussed.

3.1 Device Structure and Measurement Setup

The device structure that we chose to use throughout our study consists of a top superconducting contact on graphene, which sits on top of hexagonal boron nitride (hBN) (shown in figure 3.1). In

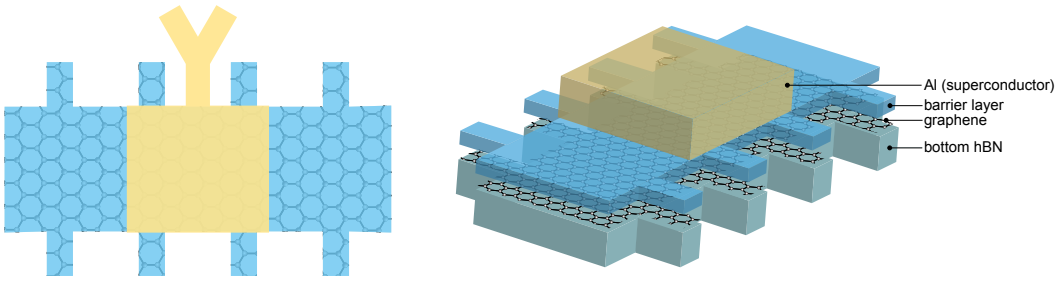

Figure 3.1: Illustration of the device structure, top and side view. Barrier layer can be thin hBN or MoS_2.

between the superconductor and graphene we can insert another layer. The role of this layer is to tune the transparency of the interface between the superconductor and graphene. The strategy is then to study how transport across this interface changes as we vary the transparency of the superconducting contact. This is where we face the main challenge: how can we deterministically vary this transparency? The natural solution here is to use other van der Waals materials as the barrier layer.

First and foremost, materials besides the van der Waals family should not be considered. Materials like evaporated aluminum oxide could work in theory but in reality, the associated fabrication process would bring about plenty of other complications such as polymer residue and graphene degradation. Van der Waals materials on the other hand give us two distinct advantages. One is that we can fine-tune the material thickness by a single atomic layer. The second is that these materials ensure the interface with graphene will be atomically flat and polymer-free. Within the van der Waals family, there exist many materials that range from insulating to semiconducting and then to completely conducting. Among them, we chose to use two as the interfacial layer: hBN and molybdenum disulfide (MoS2). These two materials offer bandgaps of different sizes (1.8 eV for MoS_2, 6.1 eV for hBN) which can help tune the contact transparency. Moreover, these materials frequently appear in large sizes, in different

thicknesses after mechanical exfoliation (compared to other van der Waals materials) and can be in the thin limit with just a few layers. These are important traits that allow us to fast-track the fabrication process.

Another important reason for choosing hBN and MoS_2 is that among all van der Waals materials, they have been used the most extensively since the advent of graphene and are considered the most pristine van der Waals materials besides graphene. The growth of these materials has reached a high level of perfection which gives us much greater confidence in their overall quality, a key consideration in our experiments in order for the superconducting contacts to work consistently.

3.1.1 Vertical graphene-insulator-superconductor architecture

The van der Waals vertical structure is built by the inverted dry transfer technique (see details in Appendix A). The bottom layer is a thick, clean flake of hBN (20-40 nm), creating a uniform substrate for graphene to minimize the disorder. On top of graphene is the barrier layer, which can be thin (monolayer, bilayer, etc) hBN or MoS_2. Unlike the usual dry transfer technique, , with the inverted technique the top surface of the stack is never in contact with any polymer such as PPC or PC. After the stack is assembled, the hallbar geometry is defined followed by deposition of normal leads (5/50 nm of Cr/Au). The device then undergoes the process of vacuum annealing at 350°C for 15-20 minutes to remove any PMMA residue from e-beam lithography, so that we can guarantee the tunnel path from graphene through the barrier layer to the superconductor is clean. The final step is deposition of the superconducting contacts (5/80 nm of Ti/Al) on top of the area of interest.

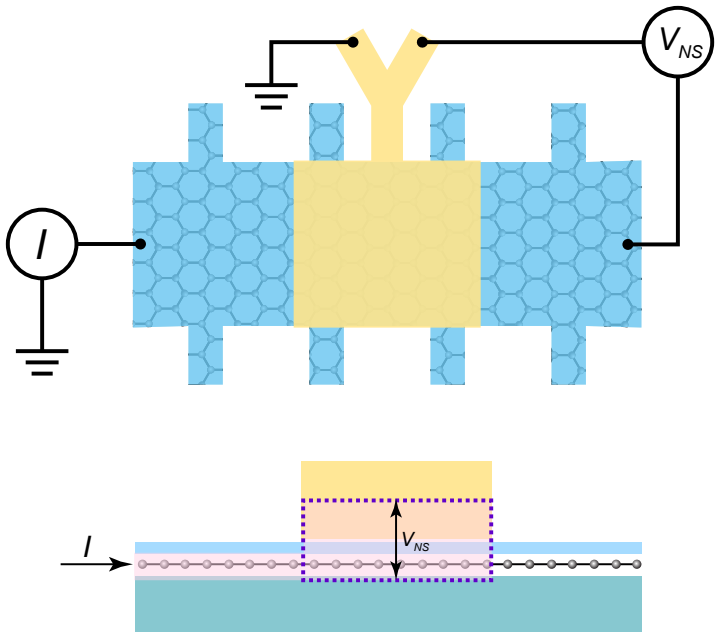

Figure 3.2: Measurement configuration of the vertical graphene/barrier/superconductor structure. The pink region denotes the current path (I) from a graphene normal contact at one end to the first lead of Al. The voltage drop across the vertical junction, V_{NS}, is measured from the other end of graphene to the second lead of Al.

3.1.2 Measurement Setup

The critical temperature of Al in the devices is typically around 1 K. All the measurements were performed in He3-fridge with a base temperature of 300 mK. The main focus is the graphene region underneath Al, where the superconducting proximity correlation is the strongest. As shown in figure 3.2, the Al contact branches out to two leads. The current is sent from a normal contact at the left end of graphene to the first Al lead, which is grounded. Then we measure the voltage V_{NS} between the other end of the graphene and the second Al lead. This is effectively the voltage drop across the vertical

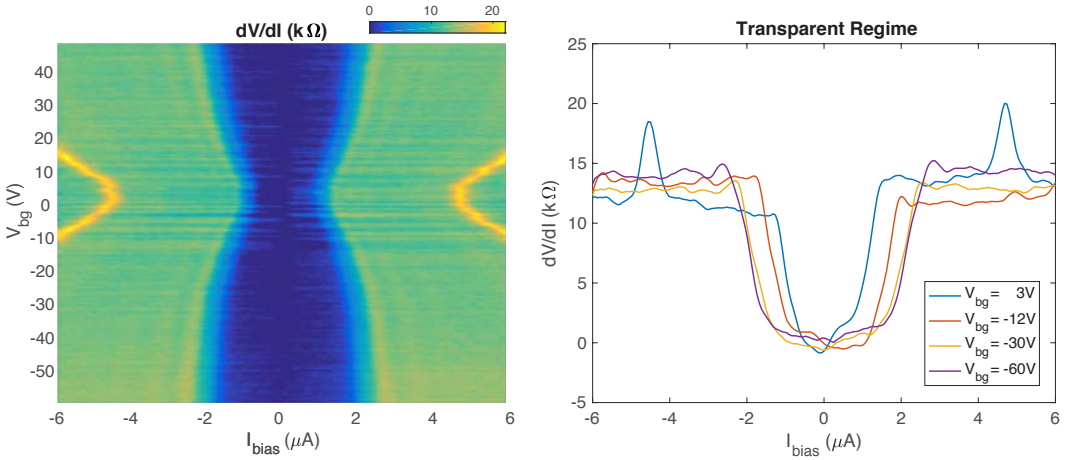

Figure 3.3: Gate dependence of tunneling resistance dV/dI in the transparent regime. The proximitized superconducting gap can be tuned by backgate voltage, where the minimum appears at the graphene Dirac peak ($V_{bg} = 3$ V).

graphene/barrier/Al structure, as marked by the dotted square in the bottom panel of figure 3.2. As a result, we obtain the tunneling conductance (or resistance) across the vertical NS junction, which characterizes the Andreev process in the system via the BTK model introduced in Chapter 2. With this measurement scheme, we categorize our devices into three regimes depending on the differential conductance profile.

3.2 Transparent Regime: Al/Graphene

As a reference point in this study, we start with a device without any barrier layer– Al is deposited directly on top of graphene. The graphene in this type of device becomes fully proximitized due to

the highly transparent superconducting contact.

Figure 3.3 shows the differential resistance dV/dI as a function of current bias and backgate voltage. In the color plot, it is clear that there is a gap feature, in which the resistance drops to near zero (deep blue region), signifying the presence of superconductivity. At the Dirac peak of graphene, where $V_{bg} = 3$ V across 300 nm SiO_2 dielectric, the superconducting gap reaches a minimum. As the carrier density in graphene is increased , the gap becomes larger. This backgate dependence suggests that we are measuring the induced superconducting gap in graphene, thereby eliminating doubts that we may be measuring the bulk Al superconducting contacts instead.

In figure 3.4, we plot the differential resistance as a function of current bias and applied magnetic field. In this figure, one can see how the induced gap (deep blue region) closes as the magnetic field approaches a critical field H_c. In addition, there are oscillations formed outside of the gap. These oscillations fan out from the superconducting gap and only exist in the superconducting regime (i.e., they also get quenched when the applied magnetic field rises above the critical field). We attribute these oscillations to Tomasch oscillations.[16,17,18] They arise specifically in superconductor-normal metal junctions when the electron- and hole-like quasiparticles are locked into strong confinement and are forced to interfere. The constructive interference results in the oscillations that we detect and occur at bias

$$V_n = \sqrt{\Delta^2 + \left(nhv_F^s/2d_s\right)^2} \quad \text{with } n = 0, 1, 2... \tag{3.1}$$

where Δ is the superconducting gap, V_F^s is the Fermi velocity in the superconductor and d_s is its thickness.

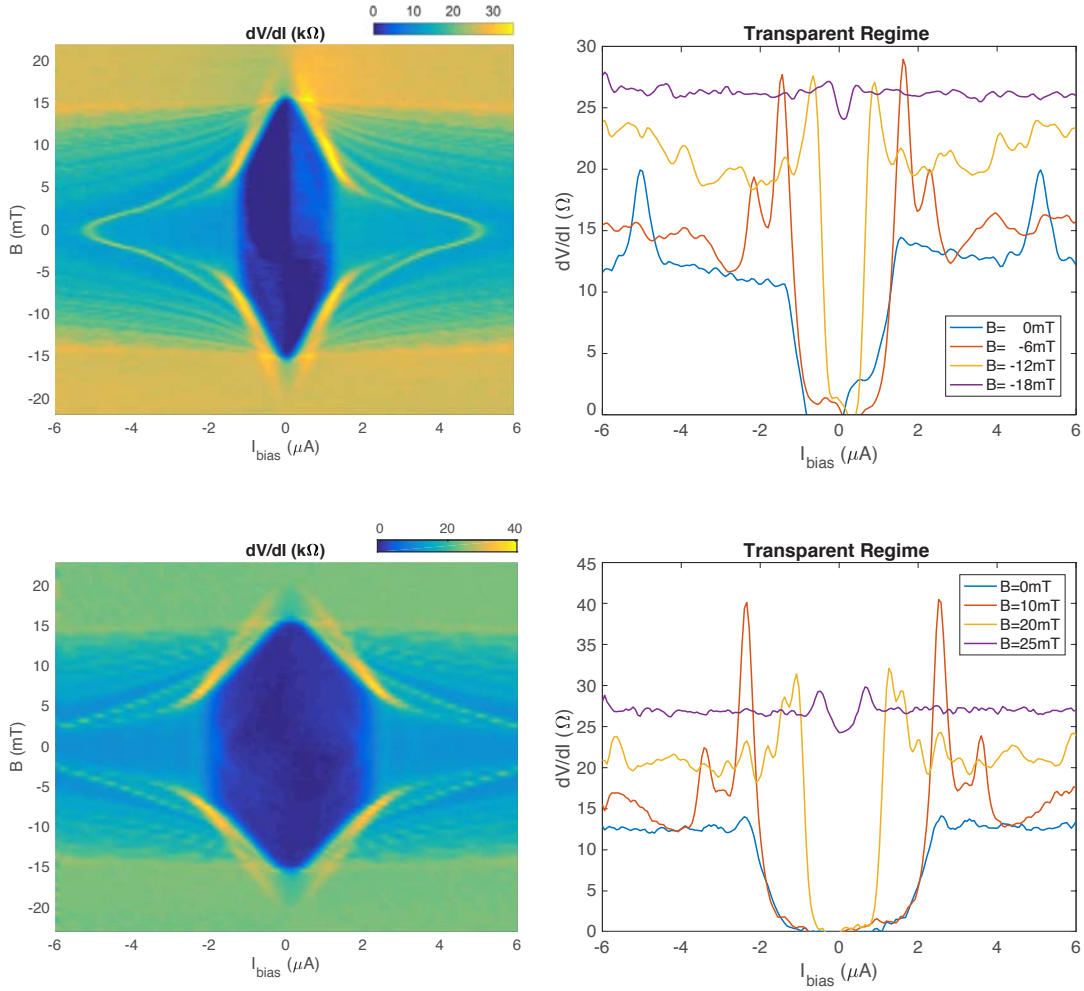

Figure 3.4: Magnetic field dependence of the differential resistance in the transparent regime. The device has direct Al contact on graphene. Top: at $V_{bg} = 0V$. Bottom: at $V_{bg} = 50V$. The color plots are dV/dI as a function of current bias and magnetic field. Linecuts: dV/dI as a function of bias at different magnetic field.

Another explanation comes from McMillan-Rowell resonance (MRR),[18,19,20] which describes quasi-particle interference as well but inside the normal region (i.e., the proximitized region and in our case, graphene). Note that in a normal material an electron and a hole cannot interfere directly.[19] So after the first Andreev reflection, the incident electron is reflected as a hole and has to propagate in the nor-

mal region before traveling back to the NS interface and undergo a second Andreev reflection. It will be converted back into an electron and can then interfere with the incident electron. The oscillations occur at bias

$$V_m = V_0 + mhV_F^N/4d_N \quad \text{with } m = 0, 1, 2... \tag{3.2}$$

where V_F^N is the Fermi velocity in the normal region and d_N is its thickness. One can see that in order to have MRR, the phase coherence between the incident electron and the Andreev reflected hole has to be preserved while the latter is traveling back and forth in the normal region.[18,19] Therefore, the observation of MRR implies that the superconducting correlation remains in the graphene and is a manifestation of graphene being proximitized.

3.3 Tunneling Regime: Al/BN/graphene

The most common van der Waals material that is used as a barrier layer is hexagonal boron nitride (hBN). It shares the same crystal structure and has a similar lattice constant as graphene. However, it is a true insulator with a large energy band gap of around 6.1 eV.[21,22] It is commonly used as a dielectric substrate that provides a flat surface for graphene and can also screen the stray electric fields from the impurities existing on the silicon dioxide substrate. As a tunneling layer, hBN has been investigated extensively. There are numerous studies on the transmission probability between combinations of

Device	Tunneling area (μm^2)	$R_N(k\Omega)$	$RA\,(k\Omega \cdot \mu m^2)$
A	1.6	4.2	6.7
B	2.7	2.6	7.2
C	0.75	11.4	8.5
D	1.9	8.9	16.9

Table 3.1: Devices in the tunneling regime with different sizes of tunneling area. The RA product is consistent with the exponential dependence of zero-bias resistance on the thickness of BN separating graphite and gold. [24]

graphene/graphite/gold through different hBN layers. [23,24] However, shockingly, there are no reports on the tunneling of Cooper pairs between graphene and superconductor via ultra-thin hBN. In this section, we present the experimental results in such a system and explain them from the perspective of Andreev process.

The hBN we use is monolayer and there are four devices with different sizes of tunneling area listed in table 3.1. The typical tunneling resistance is on the order of kOhm. The resistance area product (RA) in our devices is consistent with those in graphite/monolayer hBN/gold devices. [24]

The top panel of figure 3.5 shows the magnetic field dependence of the tunneling differential conductance as a function of voltage bias. When $B = 0$, the dI/dV profile shows the conductance at zero bias that is 30% lower than the normal conductance measured at high bias. As the magnetic field is increased, the variation of conductance with bias gradually decreases and eventually flattens out. The fact that the conductance does not go to zero within the gap even at $B = 0$ implies the monolayer hBN is not a completely opaque tunneling barrier for the NS junction. However, Andreev reflection is still not the dominant process and there is extremely limited superconducting correlation inside of

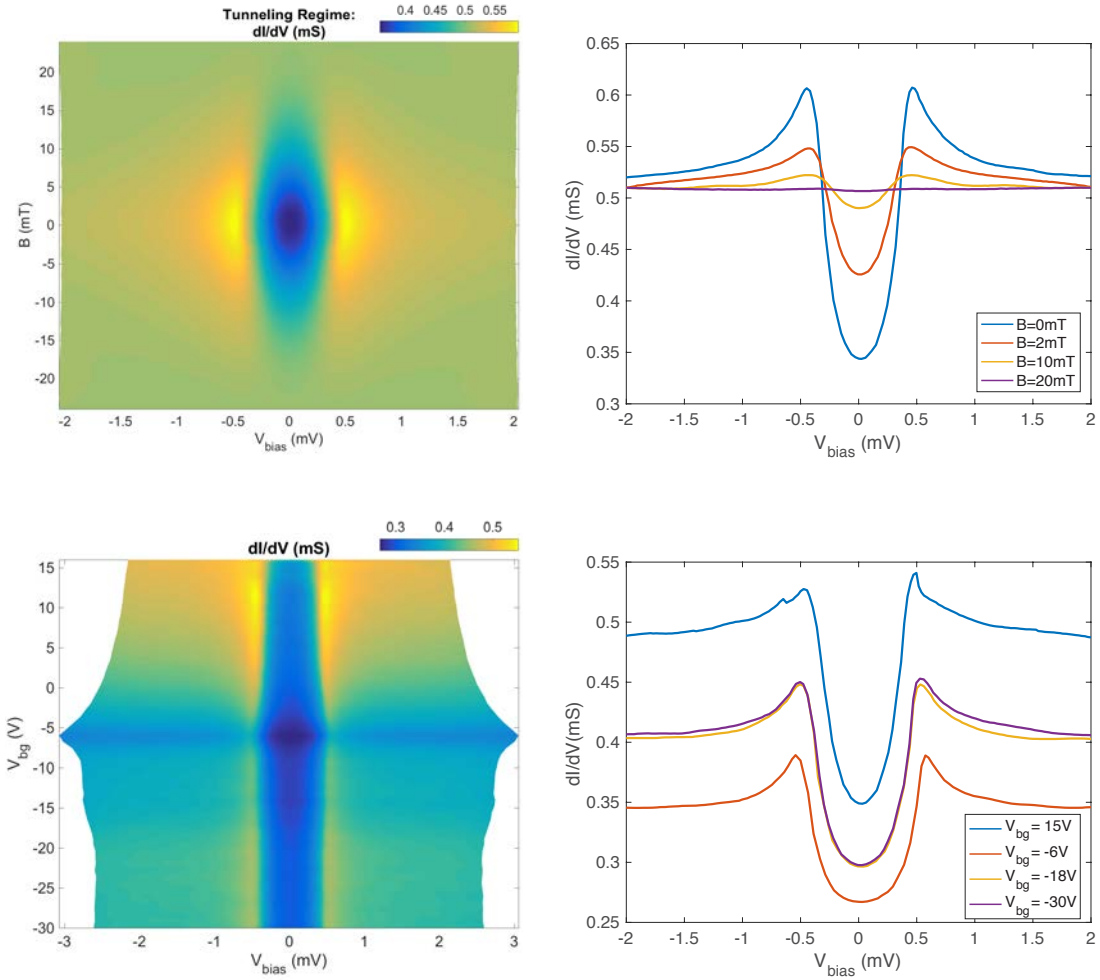

Figure 3.5: Tunneling conductance dI/dV of the device with monolayer hBN in the tunnel regime. Top panel: as a function of voltage bias and magnetic field at $V_{bg} = 30$ V. Bottom panel: as a function of voltage bias and backgate voltage at $B = 0$.

the graphene region. This is reflected in the gate dependence measurement in the bottom panel of figure 3.5. One finds that the measured superconducting gap belongs to Al and thus cannot be tuned by the backgate voltage. Moreover, there are no above gap features such as the Tomasch oscillations or McMillan-Rowell resonances that are observed in the transparent regime.

3.4 Intermediate Regime: Al/MoS_2/Graphene

From the previous two experiments, we learned that in the transparent regime, even though the graphene is proximitized, we cannot probe its properties due to the near zero resistance inside the superconducting gap. On the contrary, with monolayer hBN as the tunnel layer, the Andreev process is not prominent enough to produce superconducting correlation in the graphene layer. As a consequence, graphene only plays the role of probing the superconducting Al. Since the above two regimes cannot meet our goal of investigating the proximity effect features in graphene, we need to come up with another type of barrier that falls in between nothing and hBN.

Molybdenum disulfide (MoS_2) belongs to the class of transition metal dichalcogenides (TMDCs). The crystal structure of MoS2 takes the form of a hexagonal plane of S atoms on either side of a hexagonal plane of Mo atoms. While there are strong covalent bonds between the Mo and S atoms, the van der Waals force holding the layers together is weak. Therefore, similar to graphene and hBN, MoS_2 can be mechanically exfoliated, even down to a single layer (figure 3.6). Monolayer MoS_2 has a direct band gap around 2.1-2.5 eV, [25,26] which is much smaller than the wide band gap of monolayer hBN. Be-

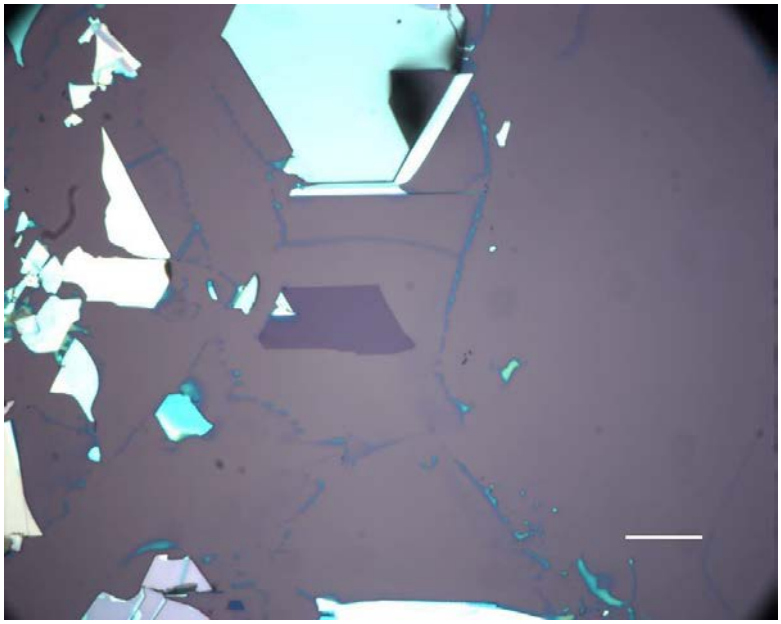

Figure 3.6: Optical image of monolayer MoS_2. Scale bar is 2 μm.

cause the transmission probability is dependent on the size of the bandgap, MoS2 serves as the perfect middle-ground between our previous two experiments. Using MoS2, graphene has the best chance of being proximitized while demonstrating some tunnel resistance at the barrier interface, which is required for electronic probing.

3.4.1 Differential conductance enhancement

Using the same measurement configuration as in the previous two sections, figure 3.7 shows the tunneling differential conductance of the vertical structure Al/MoS_2/graphene from two devices. Although both devices use monolayer MoS_2 as the barrier layer and are fabricated with the same procedure, the differential conductance shows different profiles. Near zero bias, the first type has a conductance dip

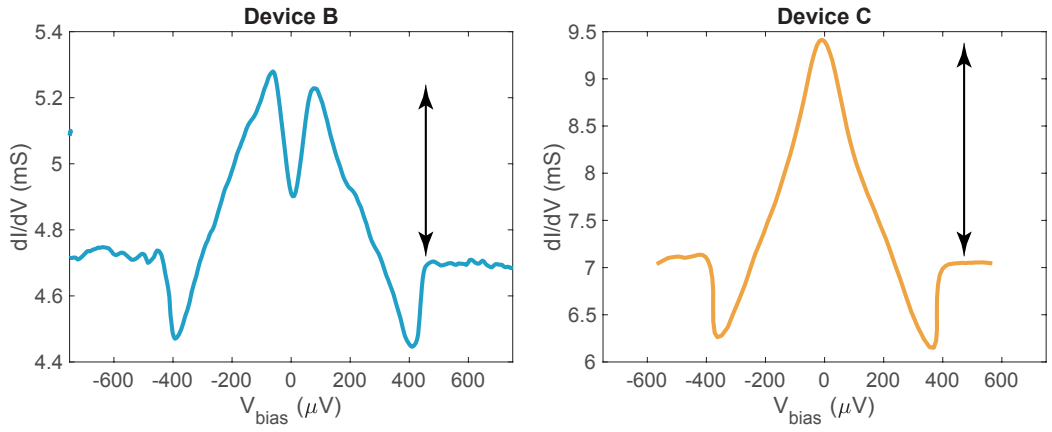

Figure 3.7: Differential conductance in the intermediate regime from two devices. The two devices show distinct behavior around zero bias: Device B has a conductance suppression but Device C does not. However, the general feature is consistent. At high bias, the normal contact resistance is 100-300 Ω. Inside the induced superconducting gap, there is conductance enhancement (the black arrows).

while the second type does not. Since there is no polymer in between the van der Waals materials, we suspect the zero-bias dip originates from a finite barrier between MoS_2 and Al that cannot be overcome at extremely low bias. It may come from the PMMA residue after the ebeam lithography for defining the Al contacts. Yet the overall quality is consistent. At high bias, the normal contact resistance is around 100-300 Ω. Once inside the proximity induced superconducting gap, there is a significant enhancement compared to the conductance at high bias, indicating prevalent Andreev reflection process between Al and graphene through MoS_2.The percentage of conductance enhancement is device dependent; typically around 10-50 %.

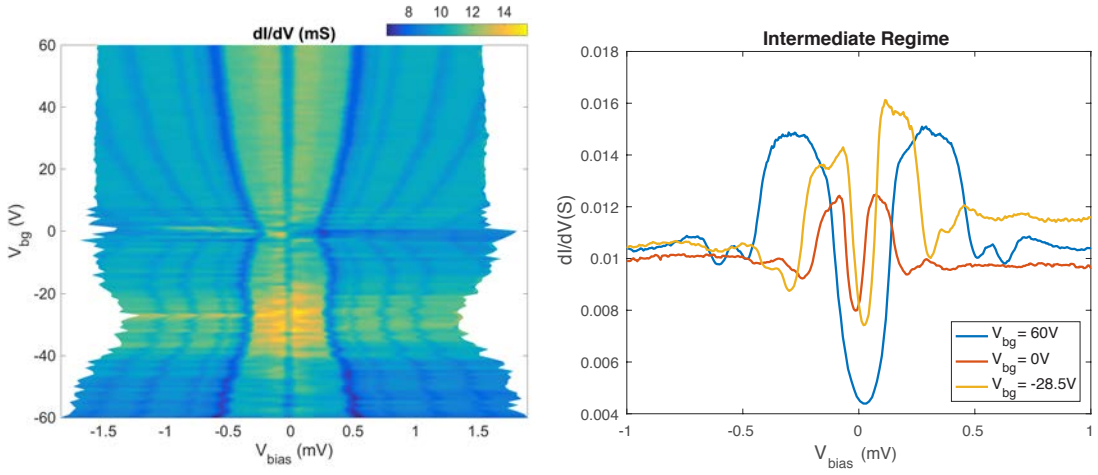

Figure 3.8: Gate dependence of the tunneling resistance in the intermediate regime. Same as in the transparent regime, the proximitized superconducting gap can be tuned by backgate voltage, where the minimum appears at the graphene Dirac peak ($V_{bg} = 0V$).

3.4.2 Gate dependence

Figure 3.8 shows the gate dependence of the tunneling differential conductance as a function of voltage bias at zero magnetic field. Same as in the transparent regime, by tuning the gate voltage we can control the size of the induced gap. Also, outside of the induced superconducting gap there are oscillations similar to the ones seen in the proximitized graphene in the transparent regime. This implies that there is in fact superconducting correlation in graphene despite the presence of a barrier layer. These features along with the conductance enhancement indicate that we obtain a graphene layer proximitized by Al through the monolayer MoS_2.

3.5 Magnetoresistance Plateaus in the Intermediate Regime

Now that we have shown signs of proximity effect in the graphene, we can go on to explore how the Andreev process can be modulated and the consequences in the proximized graphene.

In both figure 3.9 and 3.10, the top panel shows the differential conductance as a function of bias current and magnetic field while the bottom panel shows horizontal linecuts at different values of B. The difference is that figure 3.9 is data from the first type of device: having conductance suppression near zero bias and figure 3.10 is data from the second type of device: complete enhancement inside the gap. From the linecuts it is clear that as B is increased, the variation in conductance gradually flattens out and the induced gap decreases. Eventually when B is greater than the critical field, the conductance recovers to the normal state value and the gap disappears as expected. However, we find that there is one feature absent in the tunnel and transparent regimes that appears only in the intermediate regime: the magnetoresistance plateaus. When the bias voltage is greater than the gap, the curves at different values of magnetic field do not overlap with each other. Once the bias becomes smaller than the gap, the curves converge and collapsed to only a few values. This feature is obvious in the color plot: for field below H_c and bias inside the gap, there are several horizontal discrete "bands" along constant magnetic field lines.

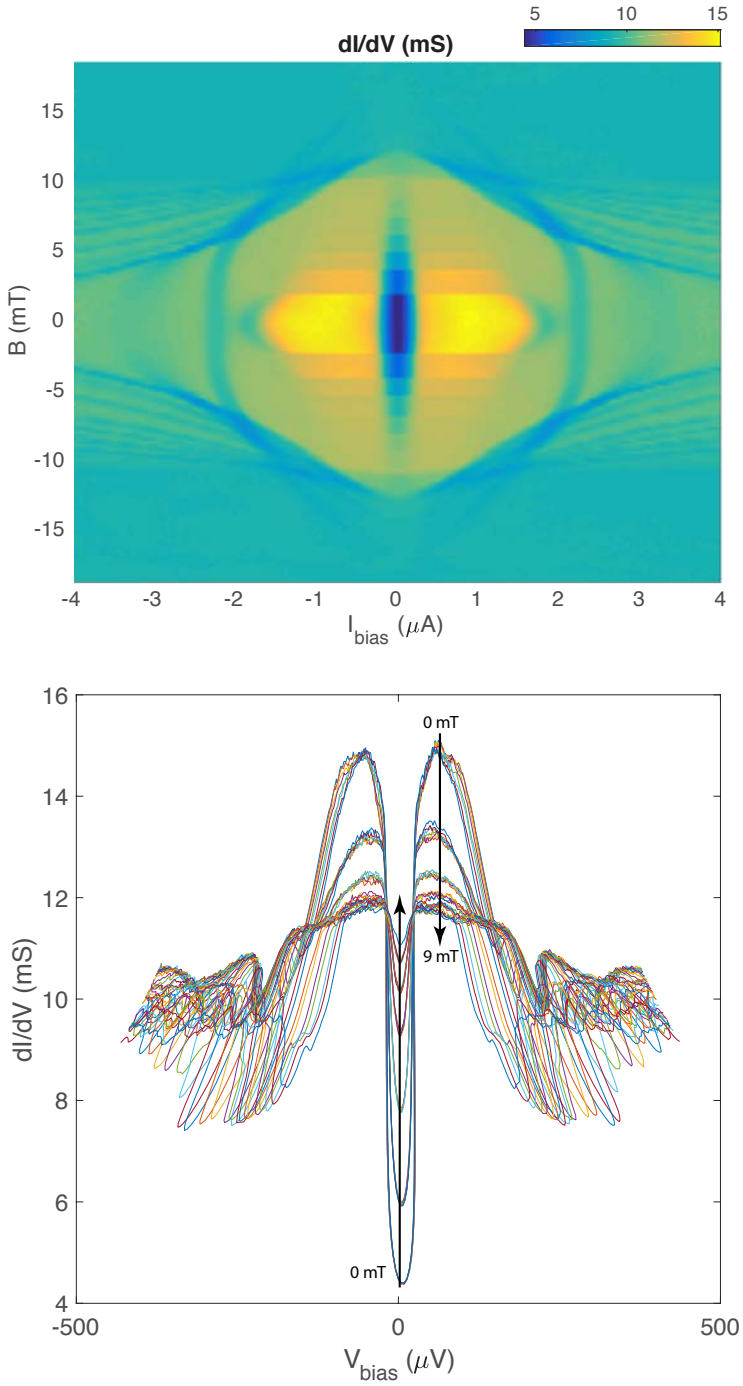

Figure 3.9: (Device A) Tunneling differential conductance dI/dV as a function of bias and magnetic field at $V_{bg} = 60$ V. Top: color plot with current bias as the x-axis. Bottom: horizontal linecuts of the color plot with the current bias converted into voltage bias; dI/dV as a function of voltage bias at different values of B.

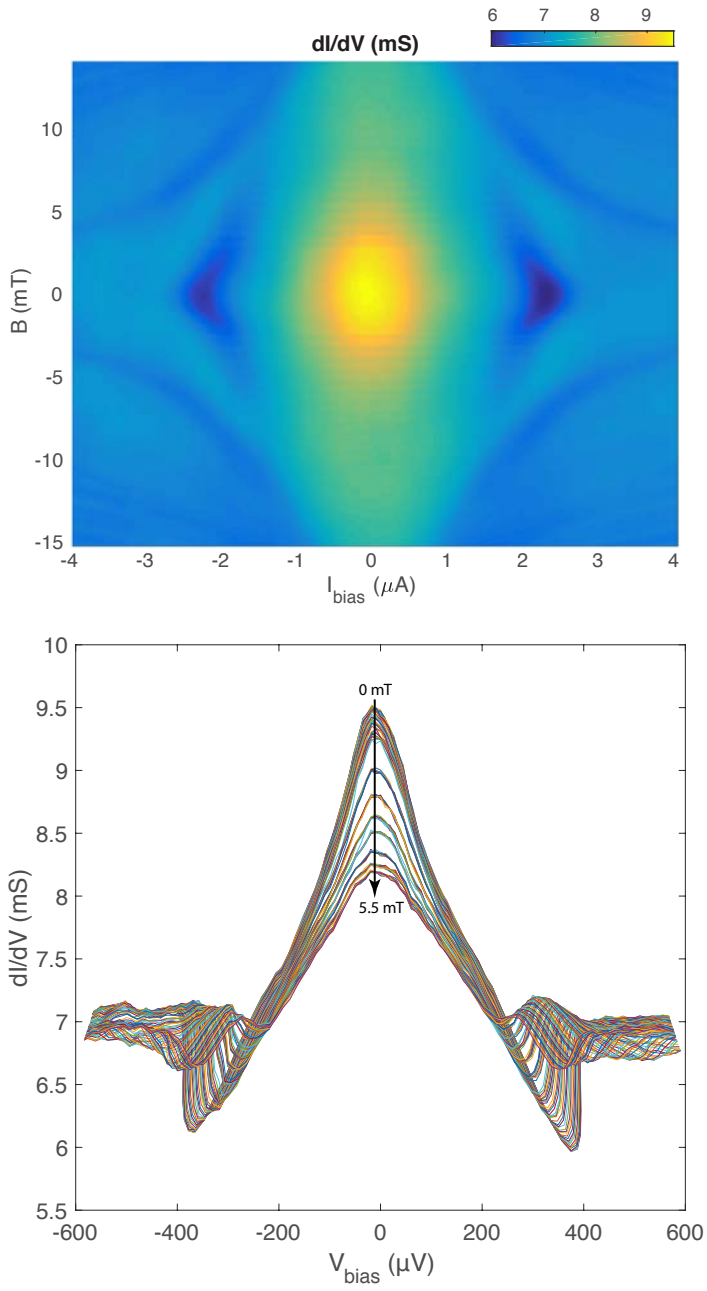

Figure 3.10: (Device C) Tunneling differential conductance dI/dV as a function of bias and magnetic field at $V_{bg} = 60$V. Top: color plot with current bias as the x-axis. Bottom: horizontal linecuts of the color plot with the current bias converted into voltage bias; dI/dV as a function of voltage bias at different values of B.

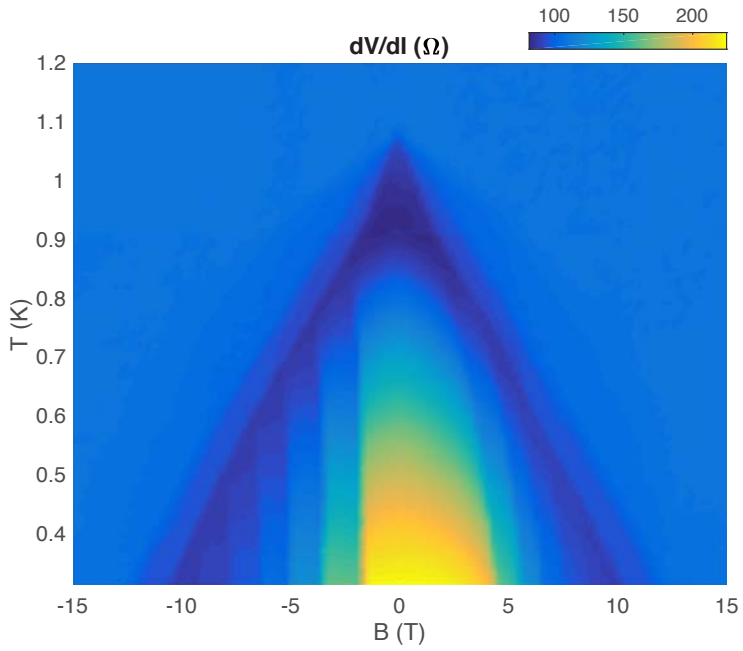

Figure 3.11: Temperature dependence of the magnetic plateaus, which only exist in the superconducting states. The width of the plateaus is not affected by the size of the superconducting gap.

The temperature dependence at zero bias is shown in figure 3.11: the differential resistance as a function of magnetic field and temperature. It turns out these magnetoresistance plateaus are only developed below the critical temperature and critical field, suggesting that they are tied with the superconductivity. As the temperature or magnetic field is increased, overall the width of the steps remains fixed until they disappear; the width is not affected by the size of the superconducting gap. We also noticed there is hysteresis; as shown in figure 3.12, the blue curve is the data taken when the magnetic field sweeps from negative to positive and the red curve is for the opposite sweeping direction.

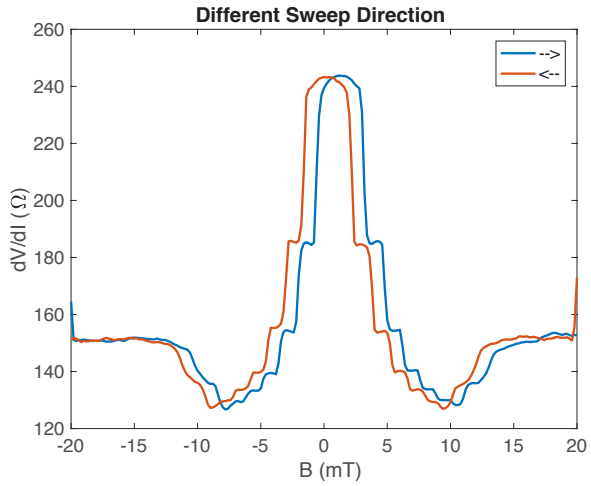

Figure 3.12: Sweeping magnetic field up (blue) and down (red) shows the hysteresis.

3.5.1 Collection of devices

In order to investigate these magnetoresistance plateaus, we fabricated devices in the intermediate regime with different sizes of the tunneling area, which is also proportional to the size of proximitized graphene. In table 3.2, we collect the information from devices A-D, including an optical image, normalized resistance as a function of bias and field, tunneling area, and step width. Among the four devices, A and B are the first type with a conductance dip (resistance peak) around zero bias; C and D are the second type without any suppression inside the gap. Figure 3.13 shows that both the width and height of the plateaus are device-dependent.

Device		Bias-Field 2D Plot	Al/Gr Area	Step Width
A		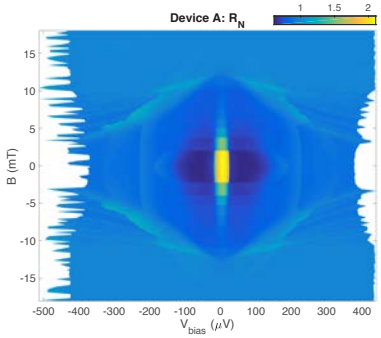	2.25 μm^2	1.35 $\pm$ 0.223 mT
B	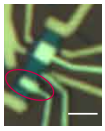	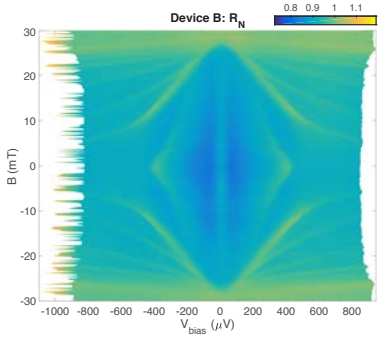	1.08 μm^2	2.50 $\pm$ 0.234 mT
C	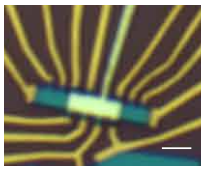	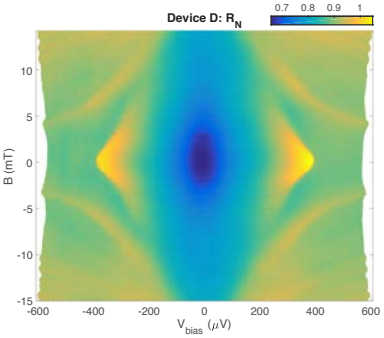	4.32 μm^2	0.67 $\pm$ 0.058 mT
D	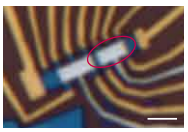	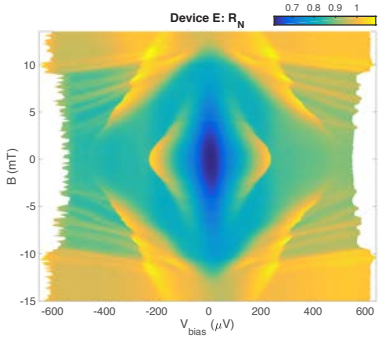	2.37 μm^2	1.26 $\pm$ 0.082 mT

Table 3.2: Intermediate regime devices: optical image, normalized differential resistance as a function of voltage bias and magnetic field, tunneling area, and step width. The scale bar in the optical images is 2 μm.

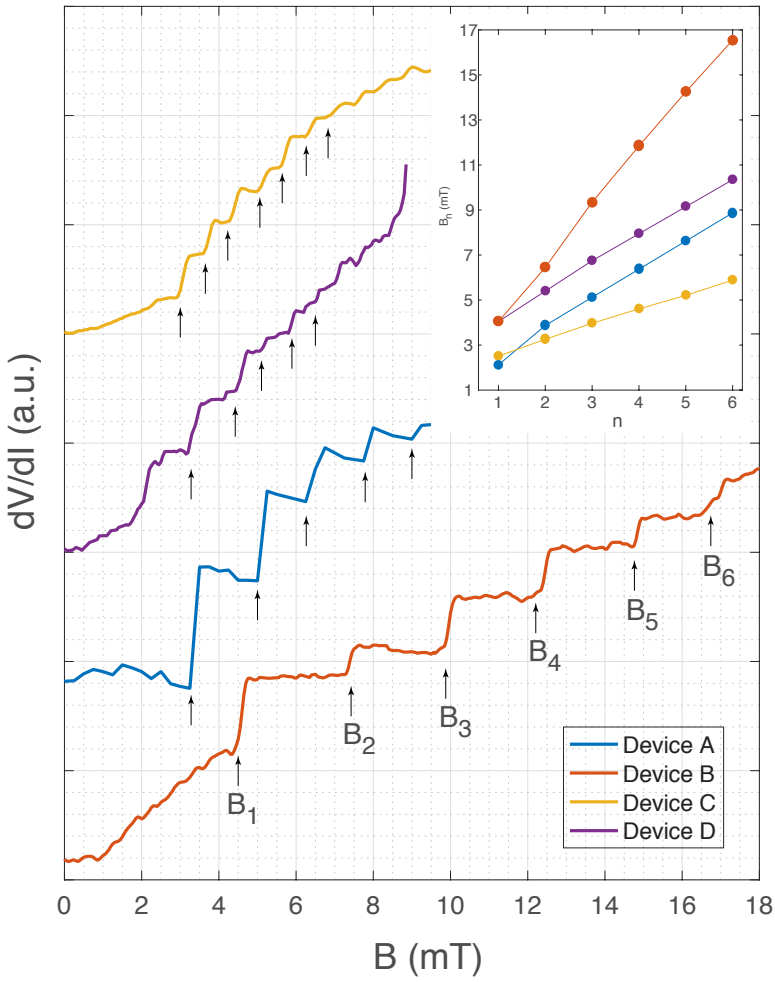

Figure 3.13: Step feature among different devices. Inset shows B_n for each device; the slope provides average step size.

3.5.2 Step width and tunneling area

From the comparison between these devices, we find that the average width of the plateaus is determined by the overlapping area between graphene and Al. Note that usually the central step around

zero is wider than the the rest of the steps, so it is excluded from the averaging. If we consider the superconducting flux quantum $\Phi_0 = h/2e$, each step corresponds to adding/removing one flux into the system.

3.5.3 Gate dependence of the magnetoresistance plateaus

Figure 3.14 shows the gate dependence of the plateaus from Device C. As shown in the top panel, the graphene has Dirac peak at $V_{bg} = -50$ V. In the bottom panel, the plateaus at different values of backgate are compared. For clarity, the curves are shifted in the y-axis direction. At Dirac peak (green), there is no obvious plateau developed since dV/dI as a function of B is rather noisy. As we move away from the Dirac peak, the step feature becomes visible. Moreover, the steepness of the steps is also gate-dependent. In figure 3.15, the relation between the height of each step and magnetic field is analyzed. By plotting the resistance dV/dI at every step as a function of the inverse of magnetic field $(1/B)$, we find that the data can be well fitted with a linear equation. The magnitude of the slope gradually decreases as the graphene is tuned to higher carrier density. The slope reveals how the tunneling resistance, hence the Andreev process, is modulated when a flux enters the hybrid graphene/Al system.

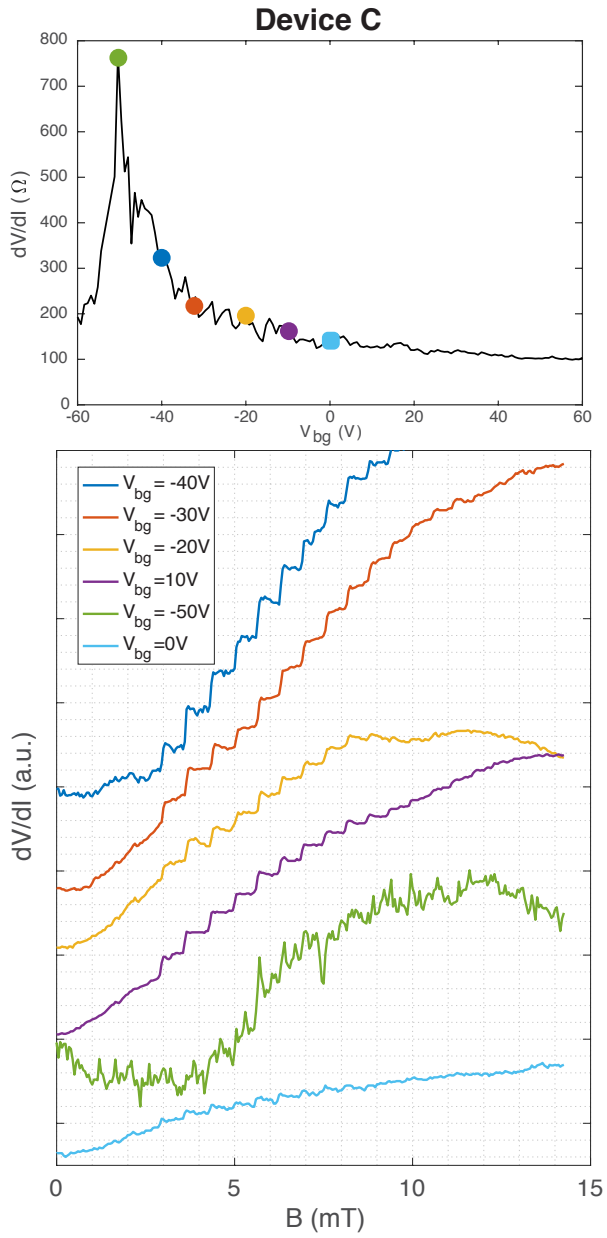

Figure 3.14: (Device C) Gate dependence of the magnetoresistance plateaus. Top panel: Graphene resistance as a function of backgate at zero magnetic field. Dirac peak of the graphene is at $V_{bg} = -50$ V. Dots with different colors correspond to the gate voltage where magnetic resistances are measured in the bottom panel. Bottom panel: plateaus at different values of backgate. There is no clear step feature when graphene is at the charge neutrality point.

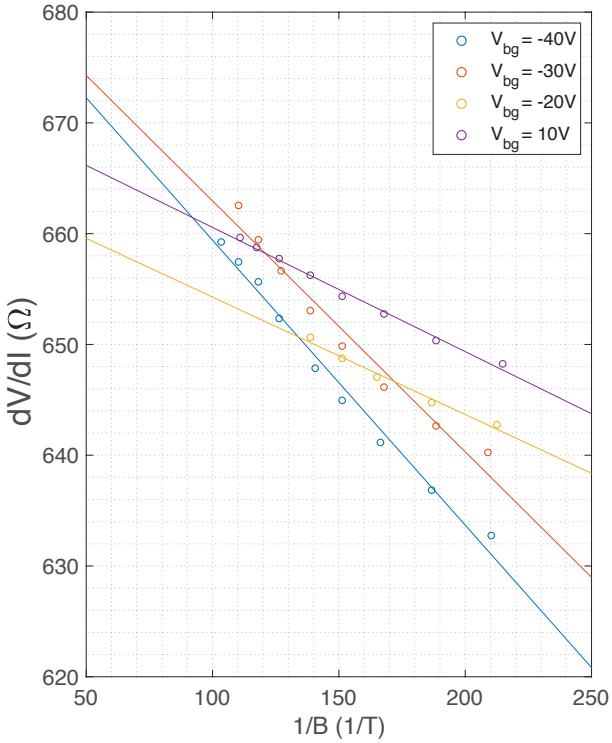

Figure 3.15: (Device C) Scattered data points correspond to the value of each step plotted as a function of $1/B$, which shows a linear behavior. The slope is is gate-dependent.

3.5.4 From plateaus to oscillations

From the data of Device C, it is difficult to extract the plateau information at Dirac peak due to the low signal/noise ratio. However, as we evaluate the other devices, we notice a peculiarity in terms of gate dependence. Figure 3.16 shows the differential conductance dI/dV as a function of current bias and magnetic field from Device B. Top panel is taken at $V_{bg} = 1.8$ V (Dirac peak) while bottom panel is taken at a high gate $V_{bg} = 60$ V. From the two color plots, the immediate difference we see is that only the conductance away from Dirac peak has clear plateaus, which is similar to the observation in Device C. Now let us take a better look by plotting the linecuts at zero bias for both $V_{bg} = 1.8$ V and $V_{bg} = 60$ V. This is shown in the left panel of figure 3.17, in which the orange curve is at Dirac peak and the blue curve is far from Dirac peak. The inset is after shifting the two curves in y-direction so that they are in the same resistance range for clear comparison. The contrast pops out right on the spot: while at high gate the steps are well developed, there is an oscillatory behavior at Dirac peak. This feature is also found in Device D, as shown in the right panel of figure 3.17.

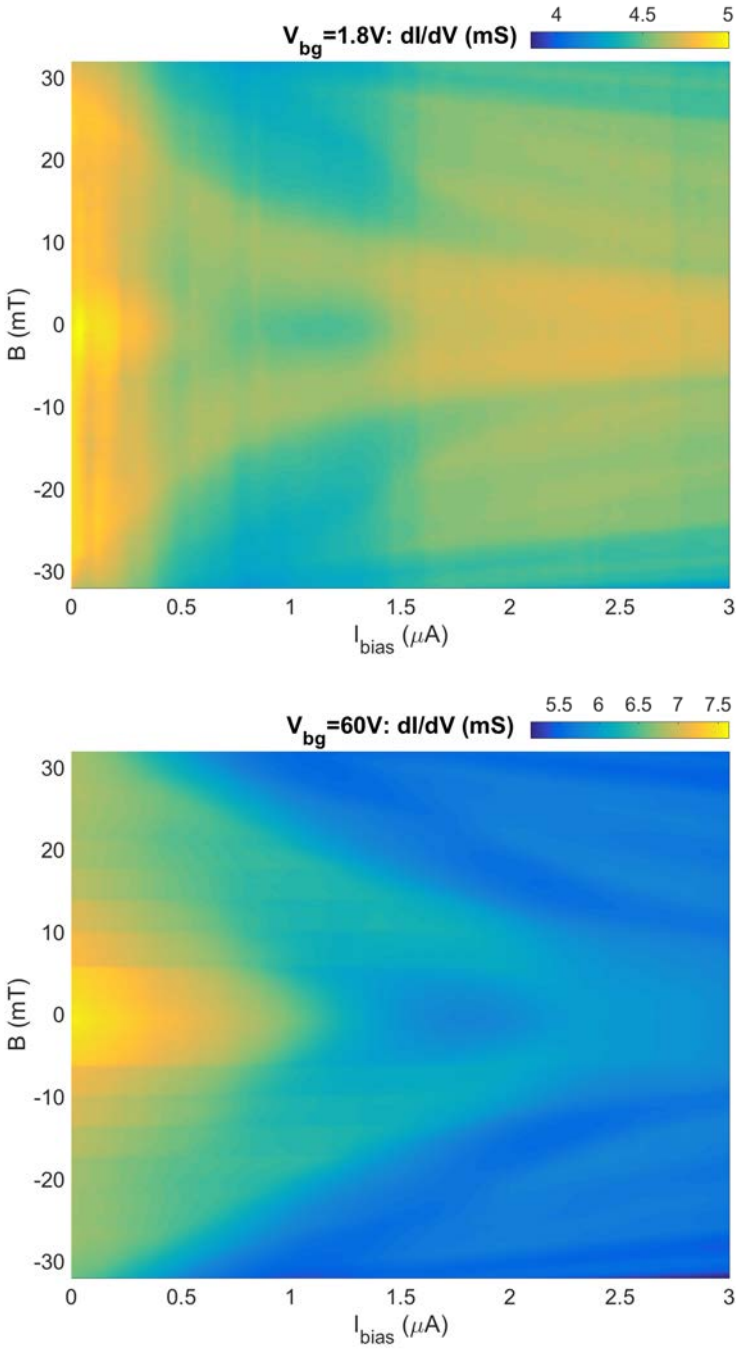

Figure 3.16: Device B: Differential conductance as a function of current bias and magnetic field at Dirac peak ($V_{bg} = 1.8V$) and far from Dirac peak ($V_{bg} = 60V$).

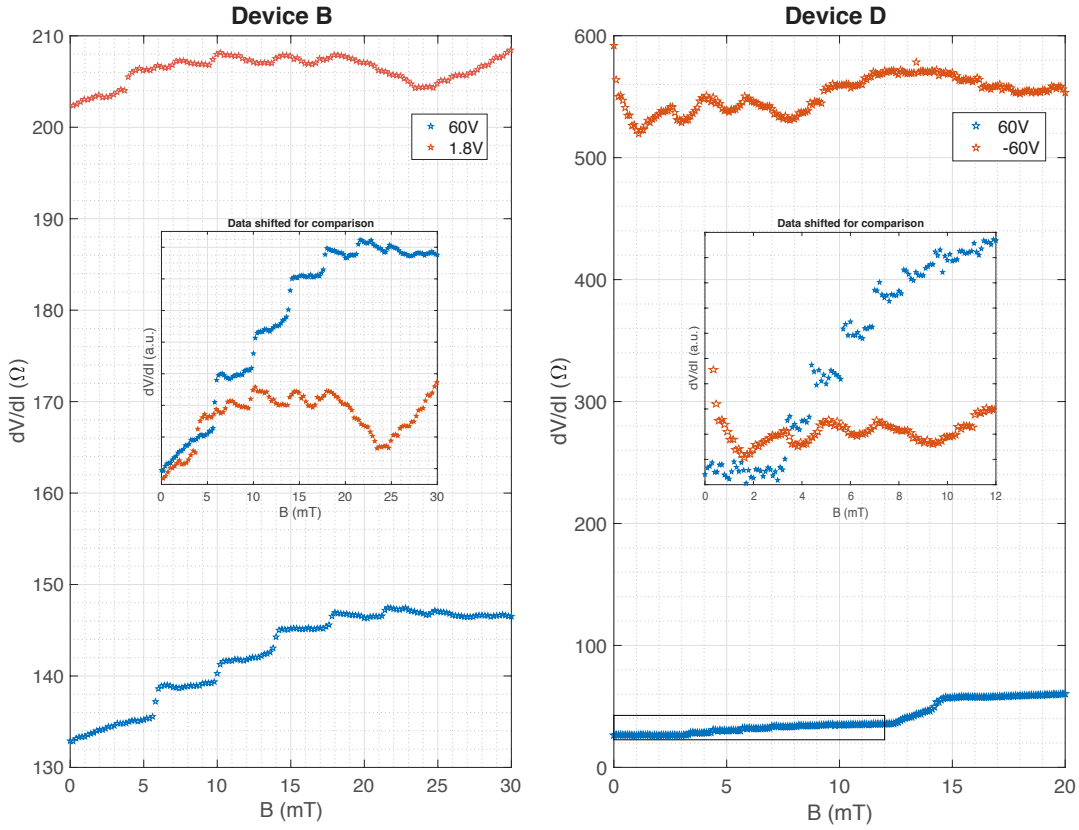

Figure 3.17: Magnetoresistance plateaus at Dirac peak (orange) and at high gate (blue) from device B and D. The inset shows the shifted data in y-direction for clear comparison. In both devices, the plateaus at high gate become oscillations at the charge neutrality point.

Superconducting vortices have been directly observed in proxmitized normal regions.[27] Due to the relation between the step width and graphene/Al overlapping area, we deduce the plateau feature is related to the transport of vortices at the interface as well as in the proximitized graphene. Although Al is type I superconductor, which does not allow formation of quantized magnetic vorticies in the bulk sample, mesoscopic Al islands can exhibit vortex structures in the low magnetic field regime.[28,29]

When the gate is tuned to be far away from the Dirac peak, the density of states in graphene is high and it is more likely for the vortices to be transmitted into graphene. The opposite situation occurs at the charge neutrality point. Despite the fact that the vortices may still enter the graphene layer, their behavior can be very different when density of states is very limited in graphene. While the mechanism behind these oscillations requires more investigation, we have demonstrated that the superconducting features (such as vortices) can be modulated by the tunable properties in graphene.

3.6 Conclusion

The Andreev process probability is determined by the barrier strength separating the normal conductor and the superconductor. In this chapter, we explored the fundamental proximity effect in graphene systematically in different regimes depending on the Andreev probability. Using insulating van der Waals materials as the tunnel barrier allows us to assemble a vertical structure with atomically flat and clean interface between graphene and the tunnel barrier. We can control the barrier strength by choosing materials with different sizes of band gap or different numbers of atomic layers. In the

transparent regime we showed that when the superconducting Al is in direct contact with graphene, the induced gap is gate tunable and there are above gap features showing the superconducting correlation inside the graphene. However, the near zero resistance inside the gap prevents us from further probing the properties of proximatized graphene. Conversely, by using monolayer hBN as the barrier we enter the tunnel regime. The graphene is no longer proximitzied and we can only observe the superconducting gap of Al without gate dependence and any above gap features. An ideal regime for the purpose of our study is achieved by selecting monolayer MoS_2 as the separation layer between graphene and Al. In this intermediate regime, we find that inside the induced gap there is typically a 10-50 % enhancement of conductance, indicating the predominance of the Andreev process between graphene and Al via MoS_2. Furthermore, in the field dependence measurement there are plateaus developed in the magnetoresistance. Since the width of the plateaus is consistent with a flux quantum in the system, we ascribe their origin to vortices. On top of that, we have discovered that as graphene approaches the Dirac peak, these magnetoresistance plateaus transition into oscillations.

The above experimental results have demonstrated how we can obtain different probabilities of the Andreev process by experimental control of barrier strength. With significant probability of Andreev process there is superconducting correlation in the graphene layer, and its proximity effect properties are determined by the magnetic field as well as the carrier density.

While in this chapter we focus on the examination of NS interface and Andreev reflection, we will move to the SNS structure and delve into the formation of Andreev bound states in the next two chapters. Systems with three or more superconducting leads that have a vast and unique set of properties will be discussed.

4

Beyond Two-Terminal SNS Junctions

As we discussed in Chapter 2, in a simple two terminal Josephson junction, successive local Andreev reflections at the two NS interfaces produce correlated electron-hole pairs and hence the supercurrent-carrying states, Andreev bound states (ABS), are formed in the normal region. There has been a fast growing interest in Josephson junctions with more than two terminals as they lead

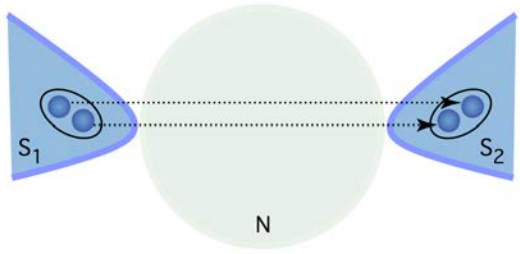

Figure 4.1: Transfer of Cooper pair in a two-terminal Josephson junction.

to ABS in higher dimensions and topology tailoring of the ABS spectrum is envisioned,[30,31,32,33,34,35,36] which we will discuss at the end of Chapter 5.

In this chapter, we start by describing the simplest multi-terminal Josephson junction, one with three terminals, where Andreev bound states create entangled Cooper pairs that carry a nonlocal supercurrent. Measurements in graphene-based devices with multi-terminal Josephson junctions is presented, along with experimental evidence of the engineering of the ABS spectrum.

4.1 ABS in a Three-Terminal Josephson Junction: Quartets

In figure 4.1, an Andreev bound state is formed as one Cooper pair is transferred between the two superconductors through the normal region. Figure 4.2 shows how in a three-terminal Josephson junction two correlated Cooper pairs can be transmitted among the three superconductors and form a bound state. The right and left superconducting leads each provide a Cooper pair that is decomposed and cross-recombined at the center lead. The resulting two entangled Cooper pairs are given the name

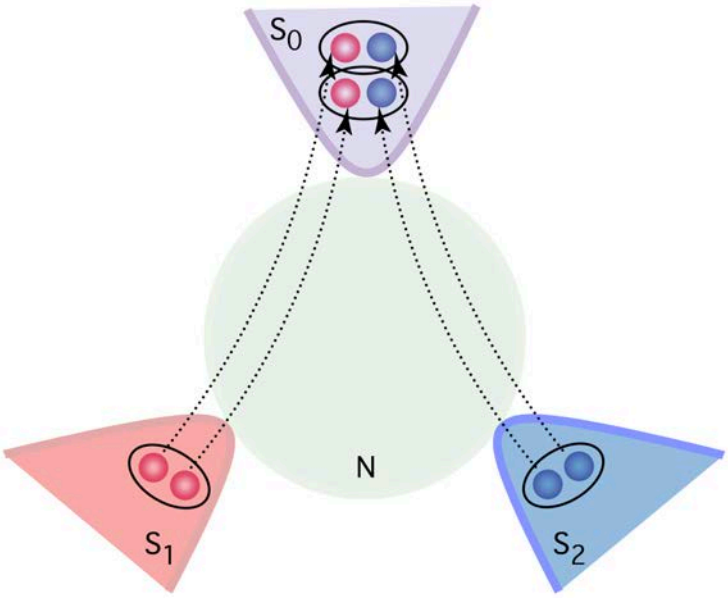

Figure 4.2: Quartet process in a three-terminal Josephson junction.

"quartet" since they consist of four correlated electrons.

4.1.1 A novel out-of-equilibrium coherent mode

The quartet process can take place when there is zero bias voltage on the junction, i.e., when all three leads are grounded and at equilibrium (figure 4.3 top panel). When the junction is biased with different voltages of the three leads, the quartet process can still take place under specific energy conditions, forming a coherent mode in an out of equilibrium system.

The bottom panel of figure 4.3 is an illustration of the biased quartet process. Here, we bias the left (S_1) and right (S_2) superconducting leads with DC voltages V_1 and V_2, respectively, and keep the

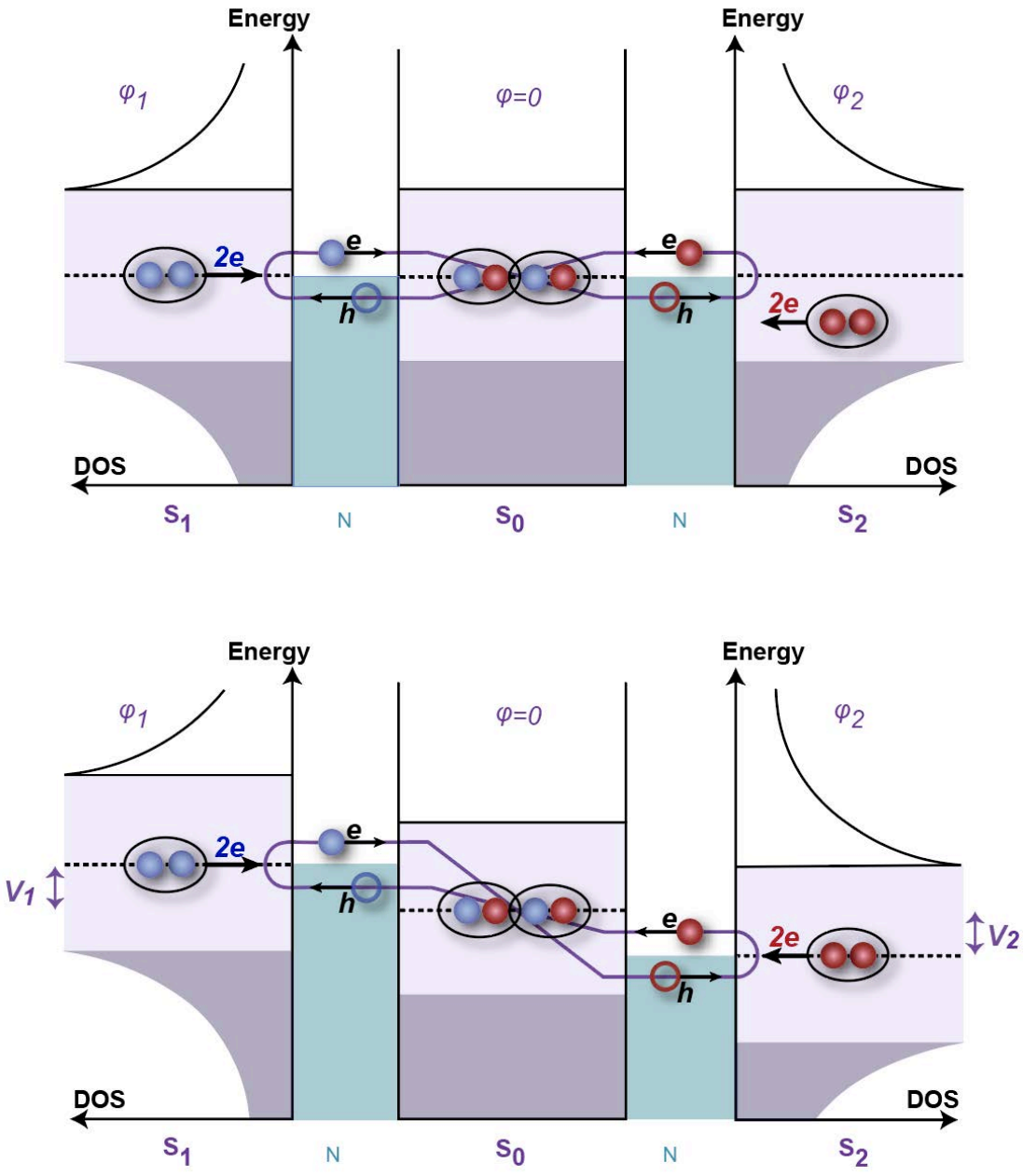

Figure 4.3: The quartet process in the ABS picture consists of two consecutive cross-Andreev-reflections, forming a new type of bound state. Top: At equilibrium. Bottom: Out of equilibrium.

middle lead (S_0) grounded ($V_0 = 0$). From energy considerations, we can extract a criterion for this process: it requires an energy of $2neV_1$ to transfer n Cooper pairs from S_1 to S_0. Similarly, for m pairs to be transferred from S_2 to S_0, it takes an energy of $2meV_2$. In order to satisfy the energy conservation during this process, the following condition must be fulfilled:

$$nV_1 + mV_2 = 0, \quad \text{where } n, m \in \mathbb{N} \tag{4.1}$$

The simplest combination of (n, m) is $(1, 1)$, which involves transferring two Cooper pairs, the "quartet". Likewise, the combination of $(1, 2)$ or $(2, 1)$ has three entangled Cooper pairs transferred and is called "sextet". One can see that there are many possible processes in multi-terminal Josephson junctions, but from now on we will focus on the quartets, for which the bias condition is

$$V_1 = -V_2 = V. \tag{4.2}$$

Note that for two coupled but separate Josephson junctions this condition is also applicable, where two AC Josephson currents coexist with frequencies $\nu_1 = 2eV_1/h$ and $\nu_2 = 2eV_2/h$. When $V_1 = -V_2$, the two frequencies synchronize and produce a subgap DC signal.[37,38] However, this "photon emission/absorption" process can be distinguished from the coherent quartet process by a phase control measurement, which will be discussed later in this chapter.

In summary, the quartet process has two special features. The first is that it is nonlocal, and the second is it forms a resonant state when driven out of equilibrium. The supercurrent in three-terminal

Josephson junctions has already been studied with diffusive metal[39] and one-dimensional nanowire[40]. However, without proper phase control, it is difficult to demonstrate explicitly the quantum coherence of quartets and alternative interpretations cannot be ruled out. We will now discuss the phase space of the quartet Andreev bound states and demonstrate the existence of a resonant state thereby eliminating other explanations for the supercurrent in the $V_1 = -V_2$ bias condition.

4.1.2 Phases of quartets

When a Cooper pair is transferred from one superconducting lead to another, it acquires a phase given by the macroscopic phase difference between the two leads, $\Delta\varphi = \varphi_2 - \varphi_1$. Without magnetic field, this phase difference is a gauge-invariant quantity which determines the physical observable (such as supercurrent). In a three-terminal Josephson junction, there are three phases, one for each superconducting lead: $\varphi_0,\ \varphi_1,\ \varphi_2$. Since only the phase differences are measurable, without loss of generality, we choose $\varphi_0 = 0$ as reference. The two gauge-invariant phases are then φ_1 and φ_2.

To meet the quartet condition, the superconducting leads need to be biased at $V_1 = -V_2 = V$ with $V_0 = 0$. Following the Josephson voltage-phase relation (see *), the phases will evolve in time:

$$\varphi_1(t) = \varphi_1(0) + 2eVt/\hbar \tag{4.3}$$

$$\varphi_2(t) = \varphi_2(0) - 2eVt/\hbar. \tag{4.4}$$

As shown in figure 4.4, the quartet process of transferring the first Cooper pair coherently from S_0

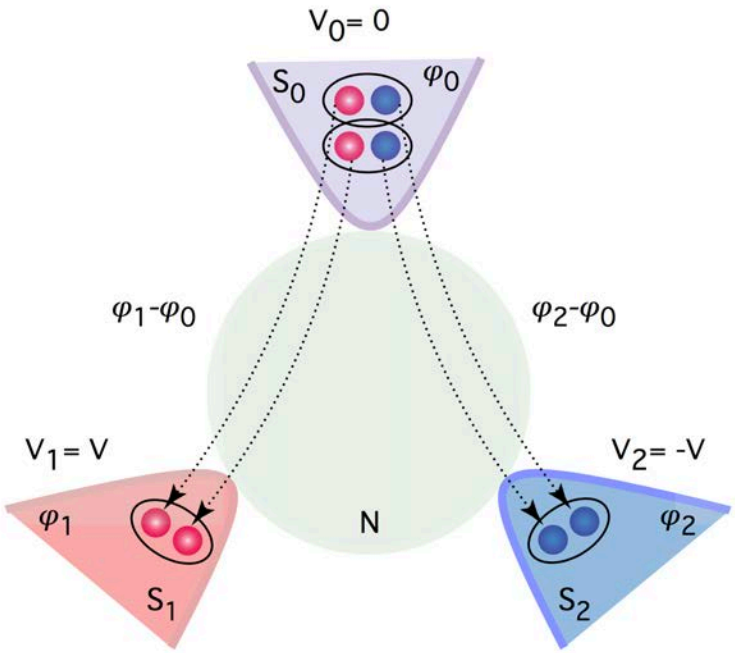

Figure 4.4: Phases in quartet process.

to S_1 and the second pair to S_2 would acquire a total phase $\varphi_1 + \varphi_2 - 2\varphi_0$. We can then define it to be the quartet phase (with $\varphi_0 = 0$):

$$\varphi_q \equiv \varphi_1(t) + \varphi_2(t) = \varphi_1(0) + \varphi_2(0), \tag{4.5}$$

which is time-independent and gauge-invariant. The Josephson-like quartet current, I_q, flows among the three terminals synchronously and can then be determined by φ_q. In our model of a three-terminal Josephson junction, this coherent quartet process satisfies:

$$I_q = I_{qc} \sin \varphi_q, \tag{4.6}$$

where I_{qc} is the maximum value of the quartet current, i.e., the "quartet critical current".

We can choose another canonical phase variable

$$\varphi_r \equiv \varphi_1(t) - \varphi_2(t) = \varphi_1(0) - \varphi_2(0) + 4eVt/\hbar. \tag{4.7}$$

One immediately sees that in contrast to the stationary quartet phase φ_q, φ_r is a running phase that changes in time with a velocity $4eV/\hbar$.

Overall, going from a two-terminal to a three-terminal Josephson junction there exists a quart process that involves a pair of Andreev bound states defined in two-dimensional manifolds spanned by two phase variables. The phase coordinates can be chosen to be the static quartet phase φ_q and the running phase φ_r so that the manifolds change in time only along the latter as shown in the right panel of figure 4.5. Note that φ_r will run at different frequencies when different bias voltages V are applied. Therefore, this V becomes a control voltage, serving as a key knob in tuning how the system evolves in time.

4.2 Quartets in Graphene

Recently, experiments have begun to employ multi-terminal Josephson junctions fabricated on two-dimensional semiconductors including graphene [41] and other two-dimensional electron gases (2DEGs) such as InAs. [42,43] However, only the usual two-terminal Josephson supercurrent between different

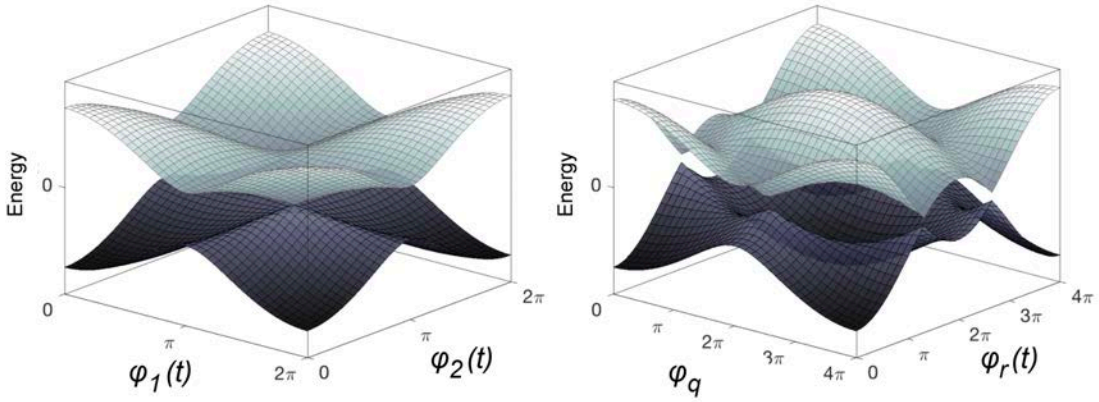

Figure 4.5: Right: two-dimensional ABS energy manifolds of a three-terminal Josephson junction. When $V \neq 0$, the superconducting phases φ_1 and φ_2 are time-dependent. Left: we may choose the canonical phase variables φ_q and φ_r so that the energy remains static along the former and wind in time along the latter.

pairs of contacts has been reported. There is no sign of quartets in these previous studies; a coherent quartet transfer process in a 2D system remains elusive. In this section, we will present the quartet supercurrent observed in our three-terminal graphene Josephson junction.

4.2.1 Device fabrication and geometry

Graphene is known to exhibit low contact resistance and weak scattering when connected to superconducting leads.[44,45,46] Furthermore, we can control the number of conduction channels in the graphene through a gate voltage. These properties of graphene make it a good platform for studying the ABS in Josephson junctions. In order to minimize disorder in the devices, we use hexagonal boron nitride (hBN) as the dielectric substrate. The graphene/hBN heterostructure is assembled with the inverted stacking method (see Appendix A). The advantage of this method is that the surface of

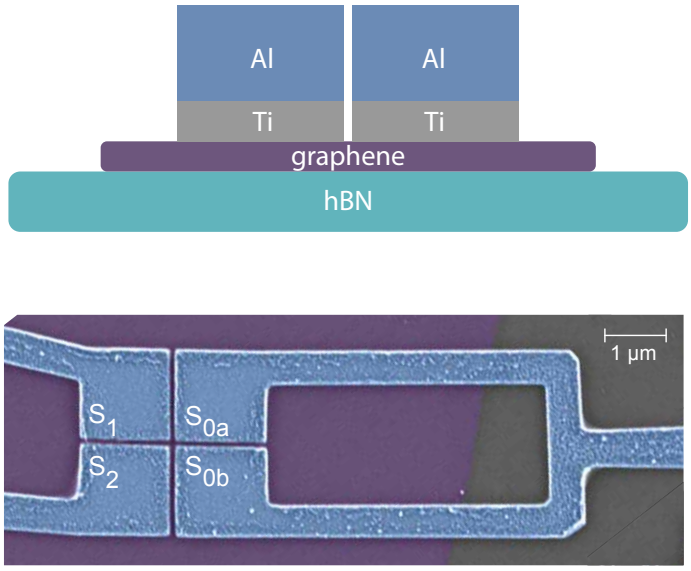

Figure 4.6: Side view of the device structure and false color SEM image of three-terminal graphene Josephson junction with a loop for the quartet experiment. Typically the substrate hBN is chosen to be 20-40 nm thick. The superconducting contacts are made of Ti/ Al (5/60-80 nm). In the SEM image, the purple region is monolayer graphene on hBN and the blue region is Al on Ti.

graphene in contact with the superconductor never comes into contact with polymers (such as PPC or PC) except for PMMA, which is used for e-beam lithography. The final step is to e-beam evaporate 5 nm of Ti followed by 60-80 nm of Al directly on top of the graphene. A side view of the device structure is shown in the top panel of figure 4.6. This fabrication process is found to greatly increase the yield of generating Josephson coupling among all of the superconducting leads, which is essential for creating quartets.

The bottom panel of figure 4.6 shows the SEM image of an actual device viewed from top. In total we have four superconducting contacts where two of them form a loop. Each channel length is designed to be 80-90 nm to ensure a supercurrent existing among all of the superconductors.

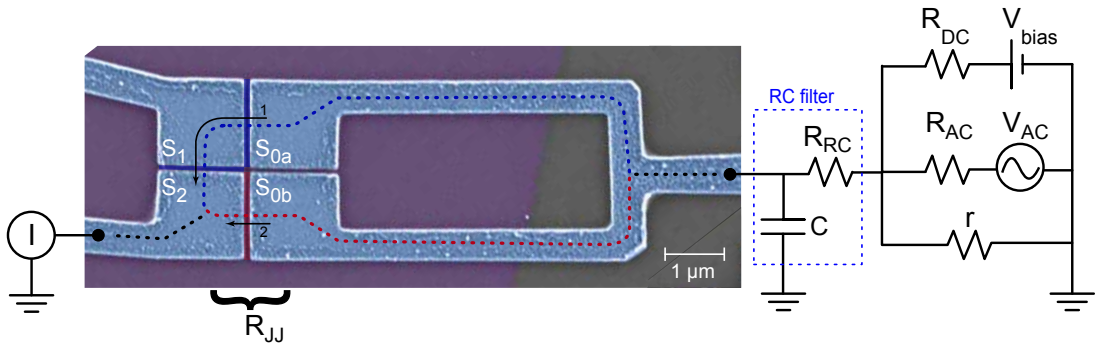

Figure 4.7: Two-terminal measurement setup for device characterization. S_0 (the loop) is voltage biased while S_2 is grounded and S_1 is left floating. The blue and red dashed lines mark the two distinct paths for supercurrents to go from the source to the drain. The interference between them results in a SQUID-like pattern (figure 4.9) as the magnetic field is varied.

Threading a flux through the loop grants us the phase control over the system. This allows us to study the magnetic field dependence of the quartet process. Moreover, the flux can serve as an additional knob for tailoring the ABS spectrum. Thus our four-terminal Josephson junction becomes comparable to a three-terminal Josephson junction whose characteristic can be controlled by applying a magnetic flux in the loop and this will be discussed later.

4.2.2 Two-terminal characterization measurement

We first need to characterize our three-terminal junction by looking at the two-terminal conductance. Using a small AC excitation on top of a DC signal, we bias the loop (S_0) and ground the second lead (S_2). This AC+DC measurement scheme is shown in figure 4.7. The differential conductance dI/dV as a function of the bias voltage and backgate voltage is presented in figure 4.8. The central plateau/peak (the bright orange region in the color plot, traced with the white dotted line) corresponds

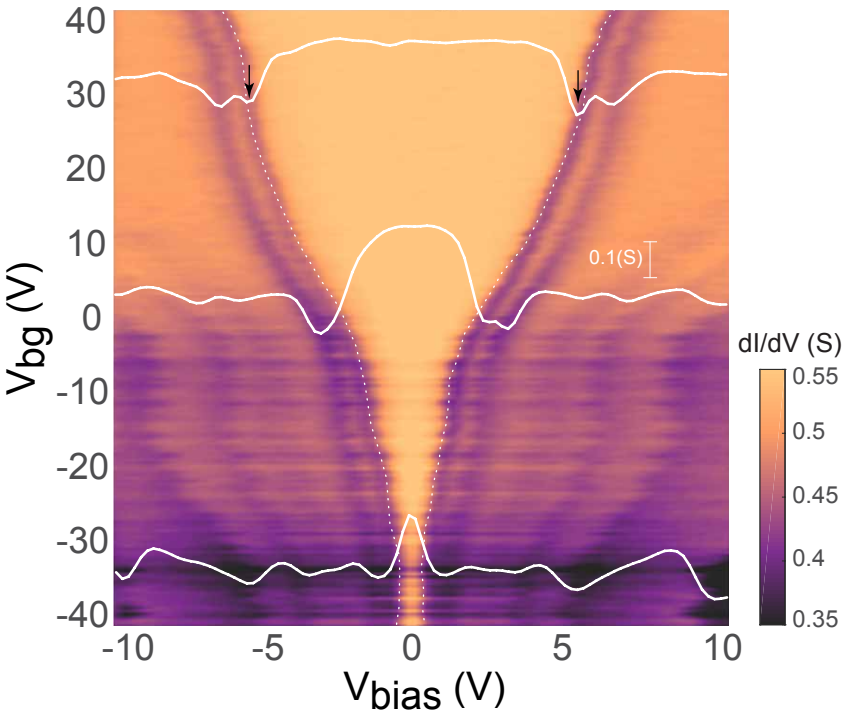

Figure 4.8: Two-terminal measurement for device characterization. The differential conductance dI/dV as a function of the bias voltage V_{bias} and backgate voltage V_{bg}. The critical current is marked by the dashed white line. Despite the screening effect from the aluminum contacts, the carrier density in graphene and hence the critical current is still gate tunable. The black arrows indicated V_c which can be converted into the critical current I_c.

to the supercurrent flowing from S_0 through graphene to S_2. As shown in the white linecuts dI/dV on top of the color plot, the two dips (indicated by the black arrows) around the zero bias peak are $\pm V_c$ that can be converted to the critical current $\pm I_c$ by the relation (Eq.B.13, see the measurement details in Appendix B):

$$I_c = \frac{V_c \cdot 10^{-4}}{(2 \cdot R_{RC} + r)}, \tag{4.8}$$

where the factor 10^{-4} comes from the voltage divider, and R_{RC} and r are the resistors in the circuit that are 200 and 10 Ω, respectively. For instance, at $V_{bg} = 30$ V, the dips are at $V_c = 5$ V and can be translated to a critical current $I_c = 1.2\ \mu$A. The value of the critical current depends on the carrier density in graphene and is tunable with the global backgate. With Ti and Al deposited on top, the graphene is heavily doped with the Dirac peak around $V_{bg} = -30$ V, at which I_c reaches the minimum. For $V_{bias} < V_c$, the junctions are current biased since there is no actual voltage drop across the Josephson junctions. For $V_{bias} > V_c$, the junctions become truly voltage biased.

SQUID-like pattern

In this two-terminal measurement setup, the first lead S_1 is left floating. However, it is still Josephson coupled to S_2 and to S_0, forming an alternative route for the Cooper pairs to enter S_2 from S_0 (the blue dashed line in figure 4.7) besides the direct path (the red dashed line). Therefore, the device can be viewed as two Josephson junctions in parallel, which is equivalent to a DC superconducting quantum interference device (SQUID). Figure 4.9 shows the differential conductance as a function of bias voltage and magnetic field taken at $V_{bg} = 0$. Top panel shows the horizontal linecuts of the color plot. Same as in the previous measurement, V_c corresponds to the critical current and oscillates with the magnetic field. These oscillations in magnetic field have a periodicity $\delta B = 145\,\mu$T, corresponding to one flux quantum Φ_0 threading the loop of an enclosed area $A = 14.2\,\mu\text{m}^2$ (including the area increase due to London penetration depth). The SQUID-like behavior is the simultaneous manifestation of Josephson coupling among the three superconducting leads and is indispensable for

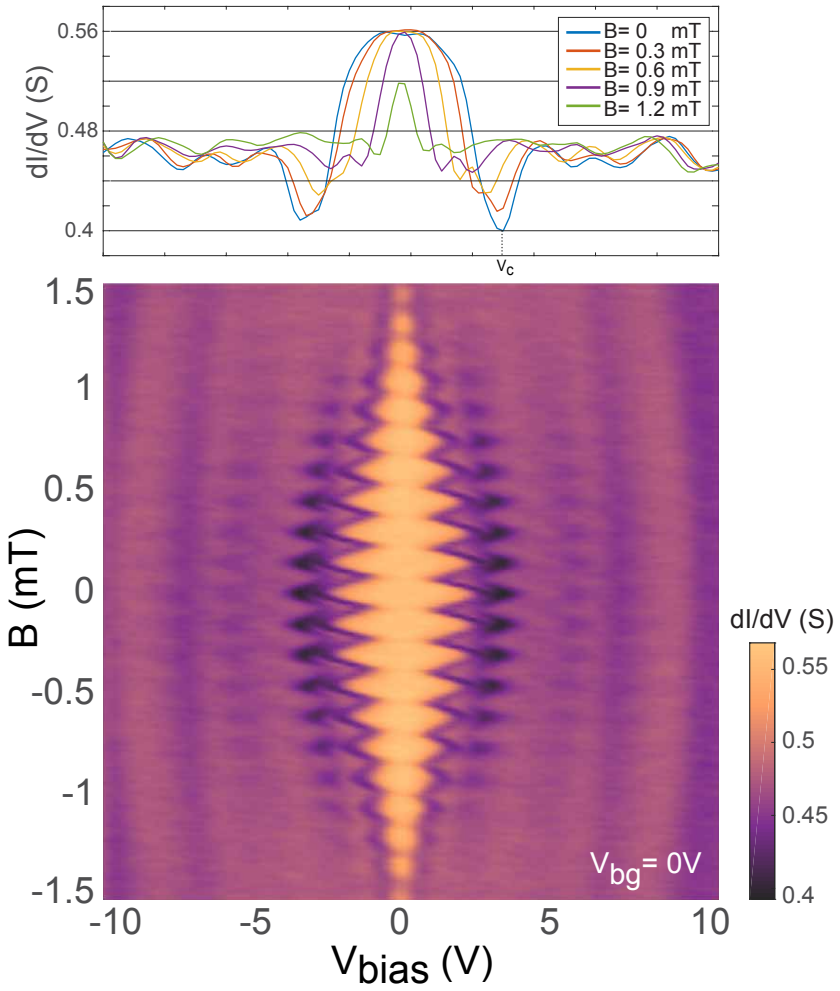

Figure 4.9: Two-terminal measurement for device characterization. The differential conductance dI/dV as a function of the bias voltage V_{bias} and magnetic field when backgate is at zero voltage. The periodicity of the fast oscillations with magnetic field matches threading one flux quantum in the loop. The envelope of these fast oscillations is attributed to the central lobe of the Fraunhofer pattern. The top panel shows the horizontal linecuts, where the dips V_c can be converted into the critical current I_c.

our next step: the observation of quartets.

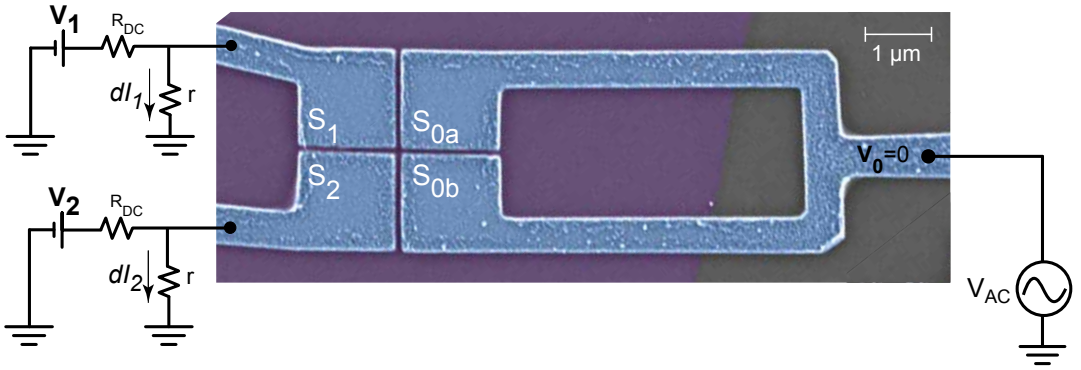

Figure 4.10: The simplified measurement setup for observing quartets. The loop is grounded while the potentials of other two superconducting leads are controlled through the bias voltages V_1 and V_2. A small AC excitation is applied to the loop and the AC currents at S_1, S_2 are measured.

4.2.3 Quartet measurement

The key to creating a quartet bound state lies in controlling the potential of the individual superconducting leads. Figure 4.10 is the simplified circuit for the quartet measurement setup (the complete circuit and measurement details are included in Appendix B.2.4). The loop S_0 is grounded ($V_0 = 0$) as the potential of S_1, S_2 are regulated by the DC bias voltages V_1 and V_2. On top of the DC bias, we apply a small AC excitation V_{AC} to the loop and monitor the AC currents dI_1, dI_2 that flow from S_1, S_2, separately.

Depending on the potential of each superconducting lesd, there are a few different supercurrents that can exist in the device. They are shown in figure 4.11. Subfigures (i) - (iii) show the usual Josephson supercurrent between any two superconducting leads when they are equipotential. Subfigure (iv) shows the quartet supercurrent we are looking for. Figure 4.12 is a map of these different supercur-

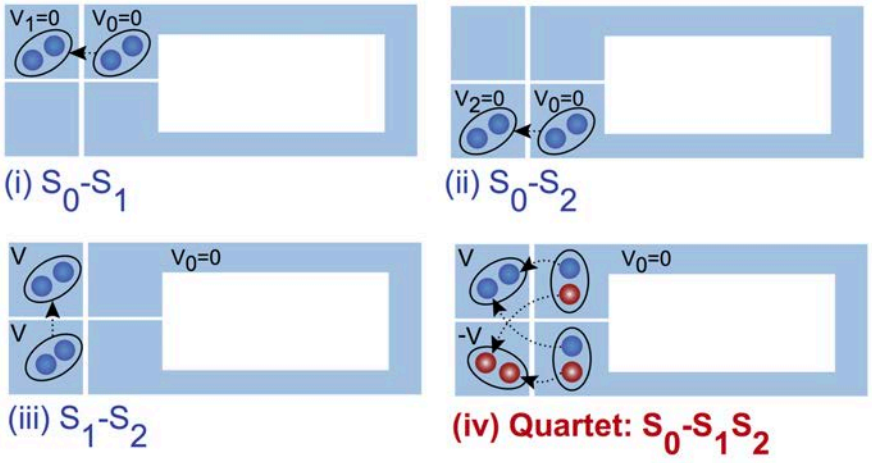

Figure 4.11: In a three-terminal Josephson junction, there are usual Josephson currents between any two leads when they're at the same potential as shown in (i)-(iii). The quartet process takes place under the bias condition $(V_1, V_2) = (V, -V)$.

rents: the differential conductance $G_1 = dI_1/dV_{AC}$ measured at S_1 as a function of the two DC bias voltages V_1 and V_2. As labelled in this color plot: (i) the vertical bright orange region (high conductance) is when V_1 is close to zero, in which case Josephson current between S_1 and S_0 is allowed; (ii) the horizontal orange region originates from the supercurrent flow between S_2 and S_0 when V_2 is close to zero; (iii) Along the +45° diagonal line is $V_1 = V_2$ and we obtain a supercurrent between S_1 and S_2; (iv) Finally, there is a much narrower orange region along the -45° diagonal line, indicated by the red arrow. This is where the quartet bias condition, $V_1 = -V_2$, is satisfied and is where the signal of quartet supercurrent occurs. The actual voltage across the junctions are related to the applied DC voltages V_1, V_2 by Eq.B.4 (See Appendix B.2.4).

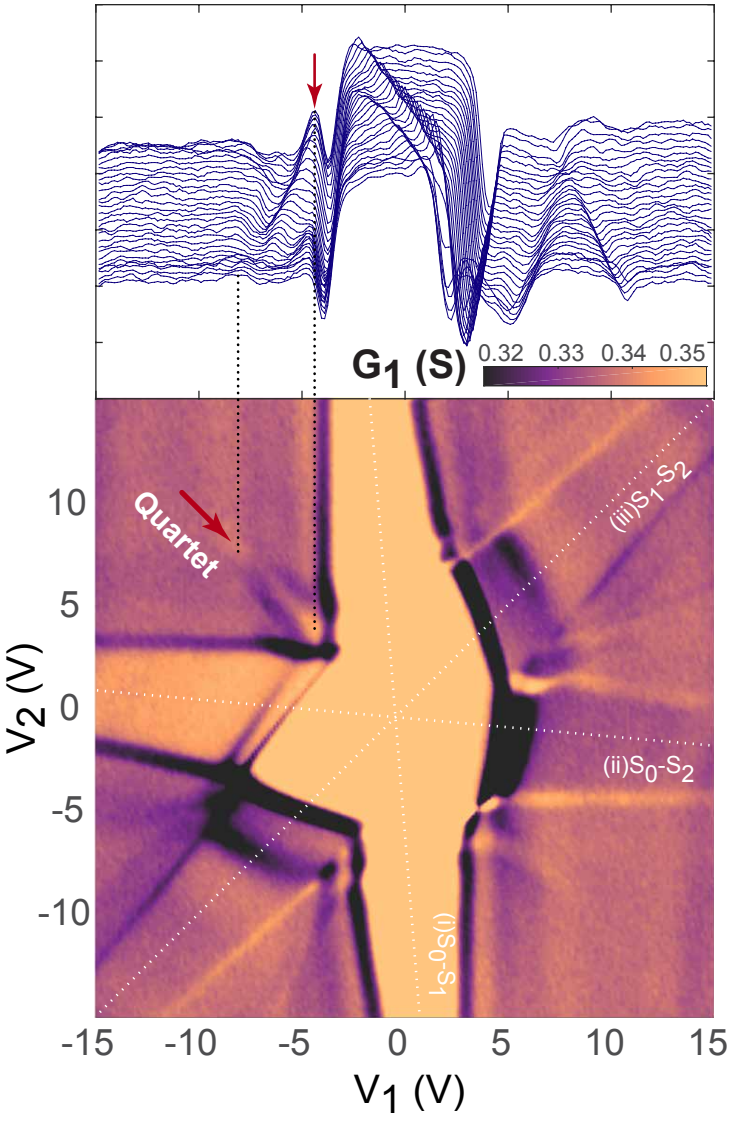

Figure 4.12: Color plot showing the differential conductance of the first terminal $G_1 (= dI_1/dV_{AC})$ as a function of the DC bias voltages V_1 and V_2. The vertical, horizontal and +45 degree signals correspond to the Josephson currents drawn in figure 4.11 (i), (ii), (iii), respectively. The quartet supercurrent, illustrated in figure 4.11 (iv), is found along -45 degree line (when $V_1 = -V_2$) as pointed out with the red arrow. The width of these signals marks the value of critical current. Note that the axes are the DC voltages applied in the circuit shown in figure 4.10. Depending on the regime of the Josephson junctions, these DC voltages can be converted to bias current (for V_i<V_c) by Eq.4.8 or bias voltage (for $V_i > V_c$) by Eq.B.4.

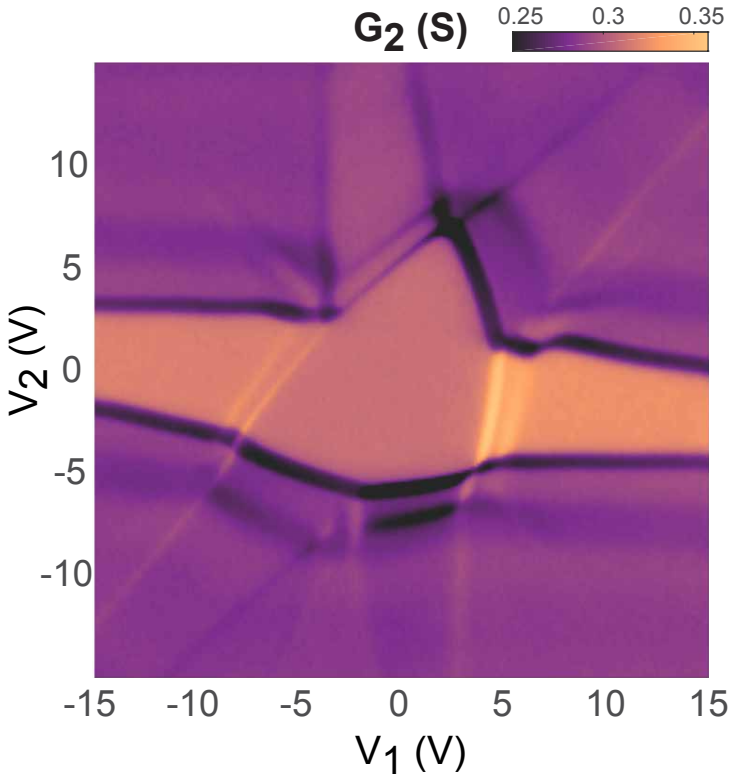

Figure 4.13: Color plot showing the differential conductance of the second terminal $G_2(= dI_2/dV_{AC})$ as a function of the DC bias voltages V_1 and V_2. The features of G_1 in figure 4.12 can also be found in this measurement. However, the overall conductance is lower than G_1.

Quartet supercurrent

The quartet signal is much weaker compared to the Josephson current due to the following reasons. First of all, Josephson current between two terminals involves two Andreev reflections, which is a 4th-order process (the probability is proportional to $|r_{he}|^4$, where $|r_{he}|$ is the Andreev reflection coefficient). The quartet current comes from an 8th-order process with four successive Andreev reflections and therefore the probability is proportional to $|r_{he}|^8$. Secondly, the whole length of the quartet pro-

cess is twice as long as the Josephson process, making it more vulnerable to the decay of coherence length. Lastly, outside of the zero-bias-voltage region there are multiple Andreev reflections (MAR) in the background, smearing out the quartet signal.

For comparison, we show the differential conductance measured at the second lead, G_2, in figure 4.13 and the similar features can be found. We notice that overall G_2 is lower than G_1, hinting asymmetric couplings between each pair of contacts.

4.3 Quartets in the Presence of Magnetic Field

In order to discuss the effect of magnetic field, we have to introduce the vector potential $\boldsymbol{A}$. For a two-terminal junction in the presence of a magnetic field, the full gauge-invariant phase difference should include the Aharonov-Bohm phase:

$$\widetilde{\varphi} \equiv \Delta\varphi - (2\pi/\Phi_0) \int \boldsymbol{A} \cdot d\boldsymbol{s}, \tag{4.9}$$

where Φ_0 is the flux quantum and the integral is from one superconducting lead to the other.

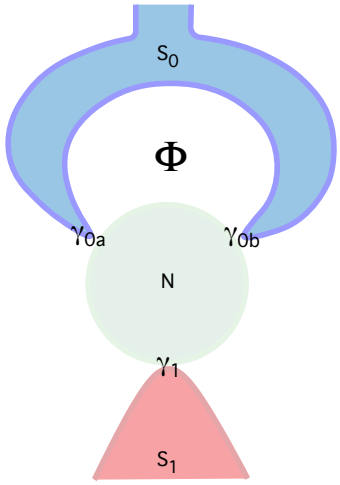

Figure 4.14: Two-terminal junction with a loop. γ's are the couplings between the superconducting contacts and the normal island.

4.3.1 Two-terminal junction with a loop

Before diving into our three-terminal junction with a loop, it is very helpful to consider a warm-up example of the two-terminal case with the simple dot model: a normal dot connected to two superconducting terminals with one of them forming a loop, as shown in figure 4.14. The phase difference between the two terminals is φ. Using the infinite-gap dot model introduced in Secion 2.4.2, at each contact we assign a parameter indicating how high the chance of tunneling between the contact and the normal dot is; these coupling strengths are denoted as γ_{0a}, γ_{0b}, and γ_1, respectively.

We can then construct the Andreev bound states and find the currents they carry. Depending on the chosen gauge, the ABS energies are (for a resonant dot where $\varepsilon_0 = 0$):

$$E_{ABS}(\varphi,\Phi)=\begin{cases}\pm\left|\gamma_{0a}+\gamma_{0b}e^{i\Phi}+\gamma_1 e^{i\varphi}\right| & \text{, non-symmetric gauge}\\ \pm\left|\gamma_{0a}e^{-i\Phi/2}+\gamma_{0b}e^{i\Phi/2}+\gamma_1 e^{i\varphi}\right| & \text{, symmetric gauge}\end{cases} \tag{4.10}$$

For example, let us consider a symmetric loop such that $\gamma_{0a}=\gamma_{0b}=\gamma_0/2$. Then with the symmetric gauge, the ABS energies become

$$\begin{aligned}E_{ABS}(\varphi,\Phi)&=\pm\left|\frac{\gamma_0}{2}e^{-i\Phi/2}+\frac{\gamma_0}{2}e^{i\Phi/2}+\gamma_1 e^{i\varphi}\right|\\&=\pm\left|\gamma_0\cos(\Phi/2)+\gamma_1 e^{i\varphi}\right|,\end{aligned} \tag{4.11}$$

where we get an effective coupling for the loop, which is $\gamma_0\cos(\Phi/2)$.

More generally, the effective coupling of the loop is a complex number and the first two terms in Eq.4.10 can be combined and written as:

$$\gamma_0(\Phi)=\gamma_0' e^{i\alpha(\Phi)}, \tag{4.12}$$

where

$$\tan\alpha=\frac{\gamma_{0b}-\gamma_{0a}}{\gamma_{0b}+\gamma_{0a}}\tan(\Phi/2), \tag{4.13}$$

$$\gamma_0'(\Phi)=\sqrt{\gamma_{0a}^2+\gamma_{0b}^2+2\gamma_{0a}\gamma_{0b}\cos\Phi}. \tag{4.14}$$

We then have

$$E_{ABS}(\varphi, \Phi) = \pm \left| \gamma_0'(\Phi) + \gamma_1 e^{i[\varphi - \alpha(\Phi)]} \right|. \tag{4.15}$$

It is now obvious that as the flux Φ is varied, the overall junction phase would have an additional term $\alpha(\Phi)$. We can define a gauge-invariant phase as

$$\widetilde{\varphi} \equiv \varphi - \alpha(\Phi). \tag{4.16}$$

Then Eq.4.15 immediately shows that our two-terminal junction with a loop is actually equivalent to a simple two-terminal junction (Eq.2.61). Except that now one of the contact couplings, $\gamma_0'(\Phi)$, is flux-dependent. Note that in Chapter 2, we assumed γ's are real. In fact, they can be complex when a magnetic field is applied and time reversal symmetry is broken. In this example, the flux adds an extra phase factor $e^{\pm i\Phi/2}$ to the loop γ's. However, in the calculation this phase factor is incorporated as a shift of the superconducting phase and we still have real γ's.

4.3.2 Quartet in three-terminal junction with a loop

Now let us move on to the simple dot model for our actual device, a three-terminal Josephson junction with a loop. As shown in figure 4.15, there are four contact couplings in total, γ_1, γ_2 for the first two terminals and γ_{0a}, γ_{0b} for the loop.

The superconducting phase of the loop is chosen to be the reference, while the other two terminals

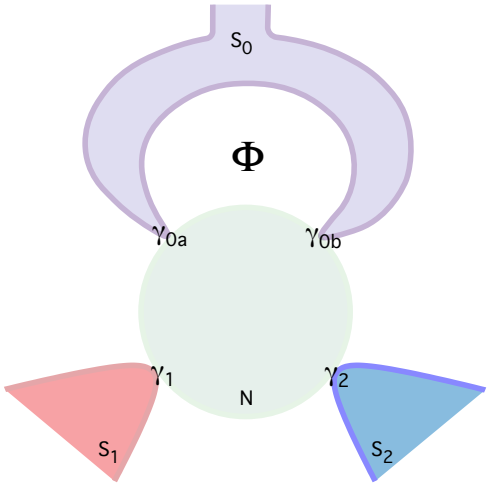

Figure 4.15: Three-terminal junction with a loop. γ's are the couplings between the superconducting leads and the normal island.

S_1 and S_2 have the phase φ_1 and φ_2, respectively. Then the ABS energies in the proximitized region (consider a resonant dot) are written as

$$E_{ABS}(\varphi_1, \varphi_2, \Phi) = \pm \left| \gamma_{0a} + \gamma_{0b} e^{i\Phi} + \gamma_1 e^{i\varphi_1} + \gamma_2 e^{i\varphi_2} \right|. \tag{4.17}$$

Following the same argument carried out for a two-terminal junction with a loop, we now can express the ABS energies in terms of the original couplings γ_1, γ_2 and the effective loop coupling $\gamma_0'(\Phi)$ along with a gauged quartet phase

$$\widetilde{\varphi}_q \equiv \varphi_q - 2\alpha(\Phi). \tag{4.18}$$

Generally, Eq.4.17 can be rewritten as

$$E_{ABS}(\varphi_1, \varphi_2, \Phi) = \pm \left| \gamma_0'(\Phi) + \gamma_1 e^{i(\widetilde{\varphi}_q + \varphi_r)/2} + \gamma_2 e^{i(\widetilde{\varphi}_q - \varphi_r)/2} \right|. \tag{4.19}$$

with $\widetilde{\varphi}_q$ the gauged quartet phase and φ_r the running phase introduced in Section 4.1.2.

For simplicity, let us consider again a symmetric junction where the two loop couplings are the same, $\gamma_{0a} = \gamma_{0b} = \gamma_0/2$. By choosing a symmetric gauge, the ABS energies are

$$\begin{aligned} E_{ABS}(\varphi_1, \varphi_2, \Phi) &= \pm \left| \frac{\gamma_0}{2} e^{-i\Phi/2} + \frac{\gamma_0}{2} e^{i\Phi/2} + \gamma_1 e^{i\varphi_1} + \gamma_2 e^{i\varphi_2} \right| \\ &= \pm \left| \gamma_0 \cos(\Phi/2) + \gamma_1 e^{i(\widetilde{\varphi}_q + \varphi_r)/2} + \gamma_2 e^{i(\widetilde{\varphi}_q - \varphi_r)/2} \right|. \end{aligned} \tag{4.20}$$

This shows that for quartets existing in a three-terminal Josephson junction with a loop, the bound state is formed the same way as in a three-terminal junction without a loop. The difference is that the Hamiltonian is now responsive to the magnetic flux. As shown in figure 4.16, our device is equivalent to a simple three-terminal junction but with one of the contact couplings tunable by the flux Φ. This provides an additional aspect to probe the system experimentally.

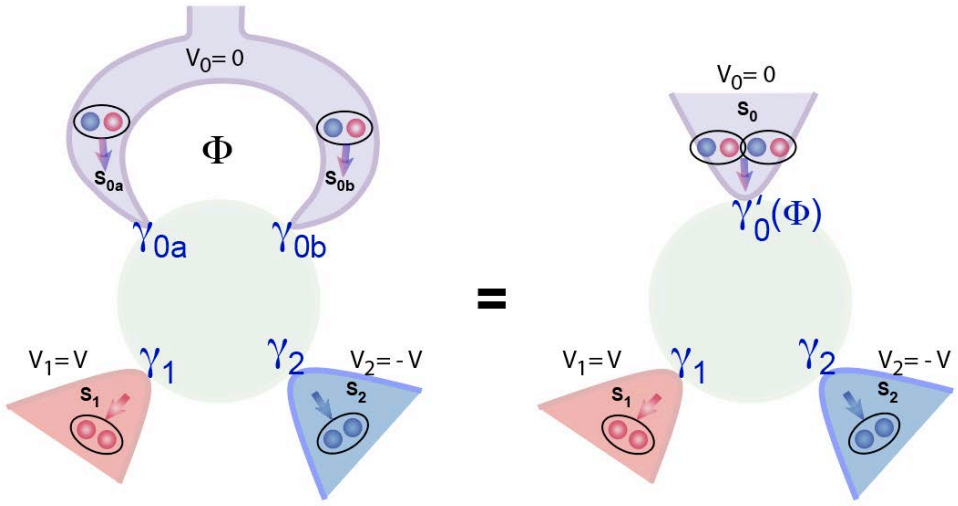

Figure 4.16: Three-terminal junction with a loop is equivalent to three-terminal junction with no loop but having one of the contact couplings dependent on Φ.

4.4 Adiabatic Approximation: Effective Andreev Bound State

In the beginning of this chapter, we showed that the ABS energies $E(\varphi_q, \varphi_r)$ in a quartet system are two-dimensional manifolds (figure 4.5), of which the running phase φ_r is winding in time with a velocity $4eV/\hbar$. Having $V = 0^+$ means that φ_r is changing extremely slowly. One can therefore use the adiabatic approximation to average out the running phase and obtain an "effective" ABS energy for the non-equilibrium three-terminal junction. In the resonant dot model for our three-terminal

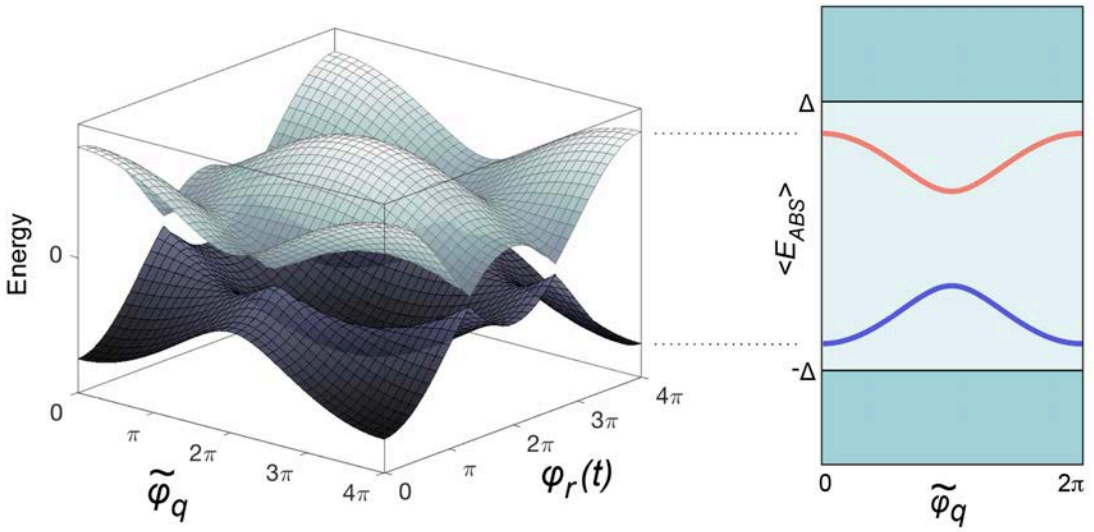

Figure 4.17: At low V, φ_r has slow and smooth variation in time. By averaging over the whole period of φ_r, we get an effective ABS $\langle E_{ABS}\rangle$ depending only on $\widetilde{\varphi}_q$, resembling the single junction ABS at equilibrium.

junction with a loop (Eq.4.19), the averaged energies read

$$\langle E_{ABS}(\widetilde{\varphi}_q,\Phi)\rangle$$

$$=\frac{1}{4\pi}\int_0^{4\pi} d\varphi_r \left|\gamma_{0a}+\gamma_{0b}e^{i\Phi}+\gamma_1 e^{i(\widetilde{\varphi}_q+\varphi_r)/2}+\gamma_2 e^{i(\widetilde{\varphi}_q-\varphi_r)/2}\right| \tag{4.21}$$

$$=\frac{1}{4\pi}\int_0^{4\pi} d\varphi_r \left|\gamma_0'(\Phi)e^{i\alpha(\Phi)}+\gamma_1 e^{i(\widetilde{\varphi}_q+\varphi_r)/2}+\gamma_2 e^{i(\widetilde{\varphi}_q-\varphi_r)/2}\right|. \tag{4.22}$$

At zero flux, the effective ABS energies for quartets are the same as those of an equilibrium Josephson junction, depending only on a single phase variable $\widetilde{\varphi}_q$. At non-zero magnetic field, the flux Φ comes into play via the effective coupling $\gamma_0'(\Phi)$.

The adiabatic quartet current in the loop can then be acquired from taking derivative of $\langle E_{ABS}\rangle$ with respect to the phase of the loop, or with respect to the quartet phase $\widetilde{\varphi}_q/2$. Taking its maximum

value provides the adiabatic quartet critical current:

$$I_{q,adiab} = -2e\frac{\partial \langle E_{ABS} \rangle}{\partial \widetilde{\varphi}_q} \tag{4.23}$$

$$I_{qc,adiab} = \mathrm{Max}_{\widetilde{\varphi}_q}\left[-2e\frac{\partial \langle E_{ABS} \rangle}{\partial \widetilde{\varphi}_q}\right]. \tag{4.24}$$

$I_{qc,adiab}$ (I_{qc} for short) is the important experimental observable which reflects the landscape of the effective ABS spectrum. Therefore, our goal is to inspect how the quartet current in the device is modulated as other experimental knobs are tuned. For the rest of this section, we use the simple dot model to demonstrate how the ABS energies are engineered by the contact couplings and gate voltage, resulting in the evolution of $I_{qc}(\Phi)$.

4.4.1 Engineering the effective ABS via contact couplings

To start with, we fix the first two superconducting leads to have couplings to the dot with $\gamma_1 = 0.1$ and $\gamma_2 = 0.3$ (see figure 4.18 top panel). Another condition is that the sum of the loop couplings $\gamma_{0a} + \gamma_{0b} = 1$. By varying γ_{0a} we find that the second harmonic appears in I_{qc} as a function of Φ when the loop contacts are nearly symmetric. In the regime of strong asymmetry between γ_{0a} and γ_{0b}, $I_{qc}(\Phi = \pi)$ is found to be larger than $I_{qc}(\Phi = 0)$. If we increase the coupling of the second lead to be much stronger than the first lead (figure 4.18 bottom panel with $\gamma_1 = 0.1, \gamma_2 = 0.9$), then we always find maximum I_{qc} at $\Phi = 0$.

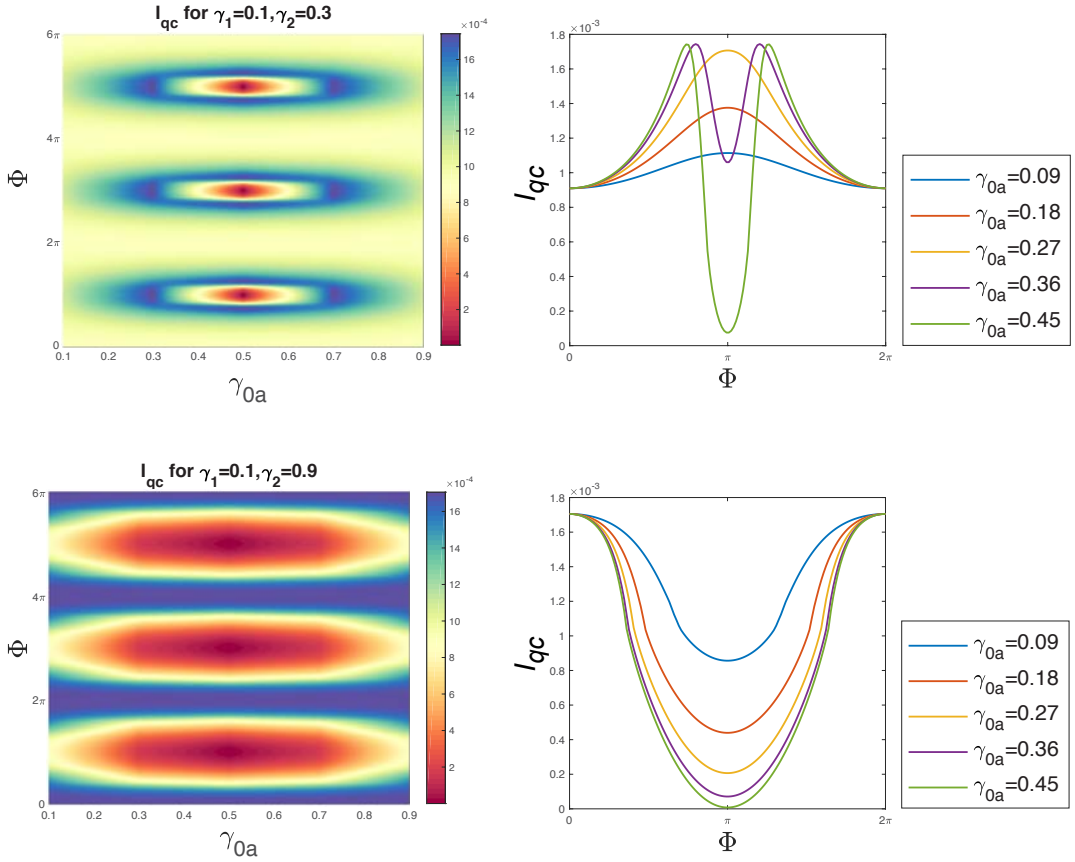

Figure 4.18: $I_{qc}(\Phi)$ for different combinations of contact couplings. Top: the second harmonic appears when the loop is nearly symmetric. Bottom: strong asymmetry between the first and second lead. Maximum value of I_{qc} always occurs at zero flux.

To further see how we can extract information on the ABS spectrum from $I_{qc}(\Phi)$, let us consider a symmetric loop (the green curve with $\gamma_{0a} = 0.45$ in figure 4.18 top panel). The maximum I_{qc} occurs around $\Phi = 0.74\pi$ while the minimum is at $\Phi = \pi$. The corresponding ABS spectra (before the adiabatic approximation of averaging over φ_r) are illustrated in figure 4.19. Since the critical current is proportional to the derivative of the energy (Eq.4.23), one can see that at $\Phi = 0.74\pi$, the Andreev gap is at its minimum and the intense deformation in the proximity of the closing point results in the

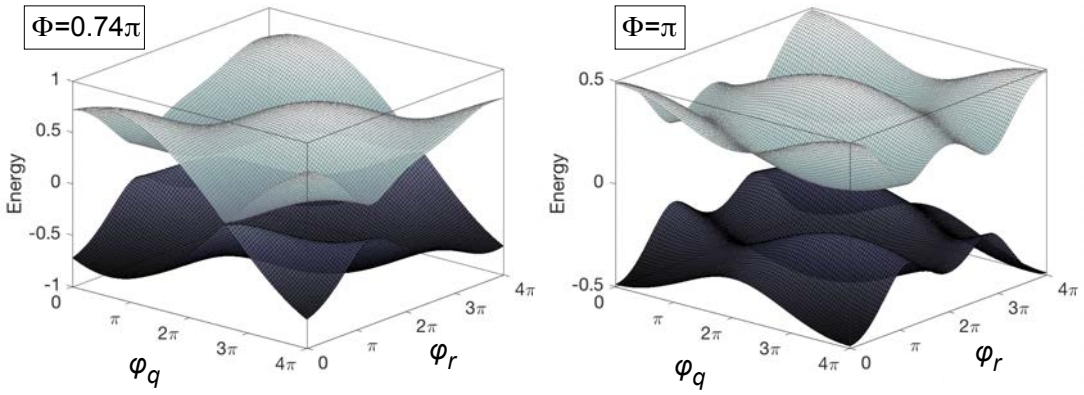

Figure 4.19: For a nearly symmetric loop, the contact couplings are fixed at $(\gamma_1, \gamma_2, \gamma_{0a}, \gamma_{0b}) = (0.1, 0.3, 0.45, 0.54)$. Left: ABS spectrum at $\Phi = 0.74\pi$ generates the maximum I_{qc} with the Andreev gap closing. Right: ABS spectrum at $\Phi = \pi$ has minimal variation and generates minimum I_{qc} .

large critical current. On the contrary, at $\Phi = \pi$, there is always a sizable Andreev gap throughout the whole spectrum. The reduced modulation amplitude in the manifolds explains the why the critical current is small.

4.4.2 Engineering the effective ABS via gate

In our device, another knob to tune the system is the gating of graphene. The applied gate voltage changes the chemical potential of the graphene channel region. Also, the gate voltage can change the density of graphene underneath Al contacts, modulating the couplings between graphene and the superconductors. In the simple dot model, the gating effect can be incorporated by changing the

single-level dot energy ε_0 in Eq.2.60:

$$E_{ABS} = \pm\sqrt{\varepsilon_0^2 + |\sum_i \gamma_i e^{i\varphi_i}|^2}.$$

For certain combinations of the contact couplings γ's, $I_{qc}(\Phi)$ behaves in distinct manners for different values of ε_0. For example, we can fix the couplings to be $(\gamma_1, \gamma_2, \gamma_{0a}, \gamma_{0b}) = (0.1, 0.3, 0.7, 0.3)$ and calculate the critical current I_{qc} as a function of ε_0 and the flux Φ. The result is shown in figure 4.20 as a color plot and its vertical linecuts at different values of ε_0. When we have a resonant dot ($\varepsilon_0 = 0$), the critical current has maximum value (peak) at $\Phi = \pi$. But as the dot energy is increased, the peak starts to split into two and gradually turns into a dip (minimum) at $\Phi = \pi$. The transition $I_{qc}(\Phi)$ undergoes is clearly shown in the linecuts.

Gate dependence data

The gating effect in the toy-model can be compared to our experimental results. At different backgate voltages we fix the bias voltage V applied on the junction to be the same and then measure the quartet conductance while sweeping magnetic field. Putting all the $G(\Phi)$ curves from measurements with different values of backgate together (figure 4.21), we see a similar evolution to that of the dot model (figure 4.20 bottom panel). At certain gate voltage ($V_{bg} \approx 10, 30$ V for example), $G(\Phi)$ exhibits Φ/Φ_0 as the dominant period. In between these gate voltages, $G(\Phi)$ exhibits $\Phi/2\Phi_0$ periodicity. In spite of the simplicity, the dot model still captures the essence of quartet physics and is consistent with

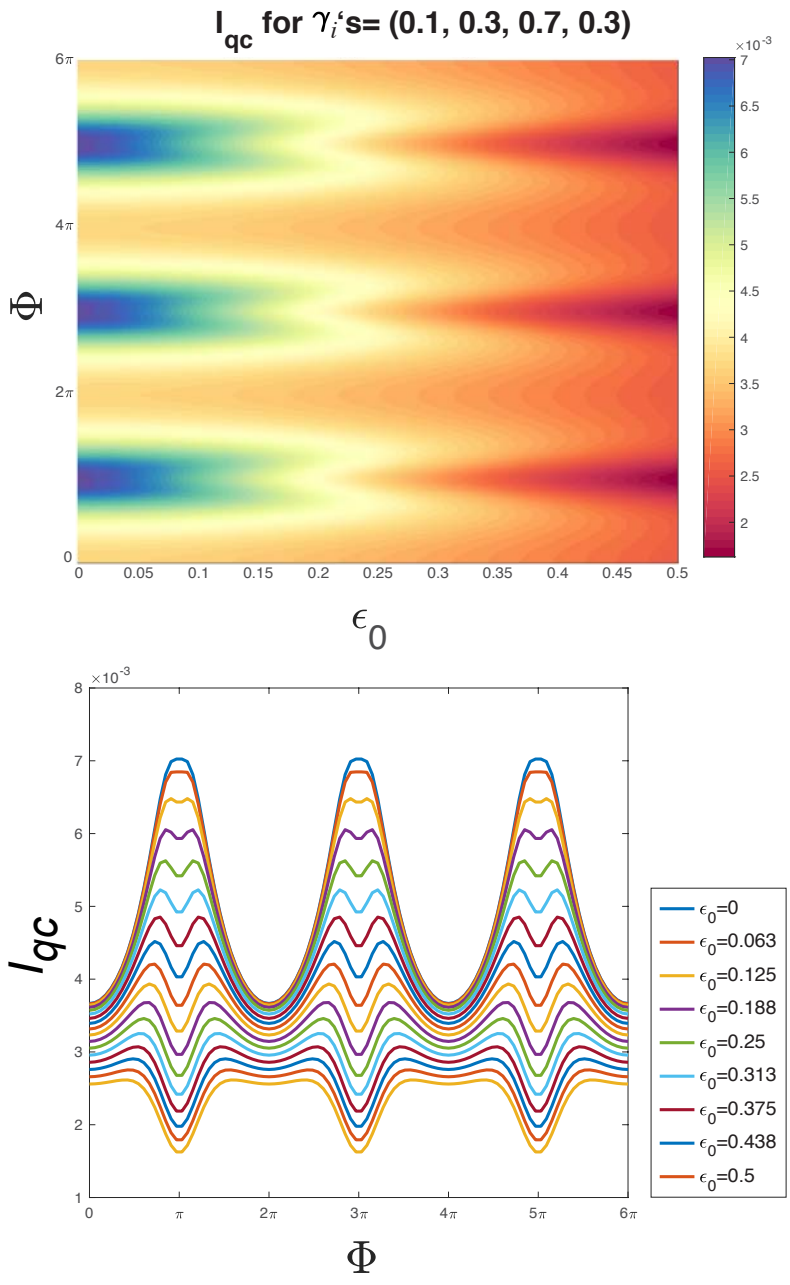

Figure 4.20: Simulated critical current with the contact couplings fixed at $(\gamma_1, \gamma_2, \gamma_{0a}, \gamma_{0b}) = (0.1, 0.3, 0.7, 0.3)$. Top panel: I_{qc} as a function of the dot energy ε_0 and the flux (Φ). Bottom panel: vertical linecuts of the color plot, $I_{qc}(\Phi)$ at different values of ε_0. The peaks at half flux $(\Phi = \pi)$ gradually evolve into dips as ε_0 increases.

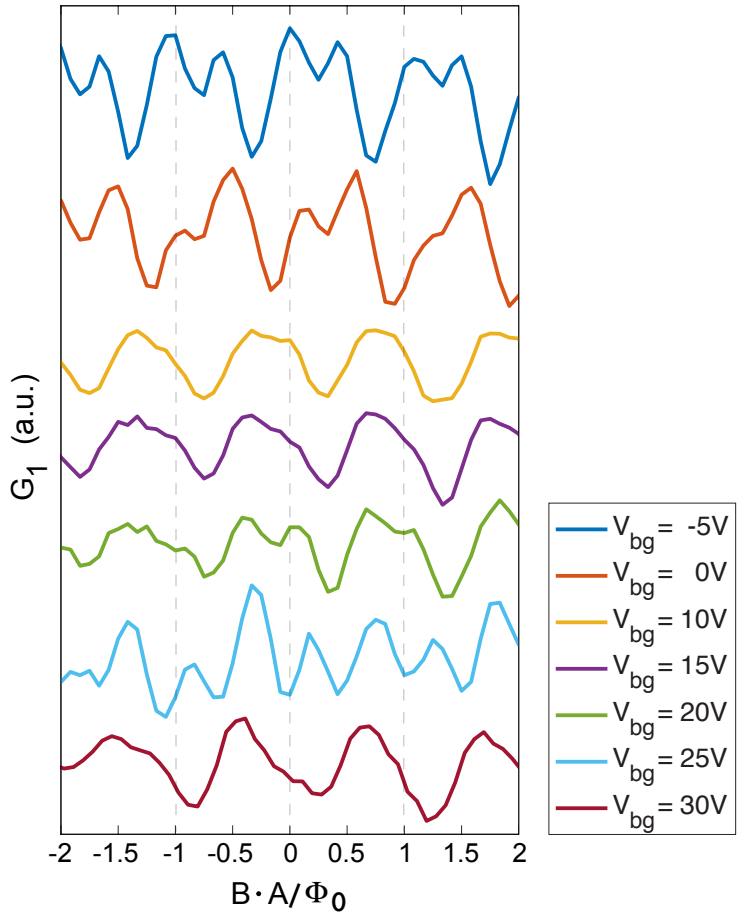

Figure 4.21: Measured quartet conductance (G_1) as a function of magnetic flux, $(B \cdot A)/\Phi_0$, for different backgate voltages. B is the applied field, A is the area enclosed by the device loop and Φ_0 is the superconducting magnetic flux quantum. $G_1(\Phi)$ is proportional to $I_{qc}(\Phi)$, which is calculated and shown in figure 4.20. The second harmonic appears at certain gate voltages.

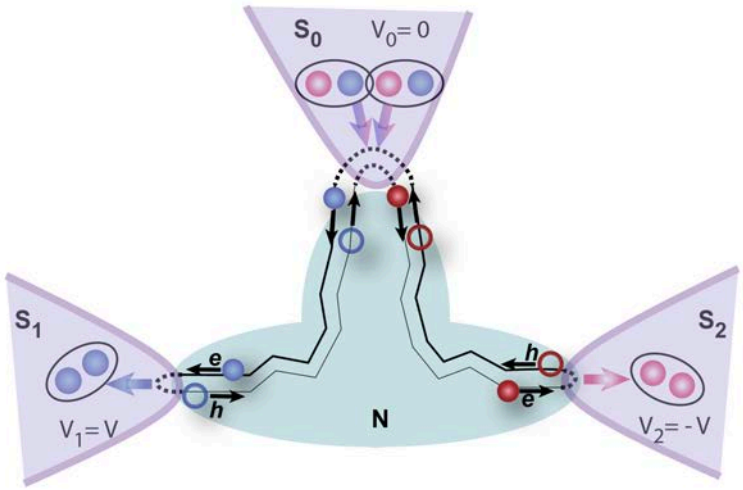

Figure 4.22: Conventional three-terminal quartet process. The process is immune to disorder in the proximitized region.

the experimental data. The modulated periodicity of $G(\Phi)$ is closely related to the appearance of different types of quartet process involving the loop electrodes that we will discuss in the next section.

4.5 Different Types of Quartet Process

In this section, we consider spatially distributed quartet procedure in the superconducting electrodes. As shown in figure 4.22, for a simple three-terminal junction, the entangled Cooper pairs are transferred into the grounded terminal while the Andreev reflected hole/electron will trace the time-reversed path of its partner and form the nonlocal supercurrent. Therefore, this process is immune to disorder in the proximitized region. This is the type of quartet process that has already been observed in the previous experiments with three-terminal Josephson junctions based on disordered metal and

nanowire.[39,40] In our device, one of the terminals is split into two contacts to form a loop, enabling phase control to probe the quartet state. One may wonder if any new phenomenon would rise from this special setup. For instance, since both contacts of the loop are at the same potential, is there any difference between them from the Cooper pairs' perspective? In this section, we will first discuss the conventional quartet process when there are four contacts and then present a new process that appears exclusively in our device.

4.5.1 Conventional quartet process

Adding another contact to the grounded lead means that the two entangled Cooper pairs now have two choices to enter the grounded terminal. The same process as in figure 4.22 can now take place with the Cooper pairs transferred together into either contact S_{0a} or S_{0b}, as illustrated in figure 4.23.

To further inspect the flux dependence of the supercurrent carried by these conventional quartets, we consider the phase at each contact. As shown in figure 4.23, the phases between the two loop contacts differ by the flux Φ. Every time an Andreev reflection occurs, the reflected quasiparticle will pick up the phase of the superconducting lead. In the conventional quartet process, the two Andreev reflections both happen at the same contact, meaning there will be another factor of 2 in the phase factor that the particles acquire:

$$e^{i2\varphi_0} \text{ at } S_{0a} \tag{4.25}$$

$$e^{i2(\varphi_0+\Phi)} \text{ at } S_{0b}. \tag{4.26}$$

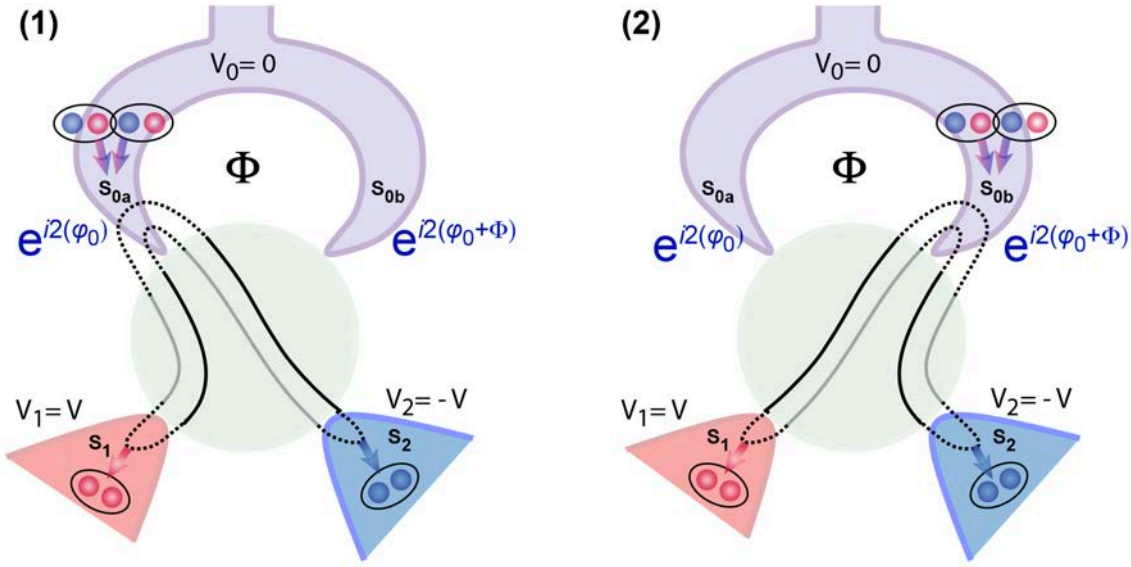

Figure 4.23: Conventional quartet among four contacts. Either S_{0a} or S_{0b} of the loop participates the process. At S_{0i} contact, the Andreev process takes place twice (the dotted line represents electron-hole conversion).

It is clear that if there is only process (1) or only process (2) in the system, the situation is the same as having quartet in a simple three-terminal junction and hence the quartet current would not have any flux dependence. On the other hand, if both (1) and (2) exist at the same time, the situation is no longer trivial due to the interference between the two processes. Let us consider the adiabatic quartet current and critical current that are defined in the previous section by Eq.4.23, 4.24:

$$I_{q,adiab} = -2e\frac{\partial \left\langle E_{ABS}(\widetilde{\varphi}_q, \Phi)\right\rangle}{\partial \widetilde{\varphi}_q}$$

$$I_{qc,adiab} = \mathrm{Max}_{\widetilde{\varphi}_q}\left[-2e\frac{\partial \left\langle E_{ABS}(\widetilde{\varphi}_q, \Phi)\right\rangle}{\partial \widetilde{\varphi}_q}\right].$$

When $\Phi = \pi$, at lead S_{0b} we have the phase factor

$$e^{i(2\varphi_0+2\pi)} = e^{i2\varphi_0}, \tag{4.27}$$

which is the same as the phase factor when $\Phi = 0$. This means that the observables such as the quartet critical current would have the relation:

$$I_{qc}(\Phi = 0) = I_{qc}(\Phi = \pi), \tag{4.28}$$

hence having a periodicity of π in flux.

4.5.2 Split quartet process

The second type of process will not survive if there is disorder in the normal island, since the butterfly-like trajectory (figure 4.24) does not retrace itself and will be averaged out. It is given the name "split quartets" since the entangled Cooper pairs are separated into the two contacts of the grounded loop. Following the same analysis, the phase factor of this process is

$$e^{i(\varphi_0+\Phi)} \tag{4.29}$$

without a factor of 2 since each contact would only experience a single Andreev reflection. Therefore, the quartet current has a periodicity of 2π in flux. We should note that at $\Phi = \pi$, the current has

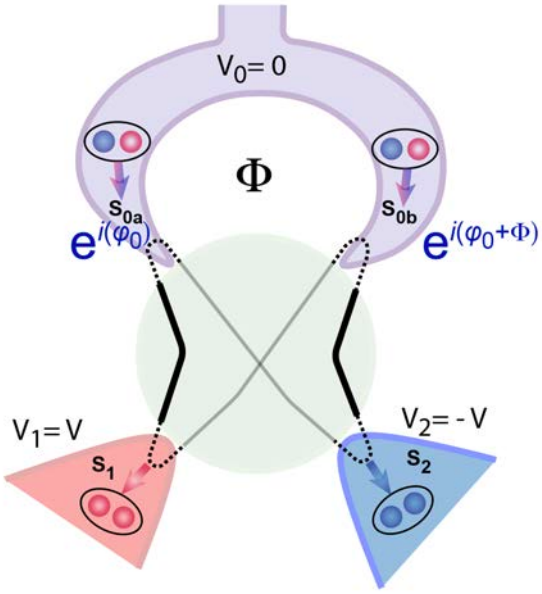

Figure 4.24: Split quartet process among four contacts, which involves both S_{0a} and S_{0b} in one cycle. But at each lead, there is only a single Andreev process (one dotted line).

the opposite sign but the same magnitude as the current at $\Phi = 0$. It implies that the critical current measured at $\Phi = 0$ and $\Phi = \pi$ would be identical because it is defined as the maximum absolute value of the current.

4.5.3 Interference and flux dependence of I_{qc}

Even though microscopically we can describe the difference between the conventional process and the split quartets, experimentally we cannot distinguish them by measuring $I_{qc}(\Phi)$ since the critical current is always positive and they both will show the same periodicity of π. This is when interference comes to the rescue. Interestingly, with the three quartet processes (two conventional and one split)

happening simultaneously in the device and interfere with each other, the periodicity of the critical current in flux becomes 2π.

As shown earlier, what we measure in experiment is the differential conductance in the junction $G = dI/dV$, which is proportional to the quartet critical current I_{qc}. In the previous section figure 4.21 shows the gate dependence of the quartet conductance as a function of flux. While for some of the gate voltages, the periodicity indeed is one flux quantum (with the area enclosed by the loop). Now we know it is not as trivial or straightforward as it may seem since it implies the presence of the split quartets. More precisely, there is interference among the conventional quartets and the split quartets. For some gate voltages, the periodicity becomes half flux quantum, indicating the absence of the split quartet. Since different types of quartet process depend on the coupling strength of each contact, it makes sense that we can modulate the occurrence of these processes in the system with gate voltage. This observation expands the richness of our three-terminal Josephson junction with a loop.

In summary, in a three-terminal Josephson junction Andreev bound states can be formed in the context of quartet, which consists of four entangled electrons and carries nonlocal supercurrents. For the first time, quartet is observed in a 2D system, our graphene-based multi-terminal Josephson junction. Furthermore, the device design with a loop enables phase control over the system and therefore unveils the existence of a new type of quartet process, the split quartet. We also discussed the adiabatic approximation that is valid when the bias voltage V is in the 0^+ limit. The calculation from a simple dot model is consistent with the gate dependence experimental data, suggesting that we can modulate the effective Andreev bound states via backgate. In the next chapter, we will march into the finite voltage regime, in which the running phase φ_r plays a critical role for the dynamics of the system.

5

Emergence of the Floquet Spectrum

So far, we have learned about the quartet system, which in principle has a time-dependent Hamiltonian due to the applied voltage bias. As shown in figure 5.1, the original pair of Andreev bound states is dynamically evolving in time along φ_r. When the variation is infinitely slow, the system is in the adiabatic regime and will always stay in the ground state without any transitions to the excited

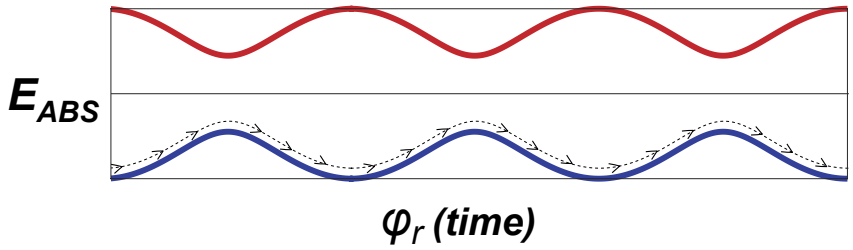

Figure 5.1: Time-dependent Andreev bound states for a quartet process in the adiabatic regime at fixed φ_q. There is no transition between the two levels; the system stays in the initial state.

state. This is the regime we focused on in the previous chapter: when the control voltage V is in the 0^+ limit and much smaller than the gap at any given quartet phase φ_q, we can find the effective energy spectrum and current near equilibrium by averaging over the running phase φ_r.

Experimentally, it is rather difficult to observe the quartet in this adiabatic regime because it is always overshadowed by the two terminal Josephson currents, as marked in figure 5.2, which shows the $V_1 - V_2$ scan in the quartet measurement. When we move to the region where the quartet is distinguishable from the other supercurrents, we are in the finite voltage regime and the dynamics of the running phase must be taken into account:

$$\varphi_r(t) = \varphi_1 - \varphi_2 + 4eVt/\hbar. \tag{5.1}$$

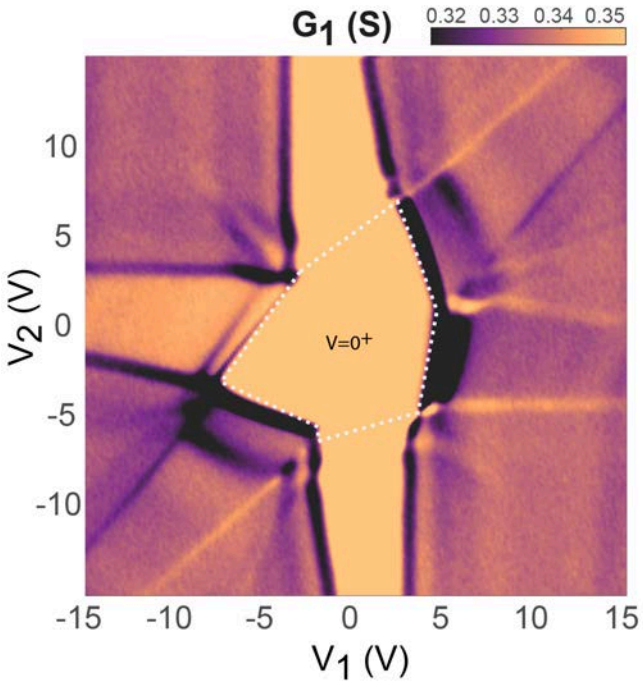

Figure 5.2: In the $V_1 - V_2$ scan of the quartet measurement, the $V = 0^+$ region is the area enclosed by the white dotted line. This is the region where the quartets are in the adiabatic regime, but they are also overshadowed by the Josephson currents.

5.1 Landau-Zener transition

In the dynamical Andreev bound states there are non-adiabatic effects due to the voltage V. Therefore, it is useful to recap the Landau-Zener transition.[47] As shown in figure 5.3, when the spectrum is varying in time with non-zero velocity, v, transitions between the two Andreev levels may occur around an avoided crossing (when the gap between the two Andreev levels is at minimum, i.e., the Andreev gap Δ_{min}). If we assume the system is initially in the lower Andreev level, then the Landau-Zener

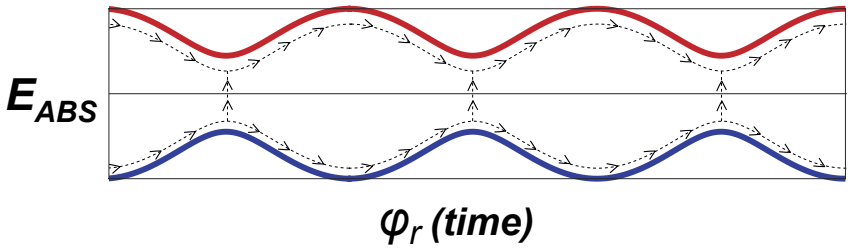

Figure 5.3: Andreev bound states as a function of $\varphi_r(t)$. Landau-Zener transitions between the two states happen at avoided crossings.

formula gives us the probability of finding the system in the upper level:

$$P = \exp\big(-2\pi\delta\big), \quad \delta = \frac{\Delta_0^2}{4v}. \tag{5.2}$$

where v is how fast the spectrum is varying. It is proportional to the voltage V:

$$v = \frac{dE}{dt} = \frac{dE}{d\varphi_r}\frac{d\varphi_r}{dt} = \frac{4eV}{\hbar}\left(\frac{dE}{d\varphi_r}\right). \tag{5.3}$$

While figure 5.3 depicts the non-adiabatic effect caused by the voltage V, it does not provide a complete picture of the quartets at finite V. Since the energy spectrum is periodic in φ_r, we now have a time-periodic problem to solve. In the next section, we will take a look at a few examples of other periodically-driven systems before getting back to our quartet system.

5.2 Driven Two-level Systems

A quote from J. J. Sakurai in the text book Modern Quantum Mechanics: "*In fact, it is amusing to see that as many as four Noble Prizes in physics have been awarded to those who exploited time-dependent two-state systems of some form.*[*]"

In contrast to time-independent quantum theory, it is very rare to have exactly solvable quantum systems that are time-dependent. In 1937, I. I. Rabi studied nuclei with 1/2-spin interacting with a circularly polarized magnetic field,[48] which is a classic example of a driven two-level system. Consider an atom in which an electron can only be in the ground state or excited state with an oscillating electromagnetic field applied to it. By switching to the rotating frame, the fast oscillating term in the Hamiltonian quickly averages out and can be neglected. This is the so-called rotating wave approximation (RWA). One finds that when the driving frequency corresponds to an energy close to the energy gap between the two levels, the probability of finding the atom in the ground and excited state oscillates in time, which is known as the Rabi-oscillation.

In Chapter 2 we discussed the DC Josephson effect and how a dissipationless supercureent can flow through an SNS junction without any applied voltage. In the simplest weak link, when the channel is shorter than the superconducting coherence length, a pair of Andreev bound states that carry opposite directions of supercurrents forms in the proximitized region. This pair of Andreev states is a

[*]Rabi (1994) on molecular beams and nuclear magnetic resonance; Bloch and Purcell (1952) on magnetic field in atomic nuclei and nuclear magnetic moments; Townes, Basov, and Prochorov (1964) on masers, lasers, and quantum optics; Kastler (1966) on optical pumping.

realization of a two-level system with well characterized parameters.

The ground state, where only the lower Andreev level is occupied, has been probed through measurements of the current-phase relation.[49] It is also of great interest to probe the excited state. Via quasiparticle tunneling spectroscopy, excitations of the excited state created by adding or removing an electron from the lower Andreev level have been observed.[50,51] More recently, microwave spectroscopy has shown coherent control of Andreev bound states with resonant excitation by microwaves.[52,53,54]

Besides probing directly the transitions between the Andreev levels, modulation of the current flowing in the junction has been studied as well. Experimentally, one can control the occupation of the supercurrent-carrying states through non-equilibrium quasiparticle injection such that the direction of the supercurrent may even be reversed.[55] † Regarding ballistic transport, there are a few theoretical investigations on how microwave irradiation can modify the equilibrium Josephson current drastically.[56,57,58]

If the strength of the driving field used to induce transition is significantly smaller than the natural transition and the frequency is close to the transition frequency, the system would go through Rabi oscillations between the two energy eigenstates. This scenario can be well described by the rotating wave approximation (RWA)[48] with sinusoidal oscillations. However, in the strong driving regime, the dynamics becomes very complex containing several frequency components and the RWA breaks down.[59,60,61]

† Even though this experiment was done with mesoscopic diffusive metal, in which the Andreev bound states are not the natural concept to describe the supercurrent, there are still supercurrent-carrying states in the normal metal. The total supercurrent also depends on the occupation of these states, analogous to the occupation of Andreev bound states in a ballistic system.

While the microwave scenario gives us some intuition about our quartet system, the periodic driving originates from the running phase $\varphi_r(t)$ and hence is intrinsic to the junction; the strength of this perturbation is comparable to the energy scale of the system's intrinsic dynamics and we are no longer in the weak driving limit. Therefore, a different theoretical approach is needed. This is where Floquet theory comes in. Its application provides a general framework that can be used to solve the periodically-driven systems in all regimes.

5.3 Floquet Theorem: Bloch's Theorem in Time

"*When I started to think about it, I felt that the main problem was to explain how the electrons could sneak by all the ions in a metal....By straight Fourier analysis I found to my delight that the wave differed from the plane wave of free electrons only by a periodic modulation.*"[62]

This is a remark of the Swiss physicist Felix Bloch (1929) that highlights the difference between free electrons and those in a crystal. The wave function he found, known as a Bloch wave, is used to describe electrons in a periodic potential and can be written in the form of an exponential plane wave multiplied by a periodic function:

$$\psi_k(\boldsymbol{r}) = e^{i\boldsymbol{k}\cdot\boldsymbol{r}} u_k(\boldsymbol{r}), \tag{5.4}$$

where $\boldsymbol{r}$ is position and $u_k(\boldsymbol{r})$ is the periodic function with the same periodicity as the crystal lattice.

Unlike a particle in a constant potential where its momentum is conserved, for a particle in a periodic potential the momentum is no longer well-defined. The parameter $\boldsymbol{k}$, called quasi-momentum (or crystal momentum), is a vector that behaves similarly to the momentum and is conserved. Due to the periodic potential, the quasi-momentum is also periodic. Therefore, we only need to pay attention to the first Brillouin zone, which is sufficient to describe all of the Bloch states without redundancy.

In 1883 a French mathematician, Gaston Floquet, already derived a form of solution for periodic differential equations.[63] Bloch theorem is just an implementation of that solution in the condensed matter setting. The Floquet theorem has found widespread relevance for the study of periodically-driven quantum systems. Such systems are described by a time-periodic Hamiltonian $H(t) = H(t + T)$, where T is the oscillation period. The corresponding time-dependent Shrödinger equation allows solutions of a specific form similar to the Bloch waves:

$$\Psi_\alpha(t) = e^{-i\varepsilon_\alpha t/\hbar}\, \Phi_\alpha(t). \tag{5.5}$$

These are the Floquet states, in which $\Phi_\alpha(t)$ is the Floquet mode and has the same periodicity as the Hamiltonian. Instead of quasi-momentum, the Floquet states are labelled with quasi-energy ε_α. One can easily see how the time periodicity here replaces the spatial periodicity in Bloch's theorem. This is why the Floquet theorem is often referred to as the counterpart of Bloch's theorem in time.

Using the Floquet ansatz (Eq.5.5) one can reduce time-dependent Schrödinger equations to an effective time-independent problem, but in an enlarged Hilbert space. The resulting number of distinct solutions depends on the dimension of the original Hilbert space. The extra set of solutions com-

ing from the enlarged Hilbert space does not give any additional information and describes the same physical states. Just as in solid state physics we focus only on the first Brillouin zone, there is a "Floquet-Brillouin zone" for the quasi-energy $\varepsilon_0 < \varepsilon < \varepsilon_0 + \hbar\omega_0$, in which all the physics of the time-periodic system is captured. Here, $\omega_0 = 2\pi/T$ is the frequency associated with the periodic driving.

5.4 Formation of Floquet Ladders

Now let us go back to our quartet system. Recall that in the simple dot model for a three-terminal Josephson junction the coupling between the electron and hole states is

$$\Gamma = \gamma_0 e^{i\varphi_0} + \gamma_1 e^{i\varphi_1} + \gamma_2 e^{i\varphi_2}. \tag{5.6}$$

With finite $V = V_1 = -V_2$, this coupling is modified to be

$$\Gamma = \gamma_0 e^{i\varphi_0} + \gamma_1 e^{i\varphi_1} e^{i\omega_0 t} + \gamma_2 e^{i\varphi_2} e^{-i\omega_0 t}, \tag{5.7}$$

where $\omega_0 = 2eV/\hbar$ is the Josephson frequency.

Since the original Hilbert space is two-dimensional and the wavefunction $\Psi(t)$ is represented by a two-component spinor $(\Psi_e(t), \Psi_h(t))$, by applying the Floquet theorem we get two quasi-energies and their replicas translated by $n\hbar\omega_0$, where n is an integer. This replicated spectrum is referred to

as a set of ladders. Same as in the previous section, we will not go into the detailed equations now. Interested readers can find the Floquet dot model in Appendix C. In the following subsections, we will build up these Floquet ladders with a classical approximation first, and then consider the quantum mechanics. Note that the Floquet ladders, Floquet levels, and Floquet spectrum will be used interchangeably. Usually "levels" are used when we talk about the two rungs of the ladders in the first Floquet-Brillouin zone, and "spectrum" is used when we talk about the Floquet energy as a function all parameters $(\widetilde{\varphi}_q, V, \Phi)$.

5.4.1 Classical ladders

Figure 5.4 (a) shows that in the $V = 0^+$ limit, one can average over the the running phase to obtain the effective time-independent Andreev bound states $\langle E_{ABS} \rangle$. This was discussed in Chapter 4. Once V is switched on, the Hamiltonian becomes time-periodic. By applying the Floquet theorem, the pair of effective Andreev levels emanates into infinite replica, forming two ladders as depicted in figure 5.4 (b).

While the energies are 2π periodic in the phases of the superconducting leads φ_1, φ_2, they are 4π periodic in the running phase $\varphi_r = \varphi_1 - \varphi_2$ (Eq.4.22). Therefore, the driving frequency of the system is the same as the Josephson frequency

$$\omega_0 = 2eV/\hbar. \tag{5.8}$$

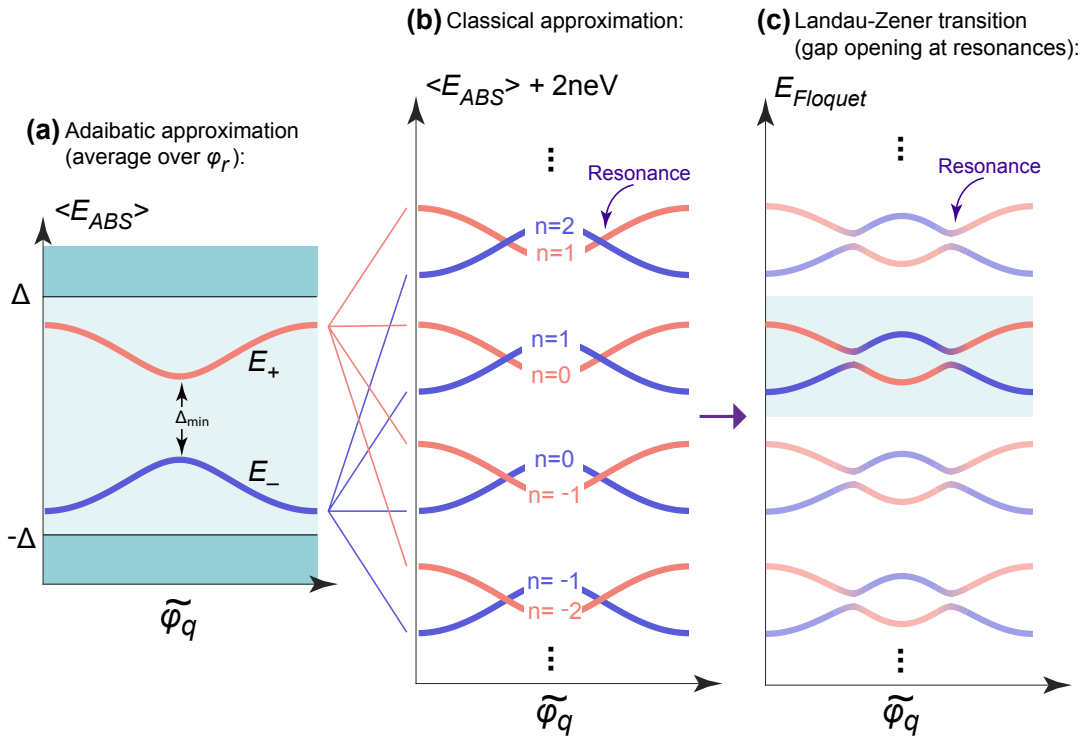

Figure 5.4: Formation of the Floquet ladders. (a) The adiabatic approximation gives us the effective Andreev bound states $\langle E_{ABS} \rangle$ by averaging over the running phase φ_r. (b) As V enters the finite regime, the pair of effective ABS, E_+ and E_- will emanate into infinite replica due to the time-periodic driving induced by the running phase φ_r. The driving frequency is $\omega_0 = 2eV/\hbar$ and the spacing between the rungs in each ladder is $\hbar\omega_0 = 2eV$. In the first Floquet-Brillouin zone, the classical ladders have level crossings when $V = E/en$. (c) Landau-Zener transitions between the original Andreev levels are triggered by the driving, opening Floquet gaps at resonances. The final form of Floquet ladders is completed.

The spacing between the rungs is given by

$$\Delta E = \hbar\omega_0 = 2eV, \tag{5.9}$$

which is tunable by the control voltage V (indeed, V determines how fast the system is running along φ_r). Figure 5.4 (b) shows the two unperturbed ladders (blue and red) from the classical approximation.

5.4.2 Landau-Zener tunneling at resonances

These classical ladders have level crossings at (consider the first Floquet-Brillouin zone only):

$$E_+ = E_- + 2neV, \quad \text{where } n \in \mathbb{N} \tag{5.10}$$

$E_{+,-}$ denote the upper and lower effective Andreev bound states and since $E_+ = -E_- \equiv E$, the resonant condition is found to be:

$$V = \frac{E}{en} \tag{5.11}$$

Due to quantum correlations and the Landau-Zener transitions between the two levels discussed in the Section 5.1, the crossings turn into avoided-crossings. The gap opening at the resonances results in the final form of the Floquet ladders, as illustrated in figure 5.4 (c).

As we emphasized earlier, the infinite number of rungs arise from the translational symmetry in time just as the repeated Brillouin zones arise from the translational symmetry in space. Therefore, despite the infinite number of the energy levels, the reciprocated energies can all be reduced into the first Floquet-Brillouin zone, where our interest lies.

5.4.3 Construction of three-dimensional Floquet spectrum

We have explained the formation of Floquet ladders for a fixed value of control voltage V, which determines the distance between the rungs. One can imagine that when V is changing, we have these ladders extended in another dimension as the spacing between the rungs is altered. If figure 5.4 (b) is the "front view" (as a function of quartet phase) of the classical ladders, then the "sideview" (as a function of V) is shown in figure 5.5. Because of the resonant condition (Eq.5.11), one can see clearly the linear periodic resonances when the Floquet energies are plotted as a function of $1/V$, as shown in the bottom panel of figure 5.5.

Let us not forget that in our device we have an additional parameter, the flux Φ threaded through the loop. As we discussed at the end of the previous chapter, varying the flux Φ results in a modification of the effective Andreev bound states, which are the building blocks of our Floquet ladders. Therefore, when we apply a different magnetic field, a new set of Floquet manifolds will be generated.

With all the tuning parameters in the quartet mode when it is set out-of-equilibrium, we possess a three-dimensional Floquet spectrum $E_{Floquet}(\widetilde{\varphi}_q, V, \Phi)$ that can be dynamically controlled. In the next section, we will demonstrate how the Floquet spectrum can be experimentally probed.

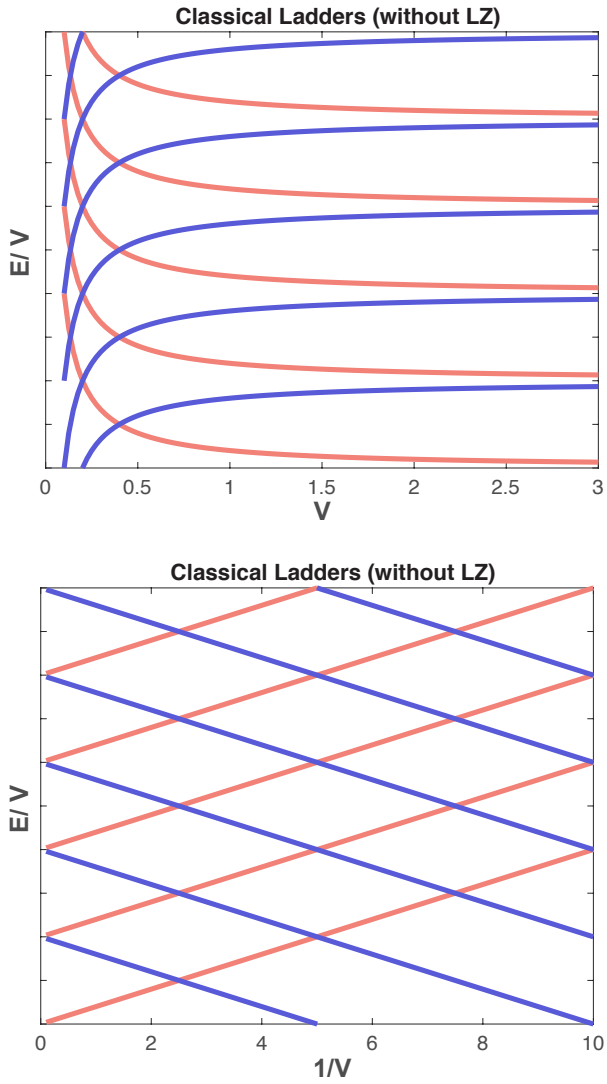

Figure 5.5: Calculated classical Floquet ladders along V when the quartet phase $\widetilde{\varphi}_q$ is chosen to be 1.1π (without the consideration of Landau-Zener (LZ) transition). Blue and red denote that the origins of the replica are the lower (E_-) and upper (E_+) effective Andreev levels, respectively. The crossing points are where the resonances are. Top: as a function of V. Bottom: as a function of $1/V$.

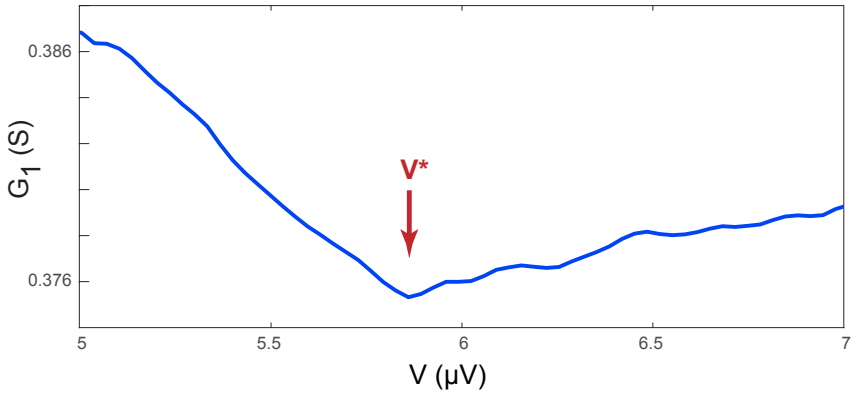

Figure 5.6: Measured quartet conductance G_1 as a function of the control voltage V, which is proportional to $I_{qc}(V)$. A local minimum at V^* is observed and is crucial for the probing of the Floquet spectrum.

5.5 Probing the Floquet Spectrum

In our experiment, we have two knobs that can directly tune the Floquet spectrum. The first is the bias voltage V, which controls the driving frequency and hence the spacing between the rungs in the Floquet ladders. The second is the flux Φ threaded through the device loop. It changes the effective loop coupling $\gamma_0'(\Phi)$ and hence the effective Andreev bound states, which are the building blocks of the Floquet ladders.

5.5.1 Evolution of Floquet levels along V

Figure 5.6 shows the quartet conductance $G_1 (= dI_1/dV_{AC})$ we measure in experiment, as a function of the control voltage V. A local minimum around $V = 5.8\ \mu$V is observed. This dip is crucial in

probing the Floquet spectrum since it indicates where an avoided crossing is. In this subsection we will lay out the connection between the Floquet spectrum in theory and the experimental measurement.

Figure 5.7 (a) shows how the Floquet levels as a function of $\widetilde{\varphi}_q$ evolve as the voltage V is tuned and (b) shows the corresponding calculated quartet current I_q. $\widetilde{\varphi}_q^*$ is where I_q has its maximum value, i.e., the quartet critical current I_{qc}. The color code blue and red represent populated and empty levels, respectively. Note that the levels originate from the two effective Andreev levels that carry supercurrents of opposite directions. Four regions of V are discussed:

(I) When $2eV$ is smaller than the Andreev gap Δ_{min}, there is no coupling between the two levels and the quartet current is the same as that near equilibrium.

(II) As $2eV$ exceeds Δ_{min}, Floquet gaps open near resonances. The hybridization between the levels and mixing of states result in a drop in the net current, which further affect the value of $\widetilde{\varphi}_q^*$ and I_{qc}.

(III) With even larger voltage $V = V^*$, the resonances take place at the original $\widetilde{\varphi}_q^*$, denting the peak in I_q. The quartet critical current I_{qc} thereby reaches a minimum.

(IV) When $2eV$ is increased to be greater than the largest gap between the two levels, there is no more hybridization. Both the levels and the current recover to the case near equilibrium. In this stage, the two levels may look like the Andreev bound states in a ferromagnetic Josephson π-junction. But remember only two rungs of the ladders are shown in the figure. The full set of ladders is composed of infinite rungs and therefore stage (IV) is actually the same as stage (I); it is not a π-junction.

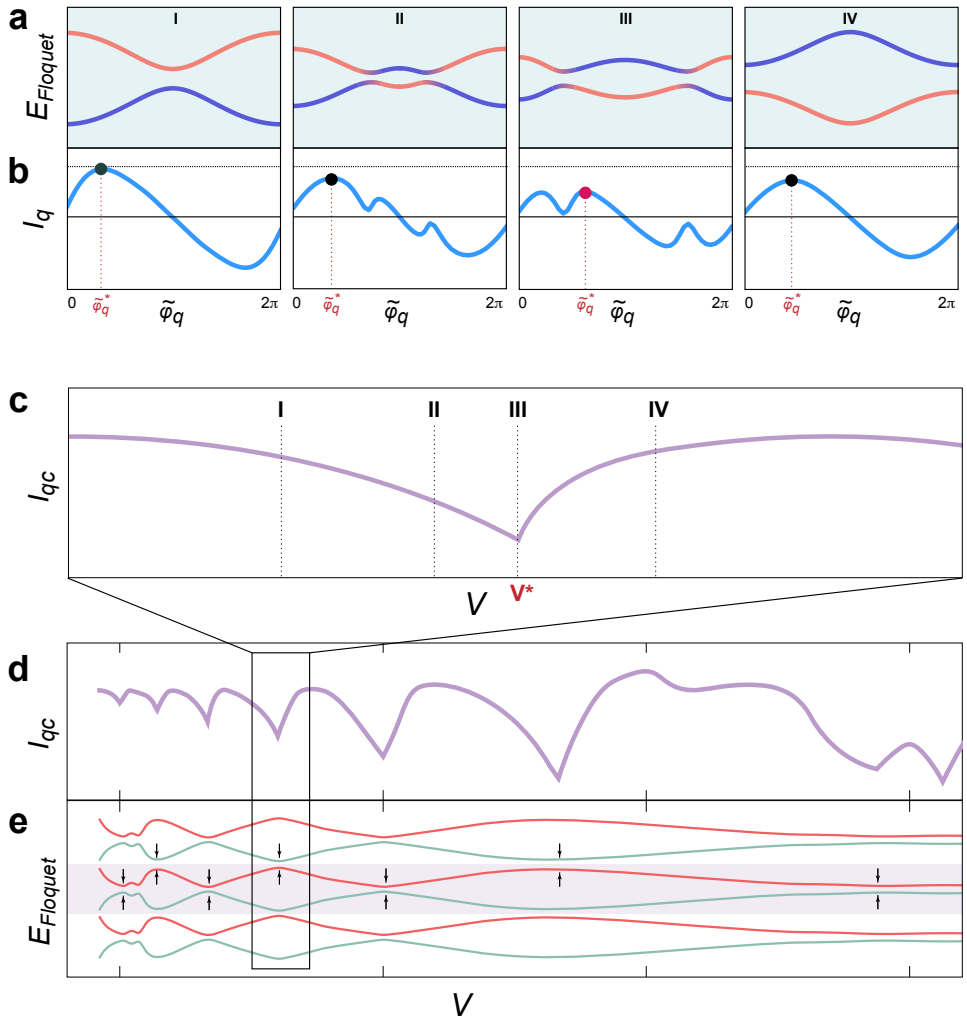

Figure 5.7: (a)(b) Evolution of the Floquet levels and quartet current as functions of $\widetilde{\varphi}_q$ at different values of V. I: When V is small such that $2eV < \Delta_{min}$, the two levels are not yet coupled. The lower level is fully occupied (blue) while the upper level is empty (red). The maximum quartet critical current occurs at $\widetilde{\varphi}_q = \widetilde{\varphi}_q^*$. II: When $2eV$ exceeds the Andreev gap Δ_{min}, the two levels start to hybridize. Due to Landau-Zener transitions, gaps open at the level crossings. At these avoided crossings, both hybridized levels are populated (blue-red gradient). Since the upper and lower levels carry quartet supercurrents of opposite directions, the mixing of states causes strong modulation of the quartet current-phase relation, resulting in the shift of $\widetilde{\varphi}_q^*$ and decrease in I_{qc}. III: As V is increased to V^*, the modulation of $I_q(\widetilde{\varphi}_q)$ is even stronger and I_{qc} reaches a minimum. IV: When $2eV$ is greater than the largest gap between the two levels, there is no longer resonant coupling and the near equilibrium situation is resumed. (c) The quartet critical current I_{qc} has a local minimum at V^*. (d) I_{qc} in a large range of V can have multiple minima. (e) The minima of I_{qc} in (d) correspond to the avoided crossings (indicated by the black arrows) in the Floquet ladders along V.

By collecting the maximum values of the quartet current at each V, one can see how the quartet critical current I_{qc} changes as a function of V in figure 5.7 (c). In fact, in a large range of V, there can be multiple minima in I_{qc}, as shown in (d). Figure 5.7 (e) shows the Floquet ladders plotted as a function of V. The avoided crossings (indicated by the black arrows) in the ladders correspond to the dips in I_{qc}. Therefore, the observation of a local minimum in the quartet conductance measured as a function of V (figure 5.6) not only shows where an avoided crossing in the Floquet spectrum is, its vicinity also reflects the evolution of the ladders.

5.5.2 Flux dependence of the Floquet spectrum

What we see in figure 5.6 and figure 5.7 is only an avoided crossing and the ladder evolution along V at a specific value of flux. Now let us tune this second knob, Φ. Figure 5.8 demonstrates that as the flux is varied, the position of the avoided crossing (V^*) shifts accordingly. After Φ is changed by one flux quantum, V^* returns to the original value.

Figure 5.9 shows the 2D color plot of the measured quartet conductance G_1 as a function of V and magnetic field. While the zig-zag pattern illustrates how V^* shifts upon changing the flux, one can also look at this data from another perspective: how $G_1(\Phi)$, which is proportional to $I_{qc}(\Phi)$, evolves as a function of V.

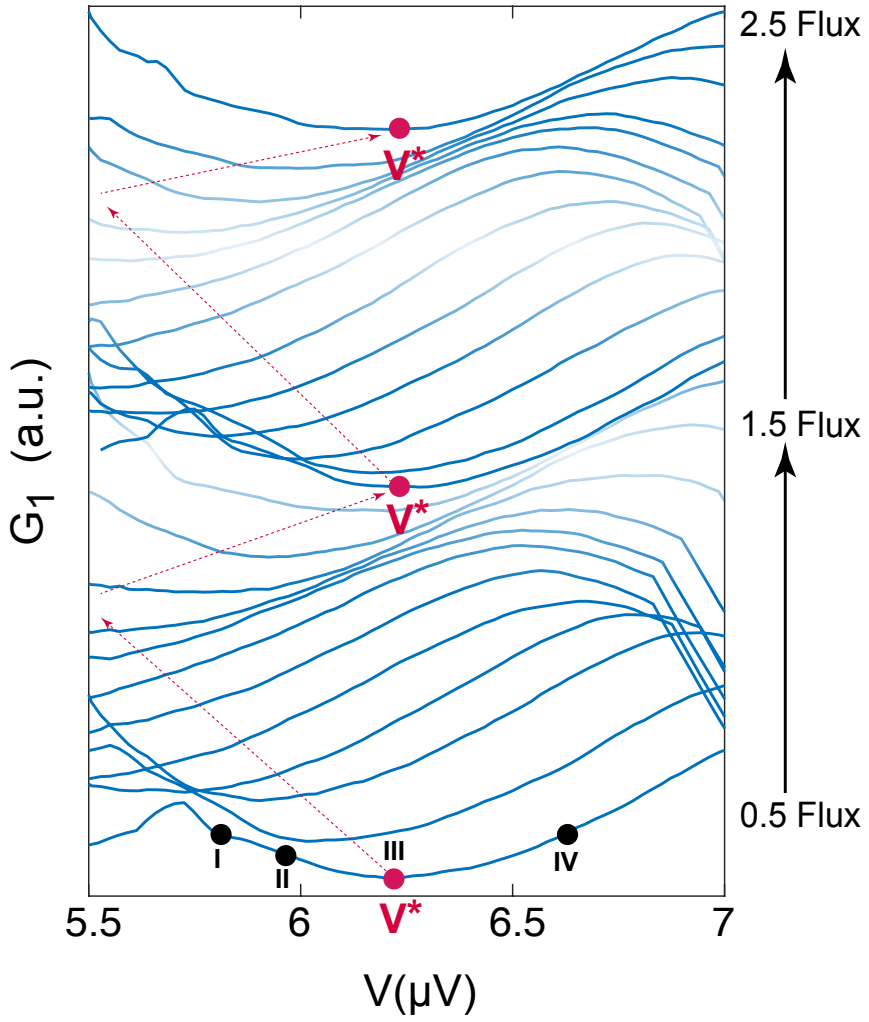

Figure 5.8: Quartet conductance as a function of V at different values of flux. The black and red dots labelled with I, II, III, IV correspond to the different architecture of the Floquet ladders as depicted in figure 5.7. The red dot V^*, where the avoided crossing in the Floquet spectrum is, shifts as the flux is varied. After increasing the flux by one flux quantum, V^* returns to its original position.

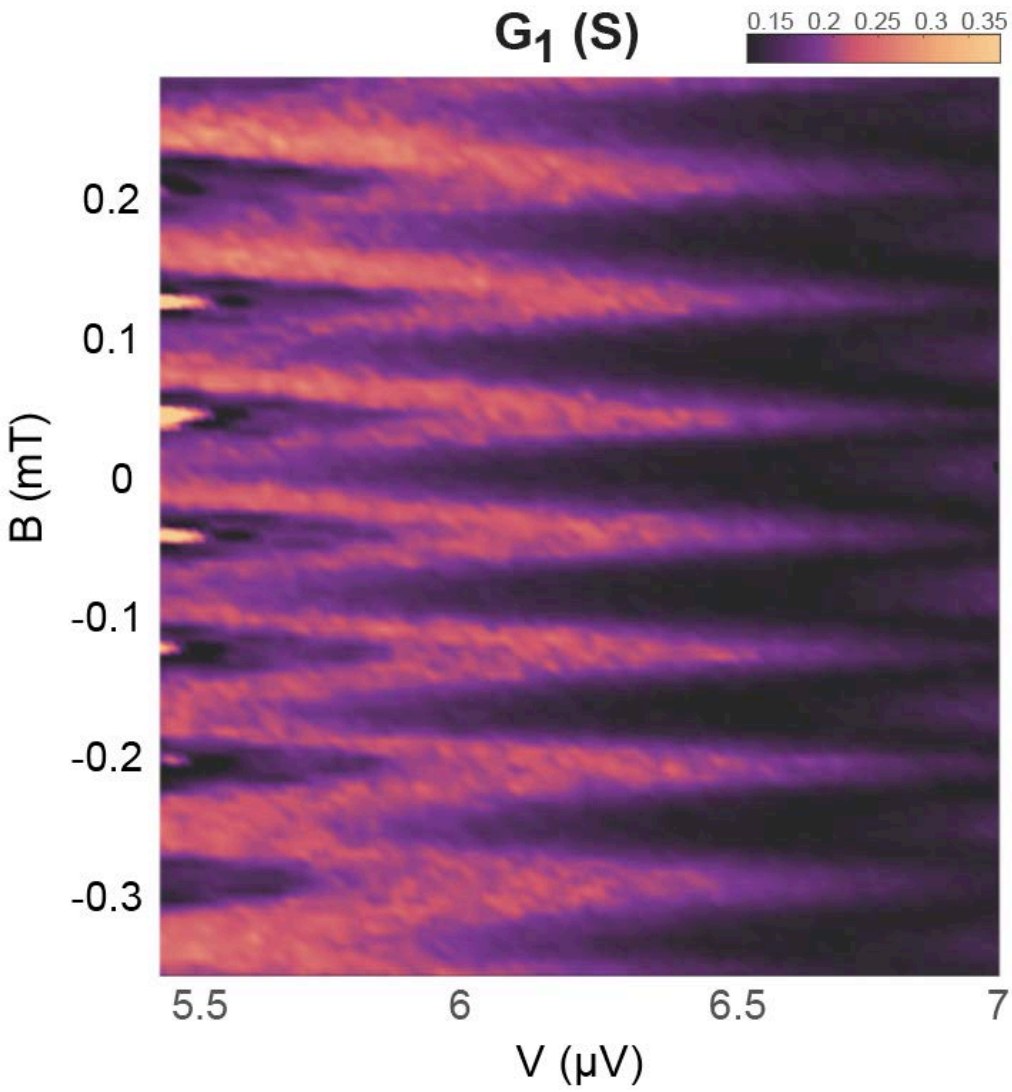

Figure 5.9: Color plot of quartet conductance as a function of V and magnetic field. The zig-zag pattern is due to the sifting of avoided crossing (V*) as the flux is varied, showing how the Floquet spectrum is tuned by the magnetic field.

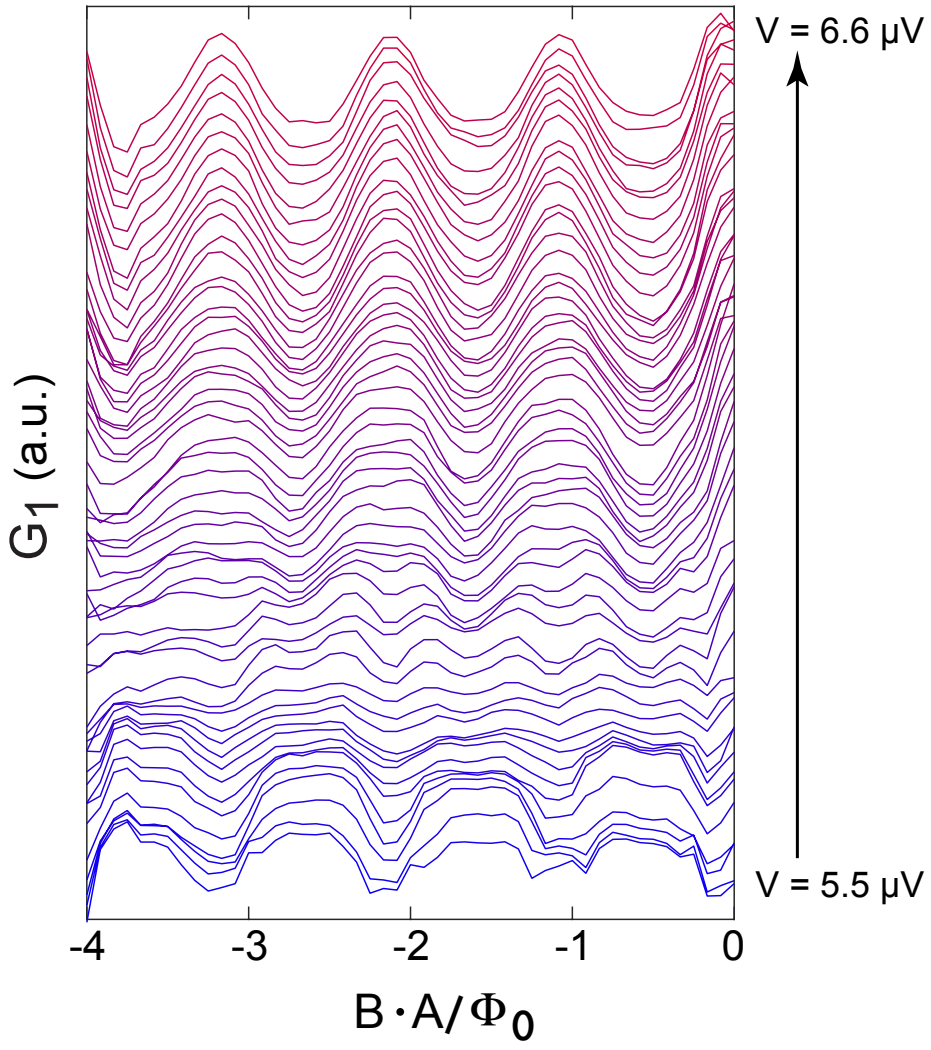

Figure 5.10: Quartet conductance as a function of flux at different values of V, which is another perspective to understand how the Floquet spectrum can be modulated. When the bias voltage V is around 5.5 μV, the conductance have minima at zero and integer values of flux. As V increases, these minima gradually evolve into maxima, suggesting the system at zero flux is moving away from an avoided crossing.

This perspective is shown by vertical linecuts of the 2D plot, as plotted in figure 5.10. Starting from the bottom of the figure, when V is around 5.5 μV, there is conductance minima at zero and integer values of flux. As V increases, the driving frequency increases and these minima gradually develop into maxima. In between, they go through a stage in which there is the second harmonic in the quartet conductance. This is similar to in the adiabatic limit we discussed in Section 4.5; the Floquet quartet process can also be modulated by V via controlling the interference between split quartets and conventional quartets.

In conclusion, under the specific voltage configuration $V_1 = -V_2 = V$, the quartet Andreev bound states is created. As V is increased above the 0^+ limit, the running phase φ_r serves as an intrinsic driving field that is time-periodic. In the framework of Floquet theory, we show how the three-dimensional Floquet spectrum is established as a function of the quartet phase $\widetilde{\varphi}_q$, the control voltage V and the flux Φ threaded through the device loop. More importantly, this Floquet spectrum can be experimentally probed and modulated via V and Φ. In the last section, we will discuss how this type of device provides a potential platform for engineering an Andreev spectrum that may exhibit exotic topological states.

5.6 Outlook: A Platform for Exploring Topology

As mentioned earlier, multi-terminal Josephson junctions have gained growing attention in recent years. This attention is tied to the quest for topological quantum phases and the fact that materi-

als with intrinsic topological properties are rare in nature. So far, much of the progress in the search for topological materials has relied on combining different materials in order to obtain the required band structure and the quality of these crystals is demanding. Therefore, alternative routes have been proposed to create artificial topological materials, even in non-electronic systems such as in ultra-cold atoms. Recently, several theoretical studies have shown that in superconducting systems the three-dimensional Andreev bound states can host Weyl nodes,[31,32,33,34,35,36] analogous to those in a Weyl semimetal.[64] This opens up a new realm of study for artificial topological materials.

In this section, the parallel between band theory and superconductivity is addressed followed by several examples of how we may explore the topology of Andreev bound states in future experiments with multi-terminal Josephson junctions.

5.6.1 Superconductivity and band theory

One can draw an analogy between superconductivity and band theory. Figure 5.11 shows the band structure of a 2D graphene in the tight-binding model and the ABS spectrum of a three-terminal Josephson junction; there is a striking similarity with the crystal momenta k_x, k_y corresponding to the superconducting phases φ_1, φ_2. This can be generalized to an n-terminal Josephson junction with $(n-1)$ independent superconducting phases. The junction energy spectrum is thus in $(n-1)$ dimensions. As these 2π-periodic superconducting phases play the role of crystal momenta, the ABS spectrum becomes the analogue of the electronic dispersion of a crystal with $(n-1)$ dimensions. In other words, one can create an artificial crystal with arbitrary dimensions, depending on the number

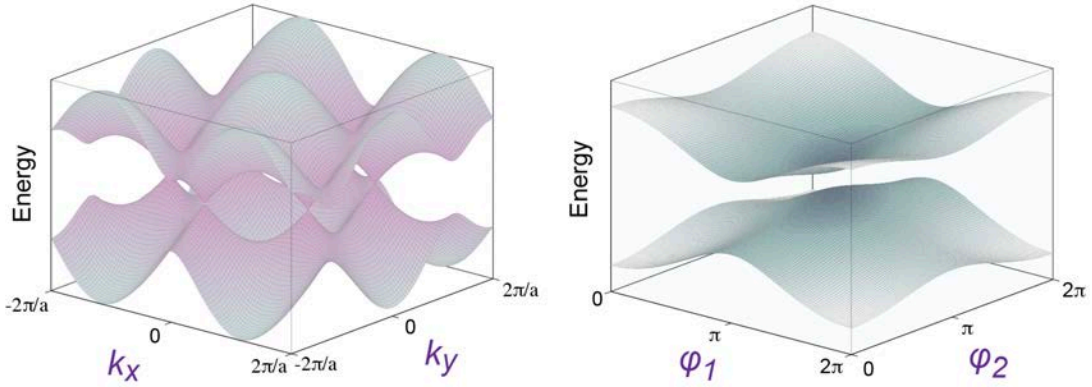

Figure 5.11: The band structure of a 2D material, e.g.graphene (left) and Andreev bound state spectrum of a three-terminal Josephson junction (right) are the analogues of each other with the crystal momenta k_i and superconducting phases φ_i are playing the same role.

of superconducting leads in the device. A more detailed parallel between band theory and superconductivity is in Table 5.1. [65]

5.6.2 Weyl nodes in three-dimensional ABS spectrum

In Chapter 2 we showed that Andreev bound states of a two-terminal Josephson junction can only have zero energy if the transmission coefficient is unity ($\tau = 1$) and at $\varphi = \pi$. Therefore, in practice there is always a finite gap in the spectrum. But the story is different for an n-terminal junction ($n > 2$). For example in a four-terminal Josephson junction or in our device (a three terminal junction with a loop) there are three independent phase variables. Depending on the details of the Josephson junction such as the scattering matrix in the normal region and the contact transparency to the superconducting leads, the ABS spectrum can be engineered to host zero-energy states, i.e., the Weyl singularities. With

Band theory	Superconductivity
n-dimensional crystal	(n+1)-terminal Josephson junction
$(2\pi/a)$-periodic wave-vector k_i	2π-periodic superconducting phase φ_i
position in real space (x_n)	number of Cooper pairs transmitted (N)
Hopping between neighboring sites	Transferring Cooper pairs between normal region and superconducting leads
Electric field $dk/dt = -eE$	Josephson relation $d\varphi/dt = 2eV/\hbar$

Table 5.1: Analogy between band theory and superconductivity.[65]

additional degree of freedom in the superconducting phases, one can sweep through the spectrum and tune the system to the topologically nontrivial phase.[32] In figure 5.12 we show that for a certain combination of the contact couplings γ's in the simple dot model (introduced in section 2.4.2), the gapped spectrum $E(\varphi_1, \varphi_2)$ can be tuned to a gapless one as the third phase φ_3 is adjusted.

The Chern number C_{12} of the ABS levels can be computed by integrating the Berry curvature B_{12} over the phases $\varphi_{1,2}$. As S_2 is biased with a very small voltage compared to the superconducting gap, $eV_2 \ll \Delta$, the current flowing into S_1 is

$$I_1(t) = \frac{2e}{\hbar}\frac{\partial E}{\partial \varphi_1} - 2e\,\frac{\partial \varphi_2}{\partial t}\,B_{12}\,, \quad \text{where} \frac{\partial \varphi_2}{\partial t} = \frac{2eV_2}{\hbar}. \tag{5.12}$$

The first term is just the adiabatic current, and the second term is the first-order correction in the phase velocity governed by the Berry curvature. When the two terminals S_1, S_2 are biased with incommensurate voltages V_1, V_2, the two phases sweep uniformly the effective Brillouin zone of the ABS spectrum. Therefore, the adiabatic current is averaged to zero and the Berry curvature is replaced

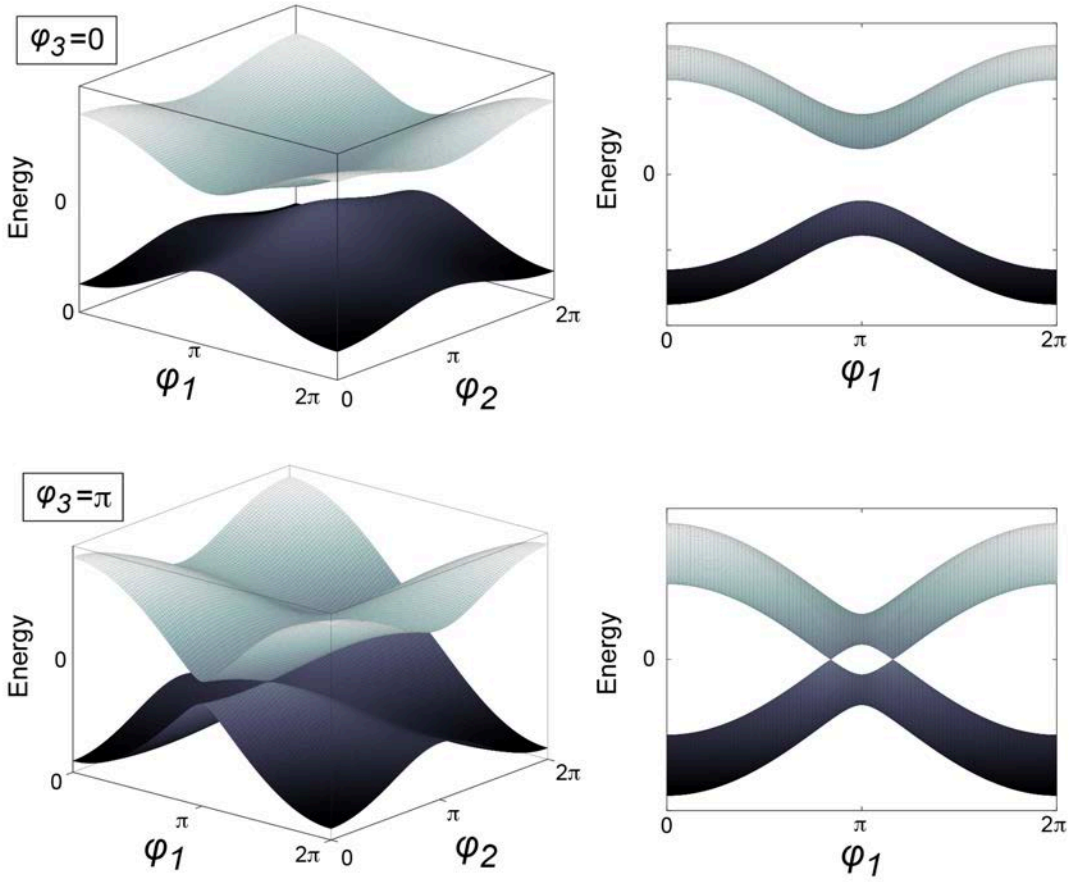

Figure 5.12: In a simple dot model for four-terminal Josephson junction, the gapped ABS spectrum at $\varphi_3 = 0$ becomes gapless at $\varphi_3 = \pi$ with a given set of contact couplings. The zero-energy states are the Weyl singularities, analogous to the Weyl nodes in the band structure of Weyl semimetals.

by its averaged value. The DC current becomes linear in the voltage

$$\bar{I}_1 = -\frac{4e^2 V_2}{\hbar} C_{12}. \tag{5.13}$$

Since I_1 and V_2 are connected through the transconductance G_{12}, it can then be defined by the Chern

number:[32]

$$G_{12} = -\frac{4e^2}{h} C_{12}. \tag{5.14}$$

Eq.5.14 suggests that the nonlocal transconductance is expected to be quantized in the topological regime in the presence of Weyl points. Experimentally an ABS spectrum with Weyl singularities may be realized through precise gate control at each superconducting contact so that fine tuning of γ's is possible. The challenge lies in the small subgap voltages required for the measurements. Nevertheless, a multi-terminal Josephson junction is another type of system that can host topological states and is more accessible since one does not need topologically-nontrivial materials.

5.6.3 Floquet topological insulators

In the quartet measurement, we are already out of the adiabatic regime. Therefore, to think beyond our current experiment, we may turn our attention to the topology of driven systems. It has been suggested that robust topological phenomena may be generated by dynamical engineering. For example, the Bloch bands in atomic or electronic systems can be manipulated with periodic driving.[66] By choosing the appropriate driving frequency and amplitude, topological phases can be induced in topologically trivial systems.[67,68,69] This band engineering is similar to the construction of Floquet ladders in our system as shown in figure 5.13: when the photon energy of the driving field exceeds the band gap, there is resonant coupling at certain crystal momentum between the valence band and

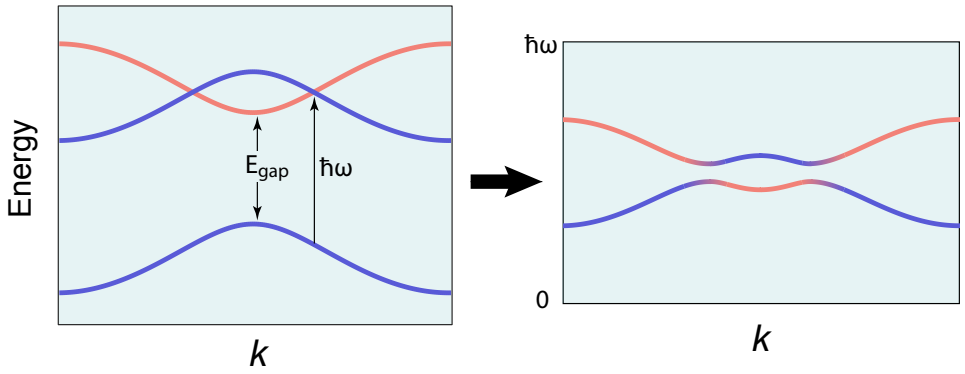

Figure 5.13: Left: in a solid, the valence band (blue) and conduction band (red) are resonantly coupled when the photon energy $\hbar\omega$ of the driving field exceeds the band gap. Right: gaps open at the resonances, forming the Floquet bands.

the conduction band. The driving field induces a Rabi-like splitting between the two bands, thereby opening a Floquet gap. The main challenge for progress in this direction is stabilizing a stationary state in such an non-equilibrium system. Recently, theoretical studies have investigated how to accomplish this task in the presence of a dissipative environment,[70] which is also encouraging for the realization of a Floquet topological state in biased multi-terminal Josephson junctions with more sophisticated device design and measurement.

A

Device Fabrication

In this appendix, the simple stamp preparation and the inverted stacking method that I used for all the devices in this thesis are described. Regarding the general transfer technique, the details and recipes can be found in the theses of my fellow lab mates who are the true masters of stacking.[71,72]

A.1 Stamp Preparation

The stamp we use is based on polypropylene carbonate (PPC), which has a glass transition temperature between 25 and 45°C. When PPC is heated to above 45°C, it begins to melt, becoming liquid-like. Typically, we contact the flake with PPC at 60°C and then cool down to 30°C to pick up the flake from the SiO_2 substrate.

The structure of the stamp used for transfer is shown in figure A.1. On a glass slide, we first put a cube of homemade polydimethylsiloxane (PDMS). The purpose is to create a moldable gel to support the PPC film. The 3M scotch tape is used to secure the PPC film on top of the gel and glass slide. The side view shows that the PPC film form a dome shape, which makes it easier to control the contact area between PPC and the substrate so that only the target flake would be picked up. The tape is also important for the inverted stacking technique, which is introduced in the next section.

A.2 Inverted Stacking

In the standard stacking technique, we pick up the flakes one by one starting from the top layer and the last step is to drop the stack onto the bottom layer. However, an ultra thin flake, monolayer hBN or MoS_2 for instance, is very difficult to be picked up by PPC. Even if the thin flake is picked up, it is difficult to align in the next step since it is transparent and almost invisible on PPC. Another scenario

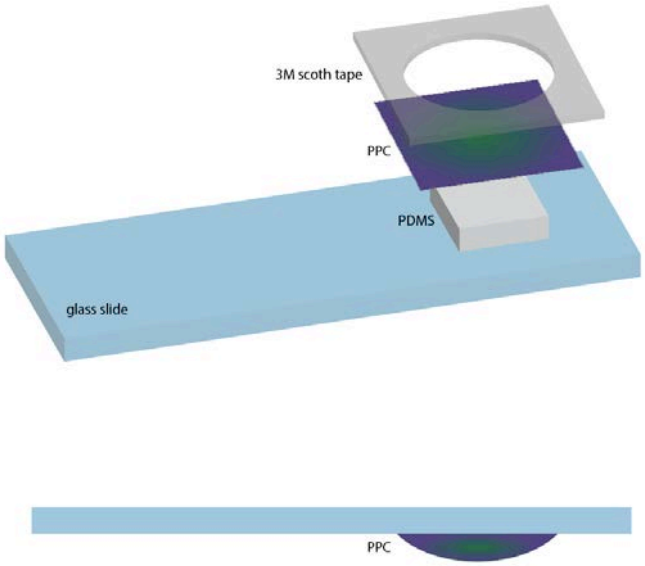

Figure A.1: PPC stamp. The PPC film forms a dome shape due to the PDMS underneath it, making it easy to pick up the target flake.

where the standard technique is not ideal is if we need a very clean top surface. This is why the devices in this thesis were all done with the so-called inverted stacking technique.

We start by picking up the bottom layer (thick hBN), then monolayer graphene, and (if needed) the top monolayer hBN/MoS_2. Afterwards come the key steps of inverted stacking are shown in figure A.2. (a)(b): with steady hands, we peel off the scotch tape from the glass slide along with the PPC film holding the van der Waals stack. (c): then we drop the PPC film on a new and clean SiO_2 substrate with the stack facing up. By heating the substrate slowly to 120°C, the PPC film will melt on the substrate and will easily detach from the scotch tape. (d): we will end up with the stack on the melting PPC on the substrate. The final step is to put the substrate into the vacuum chamber and anneal at 350°C for 15-20 minutes, which is sufficient to get rid of all the PPC. This leaves the stack sitting directly on the substate, with a clean top surface that has never been in contact with PPC.

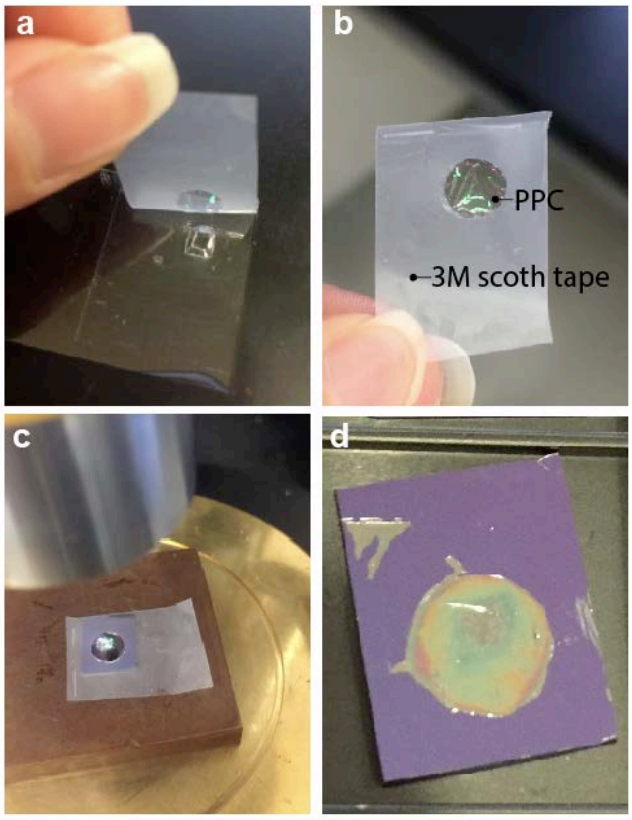

Figure A.2: Inverted stacking: (a)(b) peel off the PPC film along with the van der Waals stack from the glass slide using the 3M scotch tape. (c) put the PPC film down on a clean, new SiO_2 substrate and heat slowly to 120°C. (d) at 120°C, it is easy to detach the scotch tape from the melting PPC, leaving the stack on PPC on the substrate. The final step is to vacuum anneal the substrate.

B

Measurements

This appendix discusses the details of measurements in a three-terminal Josephson junction, including current bias/voltage bias method, as well as the circuit for quartet detection.

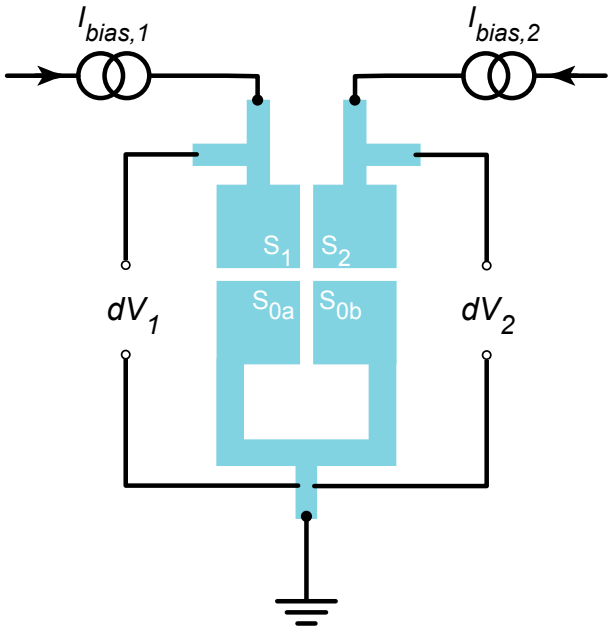

Figure B.1: Three-terminal Josephson junction measurement with the dual current source. The leads S_1, S_2 each are biased with a small AC excitation current dI=20 nA and a DC bias $I_{bias,i}$ (i = 1, 2) up to 3 μA while the loop S_0 is grounded. The differential voltage drop across the two junctions are measured: dV_1 for $S_1 - S_{0a}$ and dV_2 for $S_2 - S_{0b}$.

B.1 Current Bias Measurement in a Three-terminal Junction

In Chapter 4, we presented the quartet data with the dual voltage bias measurement. In this section, we discuss the data from the dual current source measurement and why voltage biasing is favored, even crucial for detecting the quartet. It is then followed by the details of the dual voltage source measurement we performed in the quartet experiment.

As shown in figure B.1, in the three-terminal Josephson junction the current bias method contains two current sources, each having a small AC excitation current dI=20 nA and a DC bias $I_{bias,i}$ (i =

1, 2) up to 3 μA. They are injected into the device from leads S_1 and S_2, respectively while the loop S_0 is grounded. The two lock-in amplifiers are set to non-commensurate frequencies at 87 Hz and 113 Hz in order to measure the differential voltages dV_1 between $S_1 - S_0$ and dV_2 between $S_2 - S_0$, respectively.

Figure B.2 shows the data acquired from the dual current source measurement. Left panel (a): the differential resistance dV_1/dI as a function of the two bias currents $I_{bias,1}$ and $I_{bias,2}$. One can see clearly that there are the usual Josephson currents flowing between any pair of contacts: (i) $S_0 - S_1$ (ii) $S_0 - S_2$ and (iii) $S_1 - S_2$. However, there is no sign of other supercurrent. In order to create the bound state for quartet, one needs to fix the potential of the three terminals to be $(V, -V, 0)$. Therefore, we need to convert the bias currents to bias voltages to locate where $V_{bias,1} = -V_{bias,2}$ is. In principle, with $dV/dI(I_{bias})$, one can obtain $dV/dI(V_{bias})$ via integration. However, we now have two current sources and the 2D integration is not trivial in this case. Instead, we use digital multimeters to measure directly the DC voltage drop across the junctions for $V_{bias,1}$ and $V_{bias,2}$. The differential resistance dV_1/dI is plotted as a function of the two DC bias voltages in figure B.2 (b). Despite the noise, the Josephson currents (i)(ii)(iii) can still be observed after the conversion. But there is no no hint of quartet current along $V_{bias,1} = -V_{bias,2}$. Since the quartet current is rather small compared to the Josephson current, it is extremely difficult to extract the quartet signal from such a voltage bias plot from a current bias measurement.

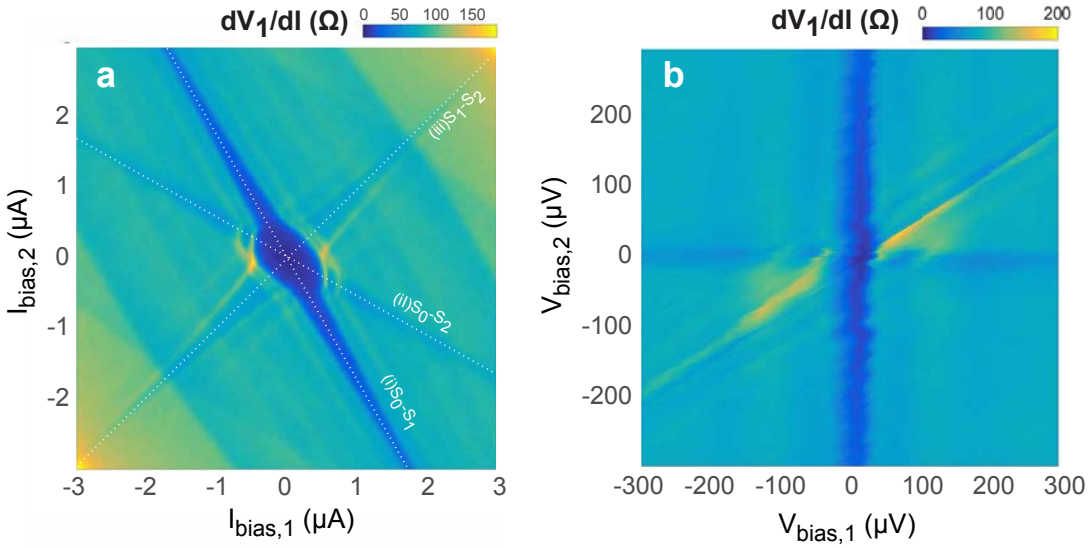

Figure B.2: Three-terminal Josephson junction measured with the dual current source method. a: differential resistance dV_1/dI as a function of the two bias currents. b: the two axes are bias voltages measured with digital multimeters.

B.2 Voltage Bias Measurement in a Three-terminal Junction

B.2.1 Voltage bias measurement for an ideal junction

Let us start with an ideal Josephson junction with $V - I$ curve that is shown in figure B.3. The red sinusoidal symbol represents the AC excitation dV.

1. Blue dots: when $V_{bias} = 0$, the radical change in current between $I = I_c$ and $I = -I_c$ can be detected, resulting in a value proportional to $2I_c$ in the measured dI/dV:

$$\left.\frac{dI}{dV}\right|_{V_{bias}=0} = \frac{\Delta I}{\Delta V} \propto 2 \cdot I_c. \tag{B.1}$$

2. Red dot: as V_{bias} is increased to a small positive value V_c but smaller than V_s, there is no variation in the current and hence $dI = 0$. This is the point that reflects where I_c is; therefore we call it V_c.

3. Purple dot: when V_{bias} is increased to the switching voltage V_s, there is a change in I because the junction is switching to its normal state, therefore dI/dV is no longer zero.

4. Green dots: finally, as V_{bias} is even larger than V_s, dI/dV shows the normal state conductance.

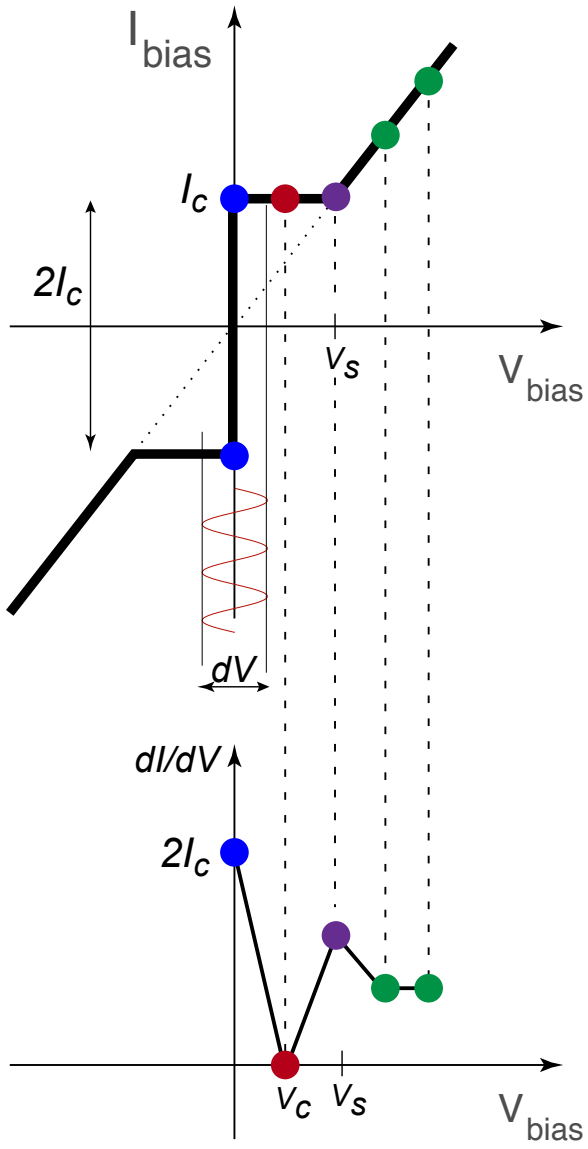

Figure B.3: Voltage bias measurement for an ideal Josephson junction. The red sinusoidal symbol represents the AC excitation dV. At zero bias (the blue dots), the radical change from $-I_c$ to I_c results in the measured dI/dV proportional to $2I_c$. At the red dot, there is no variation in current, corresponding to $dI/dV = 0$. With even larger bias (green dots), the value of dI/dV reflects the normal state conductance of the junction.

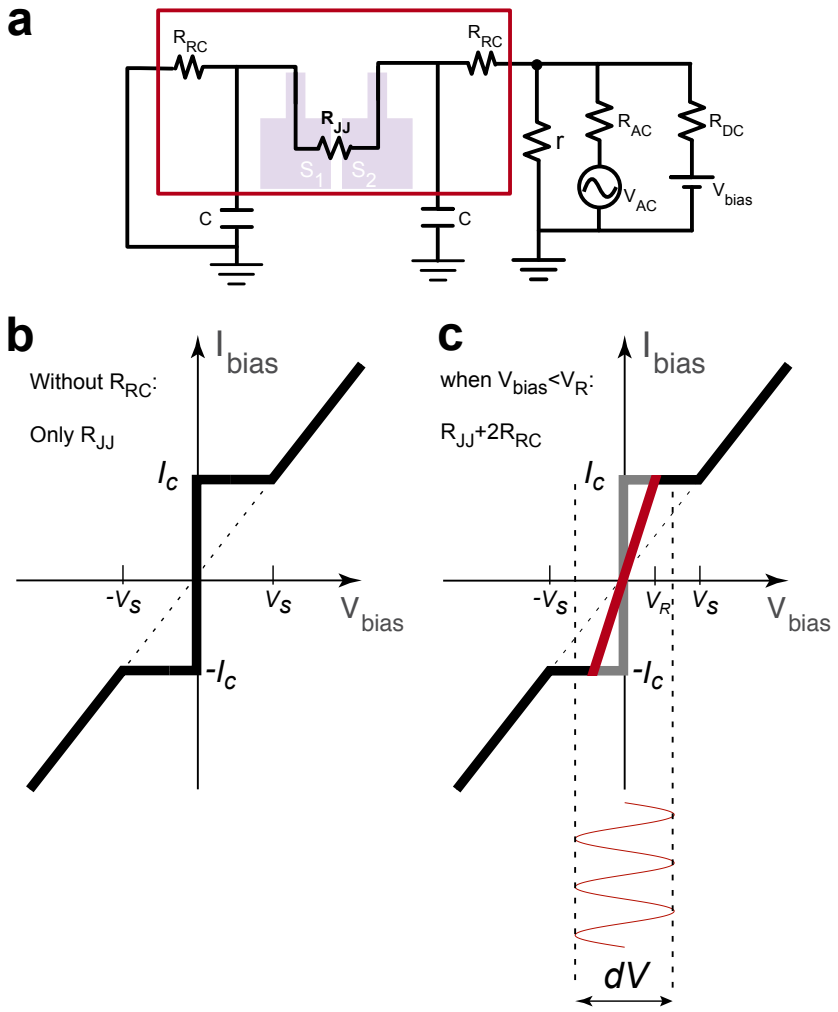

Figure B.4: (a) Two-terminal voltage bias circuit. (b) an ideal $V - I$ curve. (c) $V - I$ curve of the quartet junction in our circuit. The red sinusoidal symbol represents the AC excitation dV. As long as the excitation is chosen correctly, we are still able to detect the abrupt change at $I = I_c$ on top of the slope.

B.2.2 $V - I$ curve of the junction in quartet circuit

Let us consider a two-terminal Josephson junction for now and the voltage bias measurements scheme is shown in figure B.4 (a). This is also the circuit used for characterizing our three-terminal Josephson

junction (with one of the terminals floating). Due the resistance of RC filter, R_{RC}, we effectively have a junction (in the red box) with resistance

$$R_{JJ} + 2 \cdot R_{RC}, \tag{B.2}$$

where R_{JJ} is the Josephson junction resistance and $R_{JJ} = 0$ for $I < I_c$. Therefore, as opposed to the standard $V - I$ curve in figure B.4 (b), we have a slope when $V_{bias} < V_R$ as shown in figure B.4 (c). As long as the AC excitation (the red sinusoidal symbol)

$$dV > 2V_R = 2I_c \cdot 2R_{RC}, \tag{B.3}$$

we are able to detect the abrupt change at $I = I_c$ on top of the slope.

B.2.3 Comparison between current bias and voltage bias

In figure B.5, current bias (a)(b) and voltage bias (c)(d) measurements are compared. In the current bias measurement, as shown in subfigure (a), the red sinusoidal symbol represents the AC excitation dI. At zero current bias, one would not detect any variation in voltage, resulting in zero dV and hence zero dV/dI when $I_{bias} < I_c$. (In this example, due to some small wire resistance, dV/dI does not go to zero completely). As I_{bias} is increased to where I_c is, the AC excitation will detect the steep change in $I - V$ curve that corresponds to a sharp peak in dV/dI.

For the voltage bias case, the Josephson supercurrent is probed indirectly through the shape of

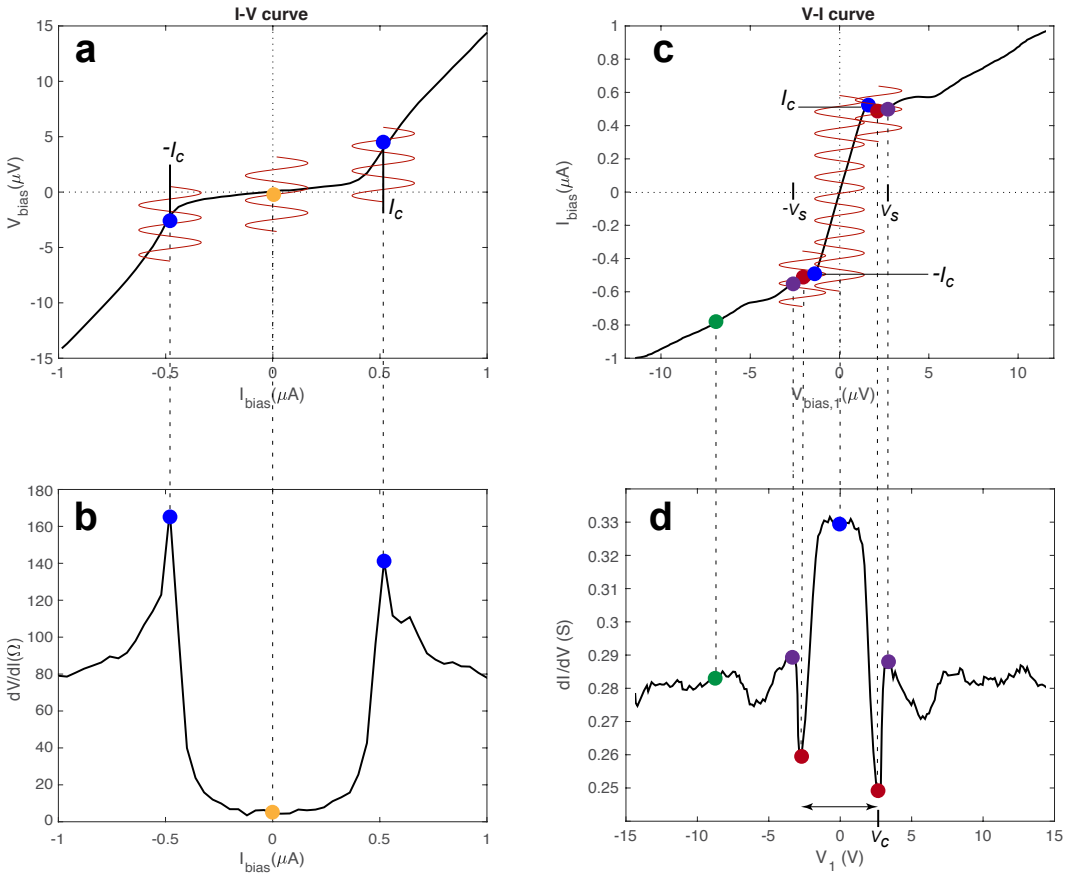

Figure B.5: Comparison between current (a)(b) and voltage (c)(d) bias measurement. The blue dots detect the variation at $I = I_c$ in both cases. In the voltage bias scheme, the red dots are before the junction becomes normal and can be considered as the detection of I_c. The purple dots are when the junction is when the junction just turns into normal.

the conductance, following the four points in V_{bias} we went through in the previous section. In the subfigure (c), the $V - I$ curve is shown, which is the same as in figure B.4 (c). Similar concept is implemented, where the red sinusoidal symbol represents the AC excitation dV. The difference from current bias is now even at zero voltage bias, the small AC excitation can sense the drastic change in $V - I$ curve at $I = I_c$ and $I = -I_c$. The corresponding differential conductance dI/dV, the blue

dot in subfigure (d), is proportional to $2I_c$ as discussed earlier.

In summary, the height of the conductance peak at zero voltage bias reflects the magnitude of the critical current I_c. The actual value of I_c can be deduced from the width of the peak; more precisely, the dip at V_c. Note that in the voltage bias scheme, the Josephson junction is current biased when $V_{bias} < V_c$. Once V_{bias} exceeds V_c, the junction will become truly voltage biased. We will have an explicit sample in the next section.

B.2.4 Voltage bias measurement for quartet detection

Figure B.6 is the circuit of the dual voltage source setup used for the detection of quartets. Understanding how the circuit works is non-trivial and therefore warrants a detailed explanation. To best describe how it works, we can decompose the circuit into four parts.

1. DC bias voltages at S_1 and S_2

The leads S_1 and S_2 are biased with DC voltages V_1 and V_2 through a voltage divider and an RC filter. In our measurements, V_i (i=1, 2) goes up to 15 V. The voltage divider divides the voltage by 10^4 and reduces the bias voltage to a maximum of 1.5 mV. This reduced voltage is then fed through two RC filters and the junctions of interest. Therefore, the actual voltage applied on each junction $S_0 - S_i$ is given by:

$$V_{bias,i} = V_i \cdot 10^{-4} \cdot \frac{R_{JJ}}{R_{JJ} + 2 \cdot R_{RC} + r}. \tag{B.4}$$

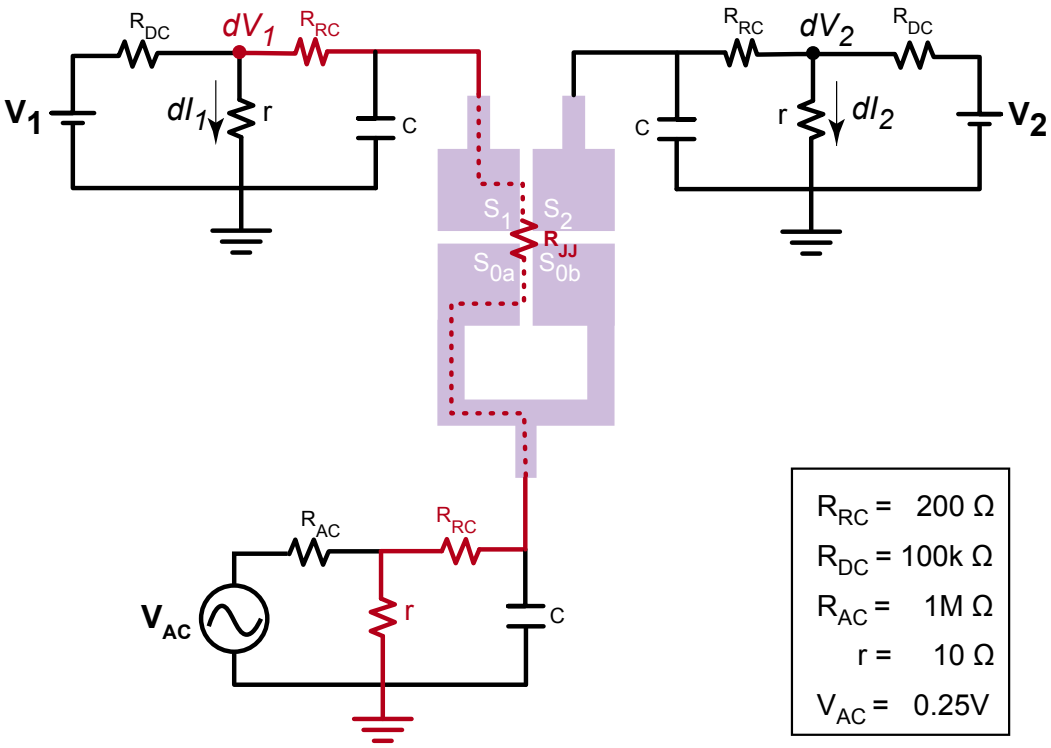

Figure B.6: $R_{DC/AC}$ and r are the components of voltage divider for the DC/AC bias voltages. R_{RC} is the resistance of the RC filter. The red path goes from potential dV_1 to the ground, and along the way there are four resistances: R_{RC}, R_{JJ}, R_{RC}, and r.

2. AC excitation applied to the loop

The loop of the device remains grounded at all times but on top of this DC ground, we apply a small AC excitation (V_{AC}) in the range of 0.25-0.3 V. Like the other leads, this lead also has a voltage divider followed by an RC filter. The voltage divider for the loop divides the AC excitation by 10^5 (not 10^4) and we denote the actual excitation for the junction to be

$$dV = V_{AC} \cdot 10^{-5} \cdot \frac{R_{JJ}}{R_{JJ} + 2 \cdot R_{RC} + r}. \tag{B.5}$$

3. AC current flowing from S_1 and S_2

In order to detect the quartet current, we measure the conductance at the biased leads S_1 and S_2. As shown in the circuit, we use lock-in amplifier to measure the potential dV_1 and dV_2. The AC currents flowing from S_1 and S_2 are then given by

$$dI_i = dV_i/r, \quad \text{where } i = 1, 2. \tag{B.6}$$

Therefore, the conductance at each lead is

$$dI_i/dV = dV_i/(r \cdot dV), \tag{B.7}$$

where r is chosen to be 10 Ω in the experiment and dV is the actual AC excitation applied on the junction given in Eq.B.5.

4. Actual DC voltage applied on the junction

To estimate the actual DC voltage applied on the junction, let us take a look at an example when V_2= 15 V, which is sufficient to switch S_2 from superconducting state to normal state. We then measure dV_1 from the lock-in amplifier as a function of DC bias V_1, as shown in figure B.7. The peak near zero bias is the signal from Josephson current between S_0 and S_1. As explained in the previous section, the red dot (V_c=1.95 V) can be used to calculate I_c and the purple dot (V_s =2.85 V) is where the normal state is switched on.

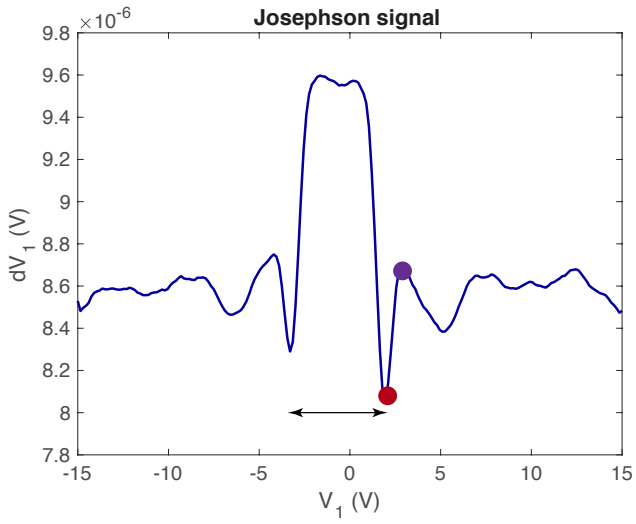

Figure B.7: The measured voltage dV_1 as a function of V_1 taken at V_2= 15 V. The peak near zero bias comes from the Josephson signal between S_1 and S_0. The red dot is at V_c=1.95 V and the purple dot is at V_s = 2.85 V.

Based on the bias regime, we can estimate the actual applied voltage in two ways. When we are outside of the supercurrent regime (for example, at V_1=15 V), our junction becomes normal and the normal resistance $R_{JJ}(I > I_c)$ is around 80 Ω, based on the current bias measurement. Then the actual DC voltage applied on the junction is (Eq.B.4):

$$\begin{aligned} V_{bias,1} &= V_1 \cdot 10^{-4} \cdot \frac{R_{JJ}}{R_{JJ} + 2 \cdot R_{RC} + r} \\ &= 15 \cdot 10^{-4} \cdot \frac{80}{80 + 400 + 10} = 250\ \mu\text{V}. \end{aligned} \tag{B.8}$$

And the voltage V_s (the purple dot) = 2.85 V converts to $V_{s,\text{junction}}$=46 μV, which is comparable to the value one finds in the current bias measurement.

The other regime is where $V_{bias} < V_c$ and R_{JJ} becomes zero. For the junction there is an AC

current defined as

$$I_{AC} = \frac{dV}{R_{\text{total}}} = \frac{dV}{2 \cdot R_{RC} + r} \tag{B.9}$$

$$= \frac{3\ \mu\text{V}}{2 \cdot 200 + 10} \approx 7\ \text{nA}, \tag{B.10}$$

and a DC current defined as

$$I_{DC} = \frac{V_1}{R_{\text{total}}} = \frac{dV}{2 \cdot R_{RC} + r} \tag{B.11}$$

$$= \frac{V_1}{2 \cdot 200 + 10}. \tag{B.12}$$

This effectively is the same as the current bias measurement scheme. So we can estimate our critical current from V_c (the red dot):

$$I_c = V_c \cdot 10^{-4}/(2 \cdot R_{RC} + r) \tag{B.13}$$

$$= 1.95 \cdot 10^{-4}/410 = 0.47\ \mu\text{A},$$

which is also consistent with the current bias data.

Another way to estimate the voltage applied on the junction is through calculation from the circuit. The conductance measured at S_1 is:

$$dI_1/dV = dV_1/(r \cdot dV) = dV_1/(r \cdot V_{AC} \cdot 10^{-5} \cdot \frac{R_{JJ}}{R_{JJ} + 2 \cdot R_{RC} + r}). \tag{B.14}$$

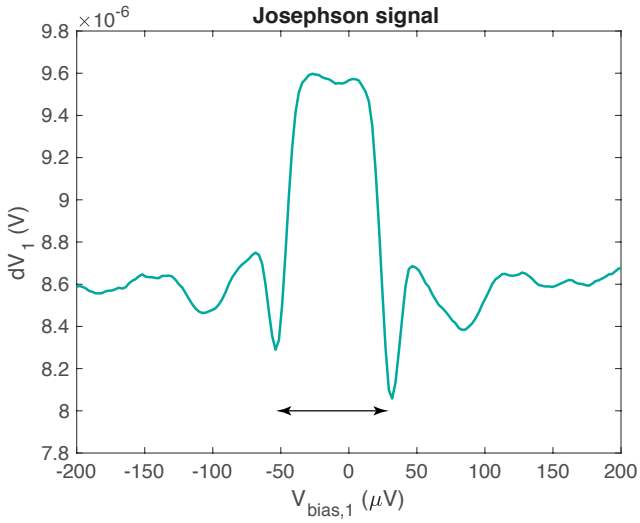

Figure B.8: After conversion, the Josephson signal is plotted as a function of the voltage applied on the junction $V_{bias,1}$.

One can then obtain R_{JJ} since R_{JJ} is the inverse of dI_1/dV. By plugging R_{JJ} into Eq.B.4

$$V_{bias,1} = V_1 \cdot 10^{-4} \cdot \frac{R_{JJ}}{R_{JJ} + 2 \cdot R_{RC} + r} \ ,$$

we can estimate the actual voltage applied across the junction. Figure B.8 shows the Josephson signal after conversion, as a function of $V_{bias,1}$. In the next section we will discuss how to read our quartet signal from the Josephson perspective in the voltage bias measurement.

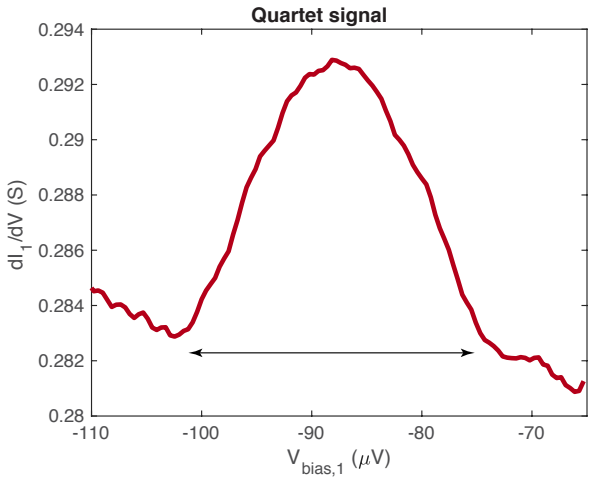

Figure B.9: The quartet signal as a function of $V_{bias,1}$. The width is about 28 μV, which corresponds to a quartet critical current $I_{qc} \sim 8.4$ nA.

B.3 Quartet supercurrent

In our experiment, based on a generalization of the RSJ model, the quartet current (non-equilibrium) can be mapped onto a standard Josephson current (near equilibrium).[40] Therefore, the width of the quartet signal measures the order of magnitude of the quartet Josephson energy E_q and quartet critical current I_{qc}. Figure B.9 shows the quartet signal as a function of $V_{bias,1}$. According to

$$E_q \approx \frac{\hbar I_c}{2e} \approx 28\ \mu\text{eV}, \tag{B.15}$$

the quartet critical current I_{qc} in our experiment is estimated to be ~ 8.4 nA. Note that same as in the Josephson case we showed earlier, the height of the quartet conductance peak is proportional to $2I_{qc}$ and serves as an important observable in the quartet experiment.

C

Floquet Formalism

This appendix discusses the application of Floquet theory on how to deal with a time-periodic problem and a toy-model for the quartet system is given.

C.1 Floquet Theorem

Given a quantum system and a periodic Hamiltonian $\hat{H}(t+T=\hat{H}(t)$, the Schrödinger equation takes the form ($\hbar=1$):

$$i\dot{\Psi}(t)=\hat{H}(t)\Psi(t), \tag{C.1}$$

where $\dot{\Psi}(t) = \frac{\partial\Psi}{\partial t}$. The Floquet theorem states that there exists a set of pseudo-energies ε_α and periodic functions $\Phi_\alpha(t+T)=\Phi_\alpha(t)$ such that the solutions are:

$$\Psi_\alpha(t)=e^{-i\varepsilon_\alpha t}\Phi_\alpha(t). \tag{C.2}$$

The function $\Phi_\alpha(t)$ obeys the Schrödinger equation:

$$i\dot{\Phi}_\alpha(t)=(\hat{H}(t)-\varepsilon_\alpha I)\ \Phi_\alpha(t). \tag{C.3}$$

One can expand $\Phi_\alpha(t)$ and $\hat{H}$(t) in Fourier series:

$$\Phi_\alpha(t)=\sum_{n=-\infty}^{\infty}e^{in\omega_0 t}\Phi_{m\alpha},\quad \hat{H}_n(t)=\sum_{n=-\infty}^{\infty}e^{in\omega_0 t}\hat{H}_n(t) \tag{C.4}$$

with $\omega_0 = 2\pi/T$ and $\hat{H}(t)$ are operators in the physical Hilbert space. This yields the secular equation for the wavefunctions $\Phi_{n\alpha}$:

$$(n\omega_0 - \varepsilon_\alpha)\Phi_{n\alpha} + \sum_m \hat{H}_{n-m}\Phi_{m\alpha} = 0. \tag{C.5}$$

This shows that the solution of Eq.C.1 amounts to find the eigenvalues and eigenvectors for a static Hamiltonian in an extended space, product of the original Hilbert space for $\hat{H}(t)$ by an infinite dimension space spanned by the integers n. The effective Floquet Hamiltonian $\hat{H}_{Fl}$ is given by:

$$\hat{H}_{Fl,nm} = \hat{H}_{n-m} + n\omega_0\delta_{nm}I. \tag{C.6}$$

Notice that the Floquet energies ε_α are defined up to a translation by $p\omega_0$ with arbitrary p. Therefore, one will seek the solution in the reduced "Floquet-Brillouin zone", $0 < \varepsilon < \varepsilon_\alpha + \omega_0$.

C.2 Floquet Theory of the Dot Toy-Model

For a single level dot model, the physical Hilbert space is two-dimensional. Consider electron and hole states, the Hamiltonian takes the form

$$\hat{H}(t) = \varepsilon_0(d_e^\dagger d_e - d_h^\dagger d_h) + (\Gamma d_e^\dagger d_h + h.c.), \tag{C.7}$$

where $\Gamma = \gamma_c e^{i\varphi_c} + \gamma_a e^{i\varphi_a} e^{i\omega_0 t} + \gamma_b e^{i\varphi_b} e^{-i\omega_0 t}$ when the superconducting leads are biased at $(V, -V, 0)$ and $\omega_0 = 2eV$ is the Josephson frequency.

The original Hilbert space has two dimensions and the wavefunction $\Psi(t)$ is represented by a two-component spinor $(\Psi_e(t), \Psi_h(t))$. For $V = 0$, the diagonalization of the static Hamiltonian is trivial and gives the two symmetric Andreev bound states with wave function $\Psi_\pm(\varphi)$ as we showed in Chapter 2:

$$E_{ABS,\pm}(\varphi_{a,b,c}) = \pm|\Gamma|. \tag{C.8}$$

Applying the Floquet approach in the electron-hole basis yields the solution with $\Psi_{n\alpha}(t) = (\Psi_{n,e\alpha}(t), \Psi_{n,h\alpha}(t))$:

$$(n\omega_0 - \varepsilon_\alpha)\Phi_{n,e\alpha} + \gamma_c e^{i\varphi_c}\Phi_{n,h\alpha} + \gamma_a e^{i\varphi_a}\Phi_{n+1,h\alpha} + \gamma_b e^{i\varphi_b}\Phi_{n-1,h\alpha} = 0 \tag{C.9}$$

$$(n\omega_0 - \varepsilon_\alpha)\Phi_{n,h\alpha} + \gamma_c e^{-i\varphi_c}\Phi_{n,e\alpha} + \gamma_a e^{-i\varphi_a}\Phi_{n-1,e\alpha} + \gamma_b e^{-i\varphi_b}\Phi_{n+1,e\alpha} = 0. \tag{C.10}$$

and only two values of the quasi-energies ε_α are retained.

The Flouqet Hamiltonian corresponds to a matrix in the enlarged Hilbert space but can be truncated. For example, if the order of the truncation is 2 we have (for a resonant dot $\varepsilon_0 = 0$):

$$\hat{H}_{Fl} = \begin{pmatrix}
-2\omega_0 & \gamma_c e^{i\varphi_c} & 0 & \gamma_a e^{i\varphi_a} & 0 & 0 & 0 & 0 & 0 & 0 \\
\gamma_c e^{-i\varphi_c} & -2\omega_0 & \gamma_b e^{-i\varphi_b} & 0 & 0 & 0 & 0 & 0 & 0 & 0 \\
0 & \gamma_b e^{i\varphi_b} & -\omega_0 & \gamma_c e^{i\varphi_c} & 0 & \gamma_a e^{i\varphi_a} & 0 & 0 & 0 & 0 \\
\gamma_a e^{-i\varphi_a} & 0 & \gamma_c e^{-i\varphi_c} & -\omega_0 & \gamma_b e^{-i\varphi_b} & 0 & 0 & 0 & 0 & 0 \\
0 & 0 & 0 & \gamma_b e^{i\varphi_b} & 0 & \gamma_c e^{i\varphi_c} & 0 & \gamma_a e^{i\varphi_a} & 0 & 0 \\
0 & 0 & \gamma_a e^{-i\varphi_a} & 0 & \gamma_c e^{-i\varphi_c} & 0 & \gamma_b e^{-i\varphi_b} & 0 & 0 & 0 \\
0 & 0 & 0 & 0 & 0 & \gamma_b e^{i\varphi_b} & \omega_0 & \gamma_c e^{i\varphi_c} & 0 & \gamma_a e^{i\varphi_a} \\
0 & 0 & 0 & 0 & \gamma_a e^{-i\varphi_a} & 0 & \gamma_c e^{-i\varphi_c} & \omega_0 & \gamma_b e^{-i\varphi_b} & 0 \\
0 & 0 & 0 & 0 & 0 & 0 & 0 & \gamma_b e^{i\varphi_b} & 2\omega_0 & \gamma_c e^{i\varphi_c} \\
0 & 0 & 0 & 0 & 0 & 0 & \gamma_a e^{-i\varphi_a} & 0 & \gamma_c e^{-i\varphi_c} & 2\omega_0
\end{pmatrix} \tag{C.11}$$

Using this dot model, figure C.1 shows the Floquet energies plotted as a function of the quartet phase for different values of V.

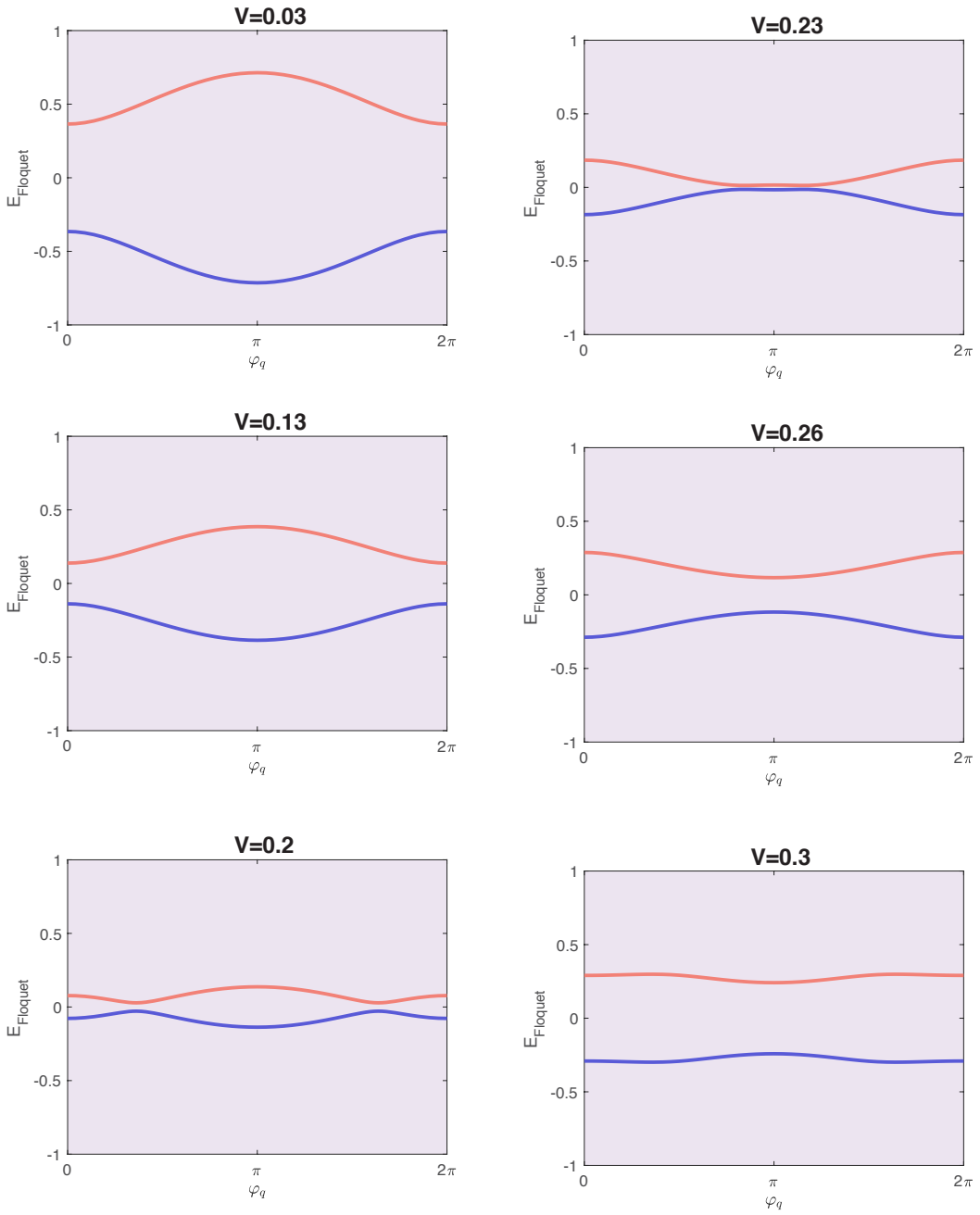

Figure C.1: Calculated Floquet levels using the dot toy-model. The energies are plotted as a function of the quartet phase for different values of V.

D

Quartet in Loop-biased Measurement

This appendix contains the data acquired from the quartet measurement with loop-biased configuration. The circuit is shown in figure D.1. It is basically the same as the loop-grounded measurement in Chapter 4, except that now the loop is biased with a DC voltage with S_1 grounded. While we do not have the complete explanation for this set of the data, it may be a useful reference for future experiments investigating on the nature of quartet.

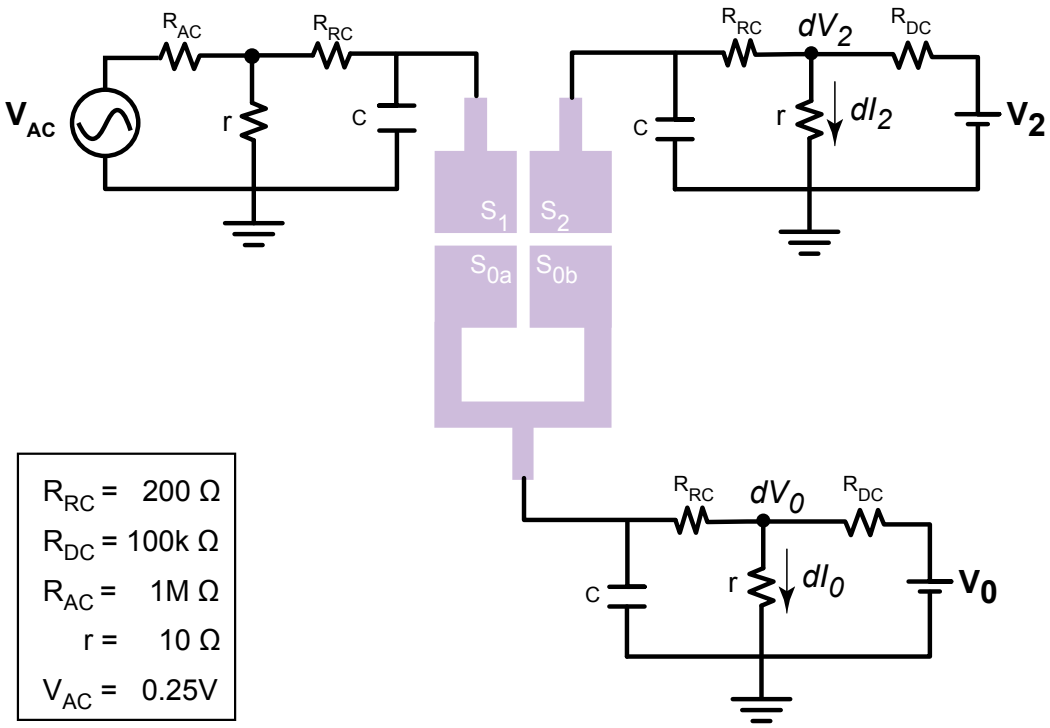

Figure D.1: Circuit of quartet measurement when the loop is biased.

Figure D.2 shows the differential conductance as the DC voltage biases V_2 and V_0. The quartet critical current is rather large compared to that in the loop-grounded measurement. Also, the conductance between the two biased leads are more asymmetric, while the loop-grounded data shows decent symmetry. The loop in general has a higher conductance. It is understandable since the loop terminal has a contact area on graphene more than twice of the other two terminals.

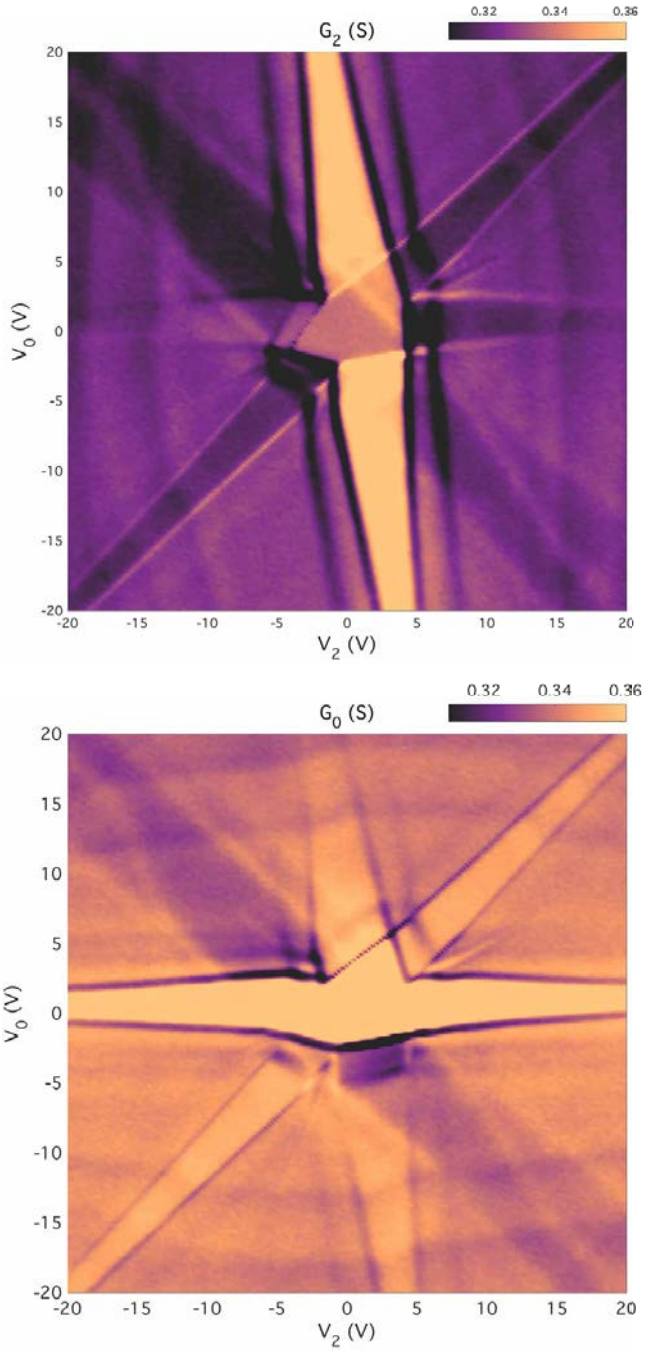

Figure D.2: V_2-V_0 scan with the loop-biased configuration

In the magnetic field dependence data we notice two features. Figure D.3 shows the large range of magnetic field scan and figure D.4 top panel is the zoom-in scan with $-0.9 < B < 0.4$ mT. All the data are taken by sweeping V_0 when V_2 is fixed at -10 V. First of all, as shown in the bottom panel of figure D.4, we compare the behavior of the conductance at the two terminals G_0 and G_0 as a function of B. On the left, we fix $V_0 = V_2$= -10 V, which is the Josephson current along the $+45^\circ$ line. We find that the conductance at the two biased terminals are anti-parallel: when G_0 is large, G_2 is small, and vice versa. This makes sense since G_0 and G_2 are the supercurrents flowing in the opposite directions between S_0 and S_2. On the other hand, the quartet signal has parallel behavior between G_0 and G_2; they increase or decrease synchronously as a function of magnetic field. It manifests the essence of the quartet: it is a supercurrent that flow from the grounded terminal simultaneously to the other two terminals that are biased at $(+V, -V)$.

The second feature is period doubling of the quartet current compared to the usual Josephson current. This can be seen in the color plots. Figure D.5 further shows the linecuts taken at three different value of V_0, corresponding to the quartet current ($V_0 = -V_2$), and two Josephson currents at $V_0 = 0$, $V_0 = V_2$. The curves are shifted in y-direction for clarity. While the oscillations of Josephson current has a period of δB =158 μT, which is comparable to what we see in the loop-grounded case (145 μ T), the oscillations of quartet has a period of δB =315 μT. Considering the area enclosed by the device loop should be the same for both quartet and Josephson currents, it implies that the flux quantum in the quartet case is h/e instead of $h/2e$. This is quite counterintuitive and remains a mystery to be solved in the future.

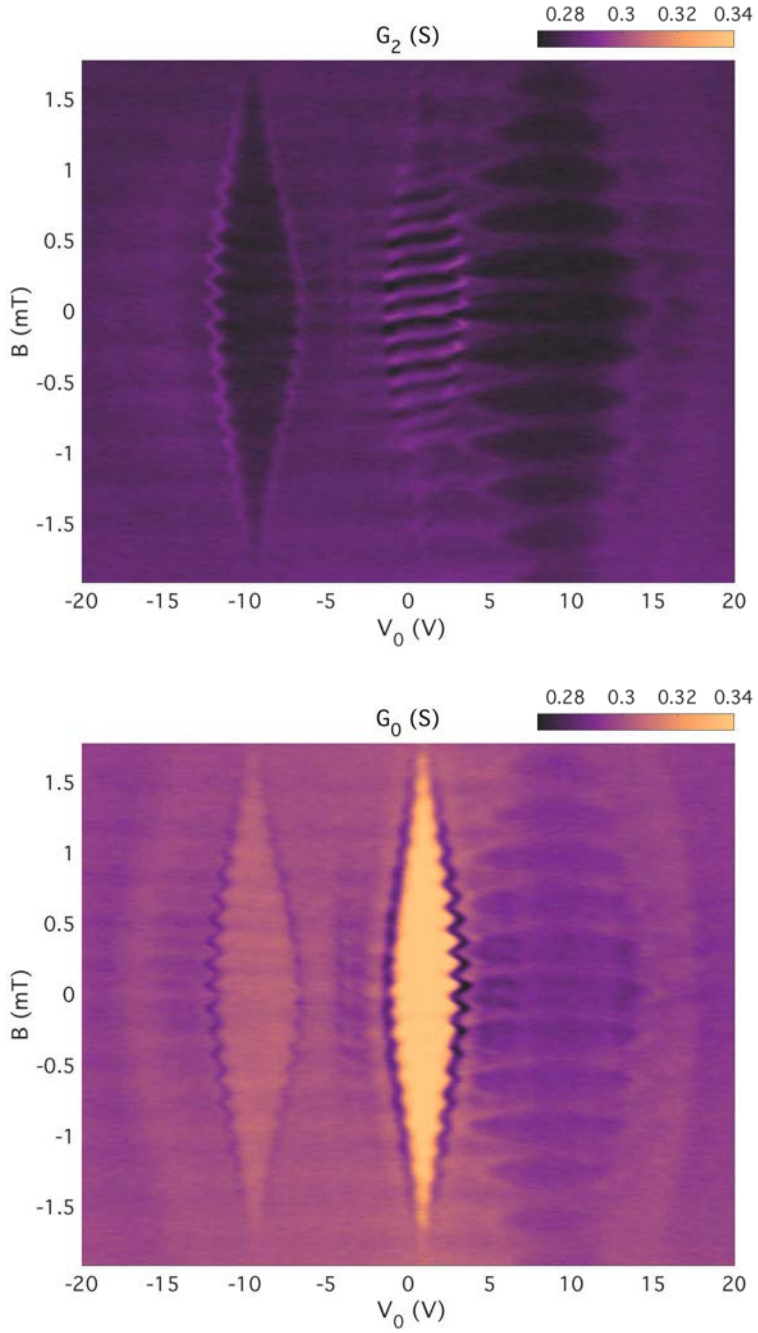

Figure D.3: Conductance as a function of V_0 and magnetic field with the loop-biased configuration. Top panel: G_2 measured at S_2. Bottom panel: G_0 measured at the loop S_0.

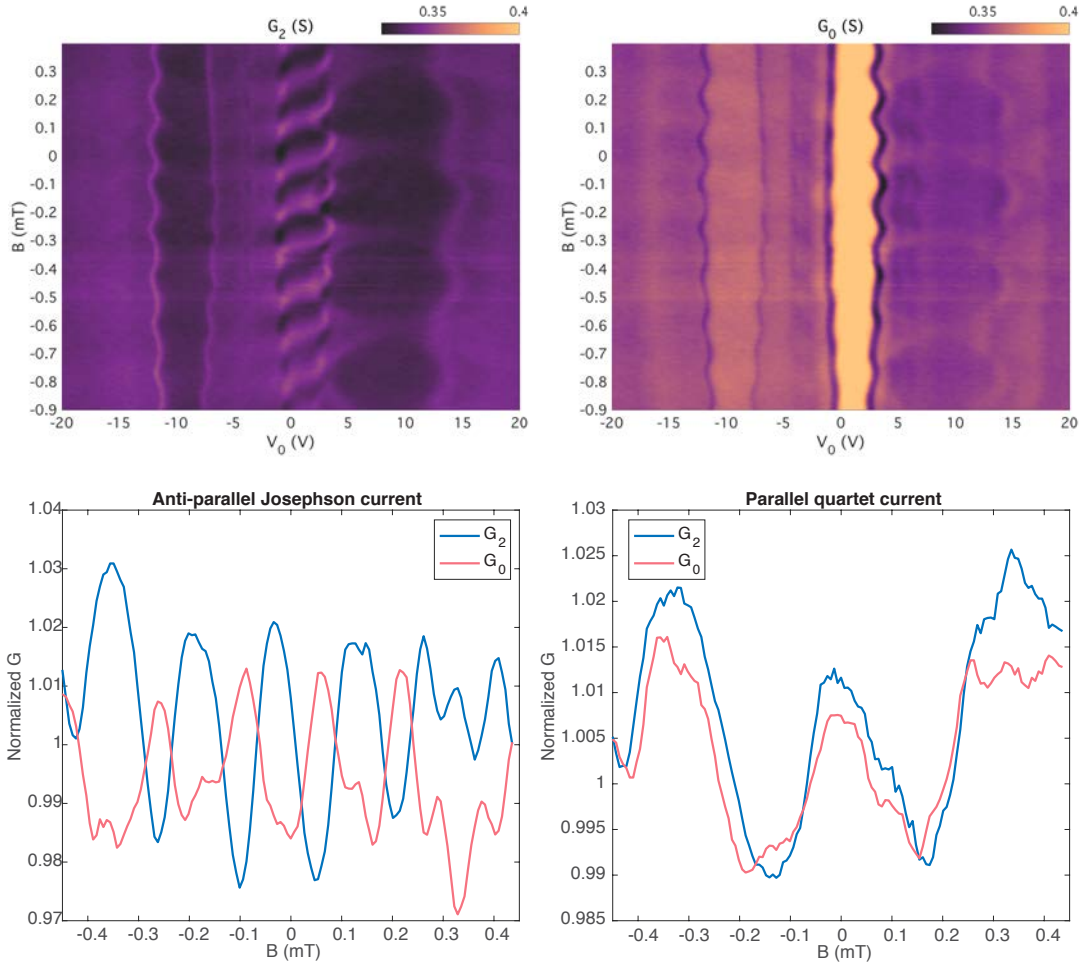

Figure D.4: Anti-parallel Josephson currents compared to parallel quartet currents at the two biased terminals.

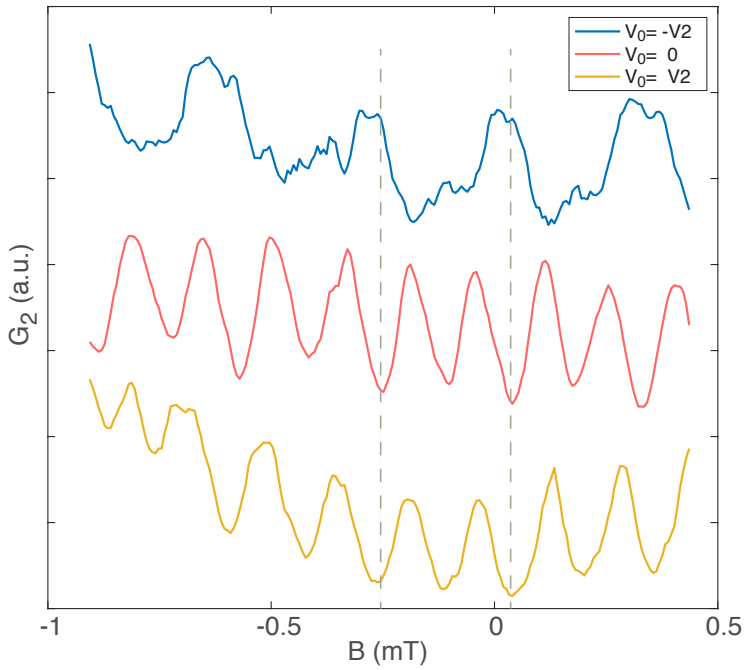

Figure D.5: Conductance as a function of magnetic field for comparison between quartet current ($V_0 = -V_2$) and Josephson currents ($V_0 = 0, V_0 = V_2$). The quartet current has a period of 315 μT, which is twice of the period of the Josephson currents.

References

[1] R. Holm and W. Meissner. Messungen mit hilfe von flüssigem helium. xiii. *Zeitschrift für Physik*, 74(11):715–735, 1932. doi: 10.1007/BF01340420. URL https://doi.org/10.1007/BF01340420. 2

[2] J. Bardeen, L. N. Cooper, and J. R. Schrieffer. Microscopic theory of superconductivity. *Physical Review*, 106(1):162–164, Apr 1957. doi: 10.1103/PhysRev.106.162. URL https://link.aps.org/doi/10.1103/PhysRev.106.162. 7

[3] N. N. Bogoljubov. On a new method in the theory of superconductivity. *Il Nuovo Cimento*, 7(6):794–805, Mar 1958. ISSN 1827-6121. doi: 10.1007/bf02745585. URL http://dx.doi.org/10.1007/BF02745585. 10

[4] P. G. de Gennes. Boundary effects in superconductors. *Reviews of Modern Physics*, 36(1):225–237, 1964. doi: 10.1103/RevModPhys.36.225. URL https://journals.aps.org/rmp/pdf/10.1103/RevModPhys.36.225. 10

[5] P. G. de Gennes. *Superconductivity of Metals and Alloys*. W. A. Benjaminm, New York, 1966. 10

[6] J. K. Hulm. Thermal resistivity of mercury in the intermediate state. *Physical Review*, 90(6):1116–1116, 1953. doi: 10.1103/PhysRev.90.1116. URL https://journals.aps.org/pr/pdf/10.1103/PhysRev.90.1116. 15

[7] S. Strässler and P. Wyder. Thermal conductivity and electron scattering at interphase boundaries in a superconductor. *Physical Review Letters*, 10(6):225–227, 1963. doi: 10.1103/PhysRevLett.10.225. URL https://journals.aps.org/prl/pdf/10.1103/PhysRevLett.10.225. 15

[8] A.F. Andreev. The thermal conductivity of the intermediate state in superconductors. *Journal of Experimental and Theoretical Physics*, 19(5):1228, Nov 1964. URL http://www.jetp.ac.ru/cgi-bin/dn/e_019_05_1228.pdf. 15

[9] G. E. Blonder, M. Tinkham, and T. M. Klapwijk. Transition from metallic to tunneling regimes in superconducting microconstrictions: Excess current, charge imbalance, and supercurrent conversion. *Physical Review B*, 25(7):4515–4532, 1982. doi: 10.1103/PhysRevB.25.4515. URL https://journals.aps.org/prb/abstract/10.1103/PhysRevB.25.4515. 15

[10] A.F. Andreev. Electron spectrum of the intermediate state of superconductors. *Journal of Experimental and Theoretical Physics*, 22(2):655, Feb 1966. URL http://jetp.ac.ru/cgi-bin/dn/e_022_02_0455.pdf. 27

[11] I.O. Kulik. Macroscopic quantization and the proximity effect in s-n-s junctions. *Journal of Experimental and Theoretical Physics*, 30(5):944, May 1970. URL http://www.jetp.ac.ru/cgi-bin/dn/e_030_05_0944.pdf. 28

[12] C. W. J. Beenakker and H. van Houten. Josephson current through a superconducting quantum point contact shorter than the coherence length. *Physical Review Letters*, 66(23):3056–3059, 1991. doi: 10.1103/PhysRevLett.66.3056. URL https://journals.aps.org/prl/abstract/10.1103/PhysRevLett.66.3056. 28

[13] Akira Furusaki and Masaru Tsukada. Current-carrying states in josephson junctions. *Physical Review B*, 43(13):10164–10169, 1991. doi: 10.1103/PhysRevB.43.10164. URL https://journals.aps.org/prb/abstract/10.1103/PhysRevB.43.10164. 28, 29

[14] C. W. J. Beenakker. Universal limit of critical-current fluctuations in mesoscopic josephson junctions. *Physical Review Letters*, 67(27):3836–3839, 1991. doi: 10.1103/PhysRevLett.67.3836. URL https://journals.aps.org/prl/abstract/10.1103/PhysRevLett.67.3836. 28

[15] Leon N. Cooper. Bound electron pairs in a degenerate fermi gas. *Physical Review*, 104(4):1189–1190, Nov 1956. doi: 10.1103/PhysRev.104.1189. URL https://journals.aps.org/pr/pdf/10.1103/PhysRev.104.1189. 31

[16] W. J. Tomasch. Geometrical resonance and boundary effects in tunneling from superconducting in. *Physical Review Letters*, 16(1):16–19, Jan 1966. doi: 10.1103/PhysRevLett.16.16. URL https://journals.aps.org/prl/abstract/10.1103/PhysRevLett.16.16. 44

[17] W. L. McMillan and P. W. Anderson. Theory of geometrical resonances in the tunneling characteristics of thick films of superconductors. *Physical Review Letters*, 16(3):85–87, Jan 1966. doi:

10.1103/PhysRevLett.16.85. URL https://link.aps.org/doi/10.1103/PhysRevLett.16.85. 44

[18] C. Visani, Z. Sefrioui, J. Tornos, C. Leon, J. Briatico, M. Bibes, A. Barthélémy, J. Santamaría, and Javier E. Villegas. Equal-spin andreev reflection and long-range coherent transport in high-temperature superconductor/half-metallic ferromagnet junctions. *Nature Physics*, 8(7):539–543, May 2012. ISSN 1745-2481. doi: 10.1038/nphys2318. URL http://dx.doi.org/10.1038/nphys2318. 44, 45, 46

[19] J. M. Rowell and W. L. McMillan. Electron interference in a normal metal induced by superconducting contracts. *Physical Review Letters*, 16(11):453–456, Mar 1966. doi: 10.1103/PhysRevLett.16.453. URL https://journals.aps.org/prl/abstract/10.1103/PhysRevLett.16.453. 45, 46

[20] J. M. Rowell. Tunneling observation of bound states in a normal metal—superconductor sandwich. *Physical Review Letters*, 30(5):167–170, Jan 1973. doi: 10.1103/PhysRevLett.30.167. URL https://journals.aps.org/prl/abstract/10.1103/PhysRevLett.30.167. 45

[21] Kenji Watanabe, Takashi Taniguchi, and Hisao Kanda. Direct-bandgap properties and evidence for ultraviolet lasing of hexagonal boron nitride single crystal. *Nature Materials*, 3(6):404–409, May 2004. ISSN 1476-4660. doi: 10.1038/nmat1134. URL http://dx.doi.org/10.1038/nmat1134. 46

[22] Y. Kubota, K. Watanabe, O. Tsuda, and T. Taniguchi. Deep ultraviolet light-emitting hexagonal boron nitride synthesized at atmospheric pressure. *Science*, 317(5840):932–934, Aug 2007. ISSN 1095-9203. doi: 10.1126/science.1144216. URL http://dx.doi.org/10.1126/science.1144216. 46

[23] F. Amet, J. R. Williams, A. G. F. Garcia, M. Yankowitz, K. Watanabe, T. Taniguchi, and D. Goldhaber-Gordon. Tunneling spectroscopy of graphene-boron-nitride heterostructures. *Physical Review B*, 85(7), 2012. doi: 10.1103/PhysRevB.85.073405. URL https://journals.aps.org/prb/pdf/10.1103/PhysRevB.85.073405. 47

[24] Liam Britnell, Roman V. Gorbachev, Rashid Jalil, Branson D. Belle, Fred Schedin, Mikhail I. Katsnelson, Laurence Eaves, Sergey V. Morozov, Alexander S. Mayorov, Nuno M. R. Peres, and et al. Electron tunneling through ultrathin boron nitride crystalline barriers. *Nano Letters*, 12(3):1707–1710, Mar 2012. ISSN 1530-6992. doi: 10.1021/nl3002205. URL http://dx.doi.org/10.1021/nl3002205. 47

[25] Chendong Zhang, Amber Johnson, Chang-Lung Hsu, Lain-Jong Li, and Chih-Kang Shih. Direct imaging of band profile in single layer mos2 on graphite: Quasiparticle energy gap, metallic edge states, and edge band bending. *Nano Letters*, 14(5):2443–2447, May 2014. ISSN 1530-6992. doi: 10.1021/nl501133c. URL http://dx.doi.org/10.1021/nl501133c. 49

[26] A. R. Klots, A. K. M. Newaz, Bin Wang, D. Prasai, H. Krzyzanowska, Junhao Lin, D. Caudel, N. J. Ghimire, J. Yan, B. L. Ivanov, and et al. Probing excitonic states in suspended two-dimensional semiconductors by photocurrent spectroscopy. *Scientific Reports*, 4(1), Oct 2014. ISSN 2045-2322. doi: 10.1038/srep06608. URL http://dx.doi.org/10.1038/srep06608. 49

[27] Dimitri Roditchev, Christophe Brun, Lise Serrier-Garcia, Juan Carlos Cuevas, Vagner Henrique Loiola Bessa, Milorad Vlado Milošević, François Debontridder, Vasily Stolyarov, and Tristan Cren. Direct observation of josephson vortex cores. *Nature Physics*, 11(4):332–337, Feb 2015. ISSN 1745-2481. doi: 10.1038/nphys3240. URL http://dx.doi.org/10.1038/nphys3240. 66

[28] A. K. Geim, S. V. Dubonos, J. J. Palacios, I. V. Grigorieva, M. Henini, and J. J. Schermer. Fine structure in magnetization of individual fluxoid states. *Physical Review Letters*, 85(7):1528–1531, Aug 2000. doi: 10.1103/PhysRevLett.85.1528. URL https://link.aps.org/doi/10.1103/PhysRevLett.85.1528. 66

[29] A. Kanda, B. J. Baelus, F. M. Peeters, K. Kadowaki, and Y. Ootuka. Experimental evidence for giant vortex states in a mesoscopic superconducting disk. *Physical Review Letters*, 93 (25), 2004. doi: 10.1103/PhysRevLett.93.257002. URL https://link.aps.org/doi/10.1103/PhysRevLett.93.257002. 66

[30] B. van Heck, S. Mi, and A. R. Akhmerov. Single fermion manipulation via superconducting phase differences in multiterminal josephson junctions. *Physical Review B*, 90(15), 2014. doi: 10.1103/PhysRevB.90.155450. URL https://journals.aps.org/prb/abstract/10.1103/PhysRevB.90.155450. 69

[31] Tomohiro Yokoyama and Yu. V. Nazarov. Singularities in the andreev spectrum of a multiterminal josephson junction. *Physical Review B*, 92(15), 2015. doi: 10.1103/PhysRevB.92.155437. URL https://journals.aps.org/prb/abstract/10.1103/PhysRevB.92.155437. 69, 128

[32] Roman-Pascal Riwar, Manuel Houzet, Julia S. Meyer, and Yuli V. Nazarov. Multi-terminal josephson junctions as topological matter. *Nature Communications*, 7(1), Apr 2016. ISSN 2041-1723. doi: 10.1038/ncomms11167. URL http://dx.doi.org/10.1038/ncomms11167. 69, 128, 130, 132

[33] Hong-Yi Xie and Alex Levchenko. Topological andreev bands in three-terminal josephson junctions. *Physical Review B*, 96(16), 2017. doi: 10.1103/PhysRevB.96.161406. URL https://journals.aps.org/prb/abstract/10.1103/PhysRevB.96.161406. 69, 128

[34] Julia S. Meyer and Manuel Houzet. Nontrivial chern numbers in three-terminal josephson junctions. *Physical Review Letters*, 119(13), 2017. doi: 10.1103/PhysRevLett.119.136807. URL https://journals.aps.org/prl/abstract/10.1103/PhysRevLett.119.136807. 69, 128

[35] Erik Eriksson, Roman-Pascal Riwar, Manuel Houzet, Julia S. Meyer, and Yu. V. Nazarov. Topological transconductance quantization in a four-terminal josephson junction. *Physical Review B*, 95(7), 2017. doi: 10.1103/PhysRevB.95.075417. URL https://journals.aps.org/prb/abstract/10.1103/PhysRevB.95.075417. 69, 128

[36] Hong-Yi Xie, Maxim G. Vavilov, and Alex Levchenko. Weyl nodes in andreev spectra of multiterminal josephson junctions: Chern numbers, conductances, and supercurrents. *Physical Review B*, 97(3), 2018. doi: 10.1103/PhysRevB.97.035443. URL https://journals.aps.org/prb/abstract/10.1103/PhysRevB.97.035443. 69, 128

[37] M. A. H. Nerenberg, James A. Blackburn, and D. W. Jillie. Voltage locking and other interactions in coupled superconducting weak links. i. theory. *Physical Review B*, 21(1):118–124, 1980. doi: 10.1103/PhysRevB.21.118. URL https://journals.aps.org/prb/abstract/10.1103/PhysRevB.21.118. 72

[38] J. C. Cuevas and H. Pothier. Voltage-induced shapiro steps in a superconducting multiterminal structure. *Physical Review B*, 75(17), 2007. doi: 10.1103/PhysRevB.75.174513. URL https://journals.aps.org/prb/abstract/10.1103/PhysRevB.75.174513. 72

[39] A. H. Pfeffer, J. E. Duvauchelle, H. Courtois, R. Melin, D. Feinberg, and F. Lefloch. Subgap structure in the conductance of a three-terminal josephson junction. *Physical Review B*, 90(7), 2014. doi: 10.1103/PhysRevB.90.075401. URL https://doi.org/10.1103/PhysRevB.90.075401. 73, 101

[40] Yonatan Cohen, Yuval Ronen, Jung-Hyun Kang, Moty Heiblum, Denis Feinberg, Régis Mélin, and Hadas Shtrikman. Nonlocal supercurrent of quartets in a three-terminal josephson junction. *Proceedings of the National Academy of Sciences*, 115(27):6991–6994, Jun 2018. ISSN 1091-6490. doi: 10.1073/pnas.1800044115. URL http://dx.doi.org/10.1073/pnas.1800044115. 73, 101, 153

[41] Anne W. Draelos, Ming-Tso Wei, Andrew Seredinski, Hengming Li, Yash Mehta, Kenji Watanabe, Takashi Taniguchi, Ivan V. Borzenets, François Amet, and Gleb Finkelstein. Supercurrent flow in multiterminal graphene josephson junctions. *Nano Letters*, 19(2):1039–1043, Jan 2019. ISSN 1530-6992. doi: 10.1021/acs.nanolett.8b04330. URL http://dx.doi.org/10.1021/acs.nanolett.8b04330. 75

[42] Natalia Pankratova, Hanho Lee, Roman Kuzmin, Maxim Vavilov, Kaushini Wickramasinghe, William Mayer, Joseph Yuan, Javad Shabani, and Vladimir E. Manucharyan. The multiterminal josephson effect. *arXiv:1812.06017*, 2018. URL https://arxiv.org/abs/1812.06017. 75

[43] Gino V. Graziano, Joon Sue Lee, Mihir Pendharkar, Chris J. Palmstrøm, and Vlad S. Pribiag. Transport studies in a gate-tunable three-terminal josephson junction. *Physical Review B*, 101(5), 2020. doi: 10.1103/PhysRevB.101.054510. URL https://journals.aps.org/prb/abstract/10.1103/PhysRevB.101.054510. 75

[44] M. T. Allen, O. Shtanko, I. C. Fulga, A. R. Akhmerov, K. Watanabe, T. Taniguchi, P. Jarillo-Herrero, L. S. Levitov, and A. Yacoby. Spatially resolved edge currents and guided-wave electronic states in graphene. *Nature Physics*, 12(2):128–133, Nov 2015. ISSN 1745-2481. doi: 10.1038/nphys3534. URL http://dx.doi.org/10.1038/nphys3534. 76

[45] M. Ben Shalom, M. J. Zhu, V. I. Fal'ko, A. Mishchenko, A. V. Kretinin, K. S. Novoselov, C. R. Woods, K. Watanabe, T. Taniguchi, A. K. Geim, and et al. Quantum oscillations of the critical current and high-field superconducting proximity in ballistic graphene. *Nature Physics*, 12(4):318–322, Dec 2015. ISSN 1745-2481. doi: 10.1038/nphys3592. URL http://dx.doi.org/10.1038/nphys3592. 76

[46] I. V. Borzenets, F. Amet, C. T. Ke, A. W. Draelos, M. T. Wei, A. Seredinski, K. Watanabe, T. Taniguchi, Y. Bomze, M. Yamamoto, S. Tarucha, and G. Finkelstein. Ballistic graphene josephson junctions from the short to the long junction regimes. *Physical Review Letters*, 117

(23), 2016. doi: 10.1103/PhysRevLett.117.237002. URL https://journals.aps.org/prl/abstract/10.1103/PhysRevLett.117.237002. 76

[47] Clarence Zener. Non-adiabatic crossing of energy levels. *Proceedings of the Royal Society of London. Series A, Containing Papers of a Mathematical and Physical Character*, 137(833):696–702, Sep 1932. ISSN 2053-9150. doi: 10.1098/rspa.1932.0165. URL http://dx.doi.org/10.1098/rspa.1932.0165. 108

[48] I. I. Rabi. On the process of space quantization. *Physical Review*, 49(4):324–328, 1936. doi: 10.1103/PhysRev.49.324. URL https://journals.aps.org/pr/abstract/10.1103/PhysRev.49.324. 110, 111

[49] M. L. Della Rocca, M. Chauvin, B. Huard, H. Pothier, D. Esteve, and C. Urbina. Measurement of the current-phase relation of superconducting atomic contacts. *Physical Review Letters*, 99 (12), 2007. doi: 10.1103/PhysRevLett.99.127005. URL https://journals.aps.org/prl/abstract/10.1103/PhysRevLett.99.127005. 111

[50] J-D. Pillet, C. H. L. Quay, P. Morfin, C. Bena, A. Levy Yeyati, and P. Joyez. Andreev bound states in supercurrent-carrying carbon nanotubes revealed. *Nature Physics*, 6(12):965–969, Nov 2010. ISSN 1745-2481. doi: 10.1038/nphys1811. URL http://dx.doi.org/10.1038/nphys1811. 111

[51] W. Chang, V. E. Manucharyan, T. S. Jespersen, J. Nygård, and C. M. Marcus. Tunneling spectroscopy of quasiparticle bound states in a spinful josephson junction. *Physical Review Letters*, 110(21), 2013. doi: 10.1103/PhysRevLett.110.217005. URL https://journals.aps.org/prl/abstract/10.1103/PhysRevLett.110.217005. 111

[52] L. Bretheau, Ç. Ö. Girit, H. Pothier, D. Esteve, and C. Urbina. Exciting andreev pairs in a superconducting atomic contact. *Nature*, 499(7458):312–315, Jul 2013. ISSN 1476-4687. doi: 10.1038/nature12315. URL http://dx.doi.org/10.1038/nature12315. 111

[53] L. Bretheau, Ç. Ö. Girit, C. Urbina, D. Esteve, and H. Pothier. Supercurrent spectroscopy of andreev states. *Physical Review X*, 3(4), 2013. doi: 10.1103/PhysRevX.3.041034. URL https://journals.aps.org/prx/abstract/10.1103/PhysRevX.3.041034. 111

[54] C. Janvier, L. Tosi, L. Bretheau, Ç. Ö. Girit, M. Stern, P. Bertet, P. Joyez, D. Vion, D. Esteve, M. F. Goffman, and et al. Coherent manipulation of andreev states in superconducting atomic

contacts. *Science*, 349(6253):1199–1202, Sep 2015. ISSN 1095-9203. doi: 10.1126/science.aab2179. URL http://dx.doi.org/10.1126/science.aab2179. 111

[55] J. J. A. Baselmans, A. F. Morpurgo, B. J. van Wees, and T. M. Klapwijk. Reversing the direction of the supercurrent in a controllable josephson junction. *Nature*, 397(6714):43–45, Jan 1999. ISSN 1476-4687. doi: 10.1038/16204. URL http://dx.doi.org/10.1038/16204. 111

[56] T. T. Heikkilä F. S. Bergeret, P. Virtanen and J. C. Cuevas. Theory of microwave-assisted supercurrent in quantum point contacts. *Physical Review Letters*, 105(11):4, Sep 2010. doi: 10.1103/PhysRevLett.105.117001. URL https://link.aps.org/doi/10.1103/PhysRevLett.105.117001. 111

[57] F. S. Bergeret, P. Virtanen, A. Ozaeta, T. T. Heikkilä, and J. C. Cuevas. Supercurrent and andreev bound state dynamics in superconducting quantum point contacts under microwave irradiation. *Physical Review B*, 84(5):14, Aug 2011. doi: 10.1103/PhysRevB.84.054504. URL https://link.aps.org/doi/10.1103/PhysRevB.84.054504. 111

[58] B. Venitucci, D. Feinberg, R. Mélin, and B. Douçot. Nonadiabatic josephson current pumping by chiral microwave irradiation. *Physical Review B*, 97(19):195423, May 2018. doi: 10.1103/PhysRevB.97.195423. URL https://link.aps.org/doi/10.1103/PhysRevB.97.195423. 111

[59] I. Chiorescu, P. Bertet, K. Semba, Y. Nakamura, C. J. P. M. Harmans, and J. E. Mooij. Coherent dynamics of a flux qubit coupled to a harmonic oscillator. *Nature*, 431(7005):159–162, Sep 2004. ISSN 1476-4687. doi: 10.1038/nature02831. URL http://dx.doi.org/10.1038/nature02831. 111

[60] G. D. Fuchs, V. V. Dobrovitski, D. M. Toyli, F. J. Heremans, and D. D. Awschalom. Gigahertz dynamics of a strongly driven single quantum spin. *Science*, 326(5959):1520–1522, Nov 2009. ISSN 1095-9203. doi: 10.1126/science.1181193. URL http://dx.doi.org/10.1126/science.1181193. 111

[61] Chunqing Deng, Jean-Luc Orgiazzi, Feiruo Shen, Sahel Ashhab, and Adrian Lupascu. Observation of floquet states in a strongly driven artificial atom. *Physical Review Letters*, 115(13), 2015. doi: 10.1103/PhysRevLett.115.133601. URL https://journals.aps.org/prl/abstract/10.1103/PhysRevLett.115.133601. 111

[62] *Biographical Memoirs V.64 (1994)*. National Academy of Sciences. doi: https://doi.org/10.17226/4547. 112

[63] Gaston Floquet. Sur les equations di erentielles lin- eaires a coe cients periodiques. *Annales de l'Ecole Normale Superieure*, 12(47):47–88, 1883. doi: 10.24033/asens.220. URL http://www.numdam.org/item/ASENS_1883_2_12__47_0. 113

[64] S.-Y. Xu, I. Belopolski, N. Alidoust, M. Neupane, G. Bian, C. Zhang, R. Sankar, G. Chang, Z. Yuan, C.-C. Lee, and et al. Discovery of a weyl fermion semimetal and topological fermi arcs. *Science*, 349(6248):613–617, Jul 2015. ISSN 1095-9203. doi: 10.1126/science.aaa9297. URL http://dx.doi.org/10.1126/science.aaa9297. 128

[65] Régis Mélin, Romain Danneau, Kang Yang, Jean-Guy Caputo, and Benoît Douçot. Engineering the floquet spectrum of superconducting multiterminal quantum dots. *Physical Review B*, 100(3), 2019. doi: 10.1103/PhysRevB.100.035450. URL https://journals.aps.org/prb/abstract/10.1103/PhysRevB.100.035450. 129, 130

[66] Wang Yao, A. H. MacDonald, and Qian Niu. Optical control of topological quantum transport in semiconductors. *Physical Review Letters*, 99(4), 2007. doi: 10.1103/PhysRevLett.99.047401. URL https://journals.aps.org/prl/abstract/10.1103/PhysRevLett.99.047401. 132

[67] Takashi Oka and Hideo Aoki. Photovoltaic hall effect in graphene. *Physical Review B*, 79 (8), 2009. doi: 10.1103/PhysRevB.79.081406. URL https://journals.aps.org/prb/abstract/10.1103/PhysRevB.79.081406. 132

[68] Takuya Kitagawa, Erez Berg, Mark Rudner, and Eugene Demler. Topological characterization of periodically driven quantum systems. *Physical Review B*, 82(23), 2010. doi: 10.1103/PhysRevB.82.235114. URL https://journals.aps.org/prb/abstract/10.1103/PhysRevB.82.235114. 132

[69] Netanel H. Lindner, Gil Refael, and Victor Galitski. Floquet topological insulator in semiconductor quantum wells. *Nature Physics*, 7(6):490–495, Mar 2011. ISSN 1745-2481. doi: 10.1038/nphys1926. URL http://dx.doi.org/10.1038/nphys1926. 132

[70] Karthik I. Seetharam, Charles-Edouard Bardyn, Netanel H. Lindner, Mark S. Rudner, and Gil Refael. Controlled population of floquet-bloch states via coupling to bose and fermi baths.

Physical Review X, 5(4), 2015. doi: 10.1103/PhysRevX.5.041050. URL https://journals.aps.org/prx/abstract/10.1103/PhysRevX.5.041050. 133

[71] Xiaomeng Liu. *Correlated Electron States in Coupled Graphene Double-layer Heterostructures*. PhD thesis, Harvard University, 2018. URL http://kim.physics.harvard.edu/wp-uploads/2014/05/Liu_Dissertation_2018.pdf. 134

[72] Austin Kcon Cheng. *Electric Transport in Hybrid Carbon Nanotube-Graphene Devices*. PhD thesis, Harvard University, 2019. URL http://kim.physics.harvard.edu/wp-uploads/2014/05/dissertation_AustinCheng.pdf. 134